UNIVERSITÉ DE NEUCHÂTEL

THÈSE PRÉSENTÉE À LA FACULTÉ DES SCIENCES, UNIVERSITÉ DE NEUCHÂTEL POUR L'OBTENTION DU GRADE DE DOCTEUR ÈS SCIENCES.

UNIVERSITÉ DE NEUCHÂTEL

LABORATOIRE TEMPS-FRÉQUENCE (LTF)

Ramsey Spectroscopy in a Rubidium Vapor Cell and Realization of an Ultra-Stable Atomic Clock

Thèse présentée par:

Mohammadreza GHARAVIPOUR

M.Sc. University of Ulm, Germany

Acceptée le 31 Mai 2018 sur proposition du jury:

Prof. Dr. Gaetano MILETI,Université de Neuchâtel, Directeur de thèse

Prof. Dr. James CAMPARO,Whittier College Aerospace Corporation, Los Angeles, USA, Rapporteur

Prof. Dr. Brana JELENKOVIĆ,University of Belgrade, Institute of Physics, Serbia, Rapporteur

Dr. Salvatore MICALIZO,Istituto Nazionale di Ricerca Metrologica (INRIM), Turin, Italy, Rapporteur

Dr. Christoph AFFOLDERBACH,Université de Neuchâtel, Examinateur

Faculté des Sciences
Secrétariat-décanat de Faculté
Rue Emile-Argand 11
2000 Neuchâtel – Suisse
Tél : + 41 (0)32 718 21 00
E-mail : secretariat.sciences@unine.ch

UNIVERSITÉ DE NEUCHÂTEL

IMPRIMATUR POUR THESE DE DOCTORAT

La Faculté des sciences de l'Université de Neuchâtel autorise l'impression de la présente thèse soutenue par

Monsieur Mohammadreza GHARAVIPOUR

Titre:

"Ramsey Spectroscopy in a Rubidium Vapor Cell and Realization of an Ultra-Stable Atomic Clock"

sur le rapport des membres du jury composé comme suit:

- Prof. Gaetano Mileti, directeur de thèse, Université de Neuchâtel, Suisse
- Dr Christoph Affolderbach, Université de Neuchâtel, Suisse
- Prof. James Camparo, Whittier College, Aerospace Corporation, Los Angeles, USA
- Prof. Branislav Jelenkovic, University of Belgrade, Serbia
- Dr Salvatore Micalizio, INRIM, Turin, Italie

Neuchâtel, le 28 juin 2018

Le Doyen, Prof. R. Bshary

Abstract

Keywords: Atomic clock, rubidium vapor cell, laser-microwave double-resonance, Ramsey scheme, frequency stability, metrology.

Various application fields in industry, telecommunication, navigation and space demand reliable, compact, high-performance frequency standards with a stability level of $<1\times10^{-14}$ at 10^5 s (equivalent to <1 ns/day). Thanks to semiconductor technology, optical pumping technique with a laser has opened up new schemes based on laser-microwave double-resonance (DR), such as continuous-wave (CW) and pulsed optical pumping (POP) to operate vapor cell atomic clocks.

In this thesis, we demonstrate the performances of a vapor cell Rubidium (Rb) atomic clock operating in a Ramsey-DR (based on POP) scheme in an ambient laboratory using a compact magnetron-type microwave cavity with a volume of only $45\,\mathrm{cm}^3$ and a low quality factor of ≈ 150. The Ramsey-DR scheme involves two resonant electromagnetic fields to interrogate the atoms - the *optical field* to polarize a population of atoms by optical pumping, and the *microwave field* to drive the ground-state hyperfine clock transition that serves as an atomic frequency reference. The applied optical and microwave pulses are separated in time in the Ramsey-DR scheme; therefore, the light shift (LS) effects can be strongly reduced which results in improving the clock stability. The magnetron-type microwave cavity is designed, developed and built in collaboration with Laboratory of ElectroMagnetics and Acoustics (LEMA) at Ecole Polytechnique Fédérale de Lausanne (EPFL)[1]. A newly home made vapor cell with a 10 times smaller stem volume compared to the previous contains ^{87}Rb and buffer gases of Argon and Nitrogen. The smaller stem results in reducing the stem temperature coefficient by about one order of magnitude, which has been a limiting factor for the medium- to long-term scales clock stability.

Detailed characterizations and performances of the clock signal (Ramsey central fringe) are presented in this study[2]. We obtain a clock signal with a contrast up to approximately 35% and a linewidth of approximately 160 Hz by optimizing the various parameters involved in the Ramsey-DR scheme. In our smaller cavity, these achievements are not trivial, because of the high requirements on field homogeneity over the entire cell volume are more challenging to meet. In this work, a short-term stability (1 s to 100 s) of $2.4\times10^{-13}\tau^{-1/2}$ is achieved which is comparable to the state-of-the-art results using the CW-DR scheme and/or using the POP scheme with a larger TE_{011} microwave cavity with a higher quality factor. The LS effect is quantified in our Ramsey-DR Rb atomic clock. In addition, we present a preliminary model based on the CW-DR LS theory and estimate the intensity LS coefficient in the Ramsey-DR scheme. Moreover, a new analytical expression is developed to predict the clock's short-term stability by considering the optical detection duration in the Ramsey-DR scheme. From this formula, we also estimate the best Ramsey time to improve the short-term stability of the clock.

This thesis, in addition, contains a more fundamental investigation on the measurements of the

[1]Within the projects Fonds National Suisse (FNS):"Microwave Cavities for High Performance Double Resonance Atomic Clocks and Sensors" no. 140712 (2012-2015) and "Study of microwave cavities for high performance pulse pumped double resonance atomic clocks" no. 162346 (2015-2018).

[2]Within the MClocks project: "Compact and High-Performing Microwave Clocks for Industrial Applications", EMRP (European Metrology Research Programme, Programme of Euramet) project IND55-Mclocks (2013-2016). The EMRP is jointly funded by the EMRP participating countries within EURAMET and the European Union.

population and coherence relaxation times (T_1 and T_2, respectively) of the ^{87}Rb "clock transition". This study has been performed in collaboration with the Institute of Physics Belgrade (University of Belgrade)[3]. These relaxation times are relevant for our Rb atomic clock, since they limit the usable "Ramsey time" in the Ramsey-DR scheme. An experimental method of Optically-Detected Spin-Echo (ODSE), inspired by classical nuclear magnetic resonance spin-echo, is developed to measure the ground-state relaxation times of ^{87}Rb atoms held in our buffer gas vapor cell. The ODSE method enables accessing the intrinsic T_2 (specific for the clock transition) by suppressing the decoherence arising from the inhomogeneity of the C-field across the vapor cell. The measured T_2 with the ODSE method is in good agreement with the theoretical prediction.

This work has been done at the Laboratoire Temps-Fréquence of University of Neuchâtel, in collaboration with the EPFL-LEMA for the magnetron-type microwave cavity, Istituto Nazionale di Ricerca Metrologica (INRIM) that provided the Local Oscillator (LO) and Physics Institute of Belgrade University for relaxation times measurements.

[3]Within the project FNS (SCOPES): "Ramsey spectroscopy in Rb vapor cells and application to atomic clocks" no. 152511 (2014-2018).

Résumé

Mots-clés: Horloge atomique, cellule à vapeur de rubidium, double résonnance laser et micro-onde, schéma Ramsey, stabilité en fréquence, métrologie.

Divers domaines d'application dans l'industrie, les télécommunications, la navigation et l'espace exigent des étalons de fréquence fiables, compacts et performants avec un niveau de stabilité de $<1\times10^{-14}$ à 10^5 s (équivalent à <1 ns/jour). Avec la technologie des lasers à semi-conducteurs, la technique du pompage optique par laser a ouvert de nouveaux schémas d'interrogation basés sur la double résonance (DR) laser et micro-ondes comme le pompage optique continu (CW) et le pompage optique pulsé (POP) qui sont utilisé pour faire de nouvelle horloges atomiques à cellules.

Dans cette thèse, nous présentons les performances d'un prototype de laboratoire d'horloge atomique à cellule à vapeur de Rubidium (Rb) fonctionnant avec un schéma Ramsey-DR (basé sur POP). L'horloge utilise une cavité micro-ondes compacte de type magnétron avec un volume de seulement 45 cm^3 et un faible facteur de qualité ($\approx$ 150). Le schéma Ramsey-DR utilise deux champs électromagnétiques résonants pour interroger les atomes - le champ optique pour polariser une population d'atomes par pompage optique, et le champ micro-ondes pour interroger la transition hyperfine de l'état fondamental qui est la fréquence atomique de référence. Les impulsions optiques et micro-ondes sont séparées dans le temps dans le schéma Ramsey-DR ; par conséquent, l'effet de biais de fréquence du à la lumière (light shift LS) peut être fortement réduit, ce qui améliore la stabilité de l'horloge. La cavité micro-ondes de type magnétron est conçue, développée et construite en collaboration avec le Laboratoire d'Electro-Magnétique et d'Acoustique (LEMA) de l'Ecole Polytechnique Fédérale de Lausanne (EPFL)[1]. Une cellule de verre nouvellement fabriquée au LTF avec un volume queusot 10 fois plus petit que la version précédente est remplie de ^{87}Rb et de gaz tampon d'Argon et Azote. Un queusot plus petit réduit le coefficient de température queusot d'environ un ordre de grandeur, ce qui a été un facteur limitant pour la stabilité de l'horloge à moyen et long terme.

Les caractérisations et performances détaillées du signal d'horloge (frange centrale du signal Ramsey) sont présentées dans cette étude[2]. Nous obtenons un signal d'horloge avec un contraste allant jusqu'à environ 35% et une largeur à mi-hauteur d'environ 160 Hz obtenu en optimisant les différents paramètres impliqués dans le schéma Ramsey-DR. Avec notre cavité plus petite, ces réalisations ne sont pas triviales, car les exigences élevées en matière d'homogénéité sur l'ensemble du volume de la cellule sont plus difficiles à satisfaire. Dans cette étude, on obtient une stabilité à court terme (1 s à 100 s) de $2.4\times10^{-13}\tau^{-1/2}$ ce qui est comparable à l'état-de-l'art en utilisant le schéma CW-DR et/ou en utilisant le schéma POP avec une cavité micro-ondes TE_{011} plus grande avec un facteur de qualité plus élevé. Le biais de fréquence du à la lumière (light shift) est quantifié dans notre horloge atomique Ramsey-DR Rb. De plus, nous présentons un modèle préliminaire basé sur le modèle du light-shift en mode continue

[1]Dans le cadre des projets du Fonds National Suisse (FNS):"Microwave Cavities for High Performance Double Resonance Atomic Clocks and Sensors" no. 140712 (2012-2015) et "Study of microwave cavities for high performance pulse pumped double resonance atomic clocks" no. 162346 (2015-2018).

[2]Dans le cadre du projet MClocks: "Compact and High-Performing Microwave Clocks for Industrial Applications", EMRP (European Metrology Research Programme, Programme of Euramet) project IND55-Mclocks (2013-2016). Le EMRP est conjointement financé les pays participant au EMRP qui dépend de EURAMET de l'union européen.

(CW-DR-LS) et estimons l'impact de l'intensité de la lumière (intensity light shift) dans le schéma Ramsey-DR. De plus, une nouvelle expression analytique est développée pour prédire la stabilité à court terme de l'horloge en considérant la durée de détection optique dans le schéma Ramsey-DR. A partir de cette formule, nous estimons également le meilleur temps Ramsey pour optimiser la stabilité à court terme de l'horloge.

Cette thèse contient en outre une étude plus fondamentale sur les temps de relaxation de la population et de la cohérence (T_1 et T_2, respectivement) de la "transition d'horloge" ^{87}Rb. Cette étude a été réalisée en collaboration avec l'Institut de physique de Belgrade (Université de Belgrade)[3]. Les temps de relaxation sont une donnée importante de notre horloge atomique Rb, car ils limitent le "temps de Ramsey" utilisable dans le schéma Ramsey-DR. Une méthode expérimentale de Echo de Spin Optiquement Détecté (Optically-Detected Spin-Echo ODSE), inspirée de l'écho de spin classique de la résonance magnétique nucléaire, est développée pour mesurer les temps de relaxation du rubidium 87 dans notre cellule. La méthode ODSE permet d'accéder au T_2 intrinsèque (spécifique pour la transition d'horloge) en supprimant la décohérence résultant de l'inhomogénéité du champ C à travers la cellule. Le T_2 mesuré avec la méthode ODSE est en accord avec la prédiction théorique.

Ce travail a été réalisé au Laboratoire Temps-Fréquence de l'Université de Neuchâtel, en collaboration avec l'EPFL-LEMA pour la cavité micro-ondes de type magnétron, l'Istituto Nazionale di Ricerca Metrologica (INRIM) pour l'oscillateur local (LO) et l'Institut de physique de l'Université de Belgrade pour les mesures des temps de relaxation.

[3] Dans le cadre du projet FNS (SCOPES): "Ramsey spectroscopy in Rb vapor cells and application to atomic clocks" no. 152511 (2014-2018).

Acknowledgements

This dissertation would not have been possible without supports and helps of many people. First of all, I would like to gratefully thank my adviser, Prof. Gaetano Mileti, who trusted me and gave me the opportunity to be a part of a well-known team, work in a great laboratory, introduce experienced nice colleagues and finally contribute in the success history of Laboratoire Temps-Fréquence. I am honored that I was his assistant for his Physics lecture in the University of Neuchâtel. I did not only learn about atomic physics and atomic frequency standards from Gaetano, but more importantly, I learned project management and project running from him. My second thank goes to Dr. Christoph Affolderbach, who my words fail me to appreciate his endless supports. He was always there, whenever I had questions and problems in the lab. Christoph was always aware of my coming technical difficulties, so I learned (at least tried) to pay attention to all his detailed explanations in advance. I would like to thank Dr. Songbai Kang who introduced me the characterization of atomic clocks for the first time.

I would like to thank all the jury members; Prof. James Camparo, Prof. Brana Jelenković and Dr. Salvatore Micalizo for their valuable comments and suggestions that were very helpful to improve the quality of this dissertation.

I was lucky to have such helpful and friendly colleagues at the LTF. Thank you Matthieu for helping me and being patient for all my scientific and personal friendly discussions. I really enjoyed having scientific discussions with you, although, convincing you was not an easy job. Thank you Florian for helping me in working with the laser systems. Thank you William for discussions about our Rb clock and for helping me in French. You were, are and will be one of my best friends in my life. Thank you Nil for helping me to edit this manuscript and I wish you a good luck with the Ramsey Rb clock. I would like to thank all the past and present colleagues at the LTF; Prof. Thomas Südmeyer, Renaud, Stéphane, Maxime, Valentin, Francois, Olga, Kutan, Sargis, Clément, Loïc, Nayara, Pierre, Norbert and Atif.

Within the LTF colleagues, I would like to specially thank our technical team, Patrick Scherler, for CAD designs, his expertise for tuning the magnetron cavity and his great skills in assembling the physics package and Marc Durrenberger for his helps and supports in electronic devices and for building laser and resonator controllers. I would like to thank Daniel Varidel for his experience in computer, network and electronics. I also thank the mechanical workshop people Christian Hêche and André Cornu.

I would like to thank all the LTF secretariats during almost last five years; Muriel, Sandrine, Natacha (God bless her), Joelle, Séverine and Patricia who supported and helped me in the administrative procedures.

I would like to thank our external collaborators. The team of LEMA-EPFL: Prof. Anja K. Skrivervik for her supports and Anton Ivanov for the simulations on the magnetron cavity and nice scientific discussions. Our collaborators from INRIM, Italy: Dr. Claudio Calosso, for building and providing the

LO in our lab. I would like to particularly thank our collaborators from institute of physics in Belgrade university; Prof. Brana Jelenković, Aleksandar Krmpot and Ivan Radojičić. The ODSE method would not be there without their great helps and supports.

I deeply thank my parents, my brother, Hamidreza, my sisters, Marjan and Aali, my uncle Mahmoud and my father, mother and sister in laws for their unconditional trust, great encouragement, and endless patience. And the last but not least, special thank with love to my wife, Zahra, and my son, Ariyan, who changed our life in last two years in the most positive way. Zahra has been my best friend, great companion and faithful supporter during the last ten years in my life and I would not obtain my PhD degree without her.

Neuchâtel, June 2018
Mohammadreza Gharavipour

Abbreviations

AM	**A**mplitude **M**odulation
AOM	**A**cousto-**O**ptic **M**odulator
BG	**B**uffer **G**as
CPT	**C**oherent **P**opulation **T**rapping
CW	**C**ontinuous **W**ave
DFB	**D**istributed **F**eed**B**ack
DR	**D**ouble **R**esonance
EMRP	**E**uropean **M**etrology **R**esearch **P**rogramme
EPFL	**E**cole **P**olytechnique **F**édérale de **L**ausanne
FNS	**F**ond **N**ational **S**uisse
FOF	**F**ield **O**rientation **F**actor
FM	**F**requency **M**odulation
FWHM ($\Delta\nu_{1/2}$)	**F**ull **W**idth at **H**alf **M**aximum
GPS	**G**lobal **P**ositioning **S**ystem
INRIM	**I**stituto **N**azionale di **R**icerca **M**etrologica
LEMA	**L**aboratory of **E**lectro**M**agnetics and **A**coustics
LH	**L**aser **H**ead
LO	**L**ocal **O**scillator
LTF	**L**aboiratoire **T**emps-**F**réquence
LS	**L**ight **S**hift
NMR	**N**uclear **M**agnetic **R**esonance
ODSE	**O**ptically **D**etected **S**pin **E**cho
PD	**P**hoto **D**etector
POP	**P**ulsed **O**ptically **P**umped
PS	**P**ower **S**hift
RCE	**R**esonator **C**ontrol **E**lectronics
RIN	**R**elative **I**ntensity **N**oise
SE	**S**pin **E**xchange
TC	**T**emperature **C**oefficient
TS	**T**emperature **S**hift

Physical Constants

Speed of Light	c	$299\,792\,458$ ms^{-1}
Free electron's Landé g-factor	g_S	$2.002\,0319\,304\,361\,53(53)$
Magnetic Constant	μ_0	$4\pi \times 10^{-7}$ NA^{-2}
Electric constant	ε_0	$8.854\,187\,817 \times 10^{-12}$ Fm$^{-1} = (\mu_0 c^2)^{-1}$
Bound electron's Landé g-factor ($5^2S_{1/2}$)	g_J	$2.002\,331\,13(20)$
^{87}Rb Nucleus' Landé g-factor	$g_{I_{87}}$	9.95141×10^{-4}
Bohr magneton $\frac{e\hbar}{2m_e}$	μ_B	$9.274\,009\,68(20) \times 10^{-24}$ JT^{-1}
Electron elementary charge	e	$1.602\,176\,565(35) \times 10^{-19}$ C
Electron mass	m_e	$9.109\,382\,91(40) \times 10^{-31}$ kg
Plank constant $\frac{h}{2\pi}$	$\hbar$	$1.054\,571\,726(47) \times 10^{-34}$ Js
Rb Second order Zeeman constant	K_C	575.15 HzG^{-2}

Notations

P_d	Input power of optical detection pulse
P_p	Input power of optical pumping pulse
t_d	Duration of the optical detection pulse
t_p	Duration of the optical pumping pulse
T_R	Duration of the Ramsey time
$\tau_{\mu w}$	Duration of the Rabi pulse
T_C	Duration of the cycle time
$f_C = \frac{1}{T_C}$	Cycle frequency
$\Delta\nu_{1/2}$	Full Width at Half Maximum (FWHM)
$\Delta\nu_{50\%}$	Full Width at Half Maximum (FWHM)
$\Delta\nu_{20\%}$	Full Width at 20% Maximum
Q_a	Atomic quality factor
Q_{cav}	Cavity quality factor
ξ	Field Orientation Factor (FOF)
T_{inv}	Inversion temperature
T_{cav}	Cavity temperature
T_{cell}	Vapor cell temperature
T_{stem}	Cell-stem temperature
TC_{cell}	Vapor cell temperature coefficient
TC_{stem}	Stem temperature coefficient
α_{LS}	Intensity light shift coefficient
β_{LS}	Frequency light shift coefficient
OD	Optical density
T_1	Intrinsic population relaxation time for the clock transition
T_2	Intrinsic coherence relaxation time for the clock transition
T_1'	Population relaxation time for *all* m_F levels
T_2^*	Coherence relaxation time for the clock transition with impact of C-field inhomogeneity

Contents

List of Figures

List of Tables

Introduction

Everyday life can hardly be imagined without considering the time interval measurement. In fact, answering questions such as "when did it happen?", "was it before or after the other event?", or "how long did it take?" requires a reference time scale and a clock to measure the time interval. To find a time reference, the basic idea is to choose a physical phenomenon that oscillates continuously at a constant rate, which is independent of position and environmental conditions. For centuries, the evolution and revolution of the earth (day-night cycle and year cycle respectively) were the reference "ticks". However, due to the irregularities in the rotations of the earth, another accurate reference with a shorter time scale period was required [1, 2]. In 1500 BC, ancient Egyptian and Babylonian astronomy used the first sundials clocks as timekeepers. This was followed by development various timekeepers such as candle clocks, water clocks and hourglass (sand clock) by different ancients during the history. In 1656, Christiaan Huygens invented the first pendulum clock as a mechanical clock operated based on a mechanism with a natural oscillation period. In 1880, Jacques and Pierre Curie discovered the piezoelectric properties of quartz [3] and less than fifty years later the first quartz clock was built by Marrison and Horton at Bell Telephone Laboratories in 1927 [4]. Quartz crystal clocks were not also a suitable candidate to be used in industrial fields such as telecommunications, navigation and space applications due to their drift in large time scales. Unlike the quartz clocks, atomic clocks are able to keep a stable and reliable time in the long-term scales. Advent of quantum mechanics revolutionized the understanding the nature at small scales [5]. In addition, the well-known Bohrs's relation presented that an atom in the energy state E_1 can be transferred to an excited state E_2 when it absorbs the energy of an incident electromagnetic field such that $E_2 - E_1 = h\nu$ where h is the Planck's constant and ν is the wave frequency. This was the main principle of invention of the atomic clocks. A transition started in 1939 after the discovery of nuclear magnetic resonance (NMR) by Rabi [6]. At the American Physical Society conference in 1945, Rabi announced plans for an atomic clock [7]. In 1949, Rabi in the National Institute of Standards and Technology (NIST) built the first atomic clock using ammonia molecules. In 1955, Essen and Parry designed and built the world's first Cesium (Cs) atomic clock at the National Physical Laboratory (NPL) [8]. In 1967 at the 13$^{\text{th}}$ "Conférence Générale des Poids et Mesures", the second was redefined as: "the duration of 9 192 631 770 periods of the radiation corresponding to the transition between the two hyperfine levels of the ground state of the ^{133}Cs atom".

In 1956, the world's first commercial Cs atomic clock was introduced about one year after the introduction of the NPL standard. Since then, various atomic clocks were developed such as; the thermal Cs beam standards [8, 9], primary atomic fountain clocks [10], active and passive hydrogen masers [11, 12], Rb vapor cell standards [13, 14], optical-lattice clocks [15] and ion-trap clocks [16, 17]. In the commercialization of atomic clocks, due to applications demands, many efforts have been undertaken not only to improve their accuracy performance, but also to reduce their volume, weight, power consumption and production costs. There exists applications, including satellite-based navigation systems, network synchronization, secure data communications and military systems that require atomic clocks combining excellent fractional frequency stability, low power consumption and small size. In the frequency standards domain, microwave vapor cell standards are particularly attractive and suitable candidates for meeting these criteria, since they are small and portable with low power consumption. For example each Galileo global navigation satellite system (GNSS)[1] contains two lamp-pumped rubidium atomic frequency standards (RAFS) and two passive hydrogen maser (PHM) atomic clocks. Some of characteristics of RAFS and PHM atomic clocks are listed in table 1 [18]. Photographs of RAFS and PHM atomic clocks are shown in figure 1. The goal for developing the next generation of the Rb atomic clock in Galileo GNSS is to improve its long-term stability performances below 10^{-14} (at the level of PHM) and keep it still compact. This project is ongoing among different experts time and frequency groups in Europe by replacing the laser technology instead of lamps and also using compact microwave cavities.

Table 1: Characteristics of RAFS and PHM in Galileo GNSS [18].

Clock	Stability at 1s	Stability at 10^4s	Mass (Kg)	Volume (L)	Power (W)
RAFS	3×10^{-12}	4×10^{-14}	3.3	3	18
PHM	7×10^{-13}	$<1\times10^{-14}$	18	28	80

RAFS PHM

Figure 1: Photographs of RAFS and PHM atomic clocks.

In 1950, discovery of optical pumping technique [19] by Kastler introduced the possibility to manipulate and spin-polarize atoms with coherent pumping light. This technique allowed the light spectroscopy and exploring energy levels of molecules and atoms. Development of laser technology resulted in improving the laser sources with narrow and tunable light with increased reliability and output power as well [20]. The Double-Resonance (DR) method with the optical pumping technique has been used to operate the vapor cell standards for about 70 years. The DR method involves two resonant electromagnetic fields; one in the optical domain and the other in the microwave domain. Since the 1960s, the vapor cell lamp-pumped Rb clocks have been used as time references in telecommunications and navigation systems with short-term frequency stability performances of about $1\times10^{-12}\,\tau^{-1/2}$ in terms of Allan deviation [13, 21]. However, Hao et al. have recently demonstrated a short-term stability of $2.4\times10^{-13}\,\tau^{-1/2}$ with a lamp-pumped clock [22]. The development of the semiconductor lasers in the 1980s opened new prospects in the field of vapor cell standards. Using a laser instead of the discharge lamp makes the system less bulky and the narrower linewidth of the laser compared to that of the lamp, results in more efficient optical pumping and consequently improves the short-term stability of the atomic clock by more than one order of magnitude [23, 24].

[1] Galileo GNSS is being created by the European Union (EU) through the European Space Agency (ESA).

In 2013, a large European project, named Mclocks [25] funded by EURAMET and led by S. Micalizio from Istituto Nazionale di Ricerca Metrologica (INRIM) was started in view of demonstrating highly compact vapor cell clocks and improving their performances by adopting interrogation schemes including mainly pulsed optical pumping (POP) and coherent population trapping (CPT). The main goal of the Mclocks project was the development of three types of Rb vapor cell clocks based on 1) CPT, 2) cold atoms and 3) POP schemes with the requirements of industrial and technical applications. The CPT principle [26] uses the concept of the so called dark-state and it occurs by connecting two ground-state energy levels of an atomic species to a common excited state using two phase-coherent optical fields frequency-split by the atomic ground state hyperfine frequency. In the frame of the Mclocks project, the Cs CPT clock with polarization modulation was developed recently at LNE-SYRTE in Paris [27, 28, 29] and achieved a short-term stability at the level of $3.2 \times 10^{-13}\,\tau^{-1/2}$. In cold atom clocks [30], atoms are first cooled by lasers and then interrogated by microwave field typically with Ramsey method. For example, HORACE [31, 32] is a compact cold atom clock developed in LNE-SYRTE in Paris. Recently, MuClock [33] which is an industrial compact version of HORACE has been developed and commercialized by Muquans (spin-off from Institut d'Optique and Observatoire de Paris) uses Rb atoms and demonstrated a short term stability at $\tau = 1$ s averaging time below 3×10^{-13}. These presented clocks are laboratory prototypes with massive volume and mass (360 liters and 80 kg in the case of MuClock, for instance). Micalizio et al. presented the state-of-the-art performance of a POP Rb atomic clock with a large TE_{011} cavity with a high quality factor at the level of $Q_{cav} \leq 1000$ inside a vacuum enclosure, exhibiting the short-term stability $1.7 \times 10^{-13}\,\tau^{-1/2}$ [34]. At the Laboratoire Temps-Fréquence (LTF) in the University of Neuchâtel, the state-of-the-art performance of an Rb standard exhibiting stability as low as $1.4 \times 10^{-13}\,\tau^{-1/2}$ was demonstrated [35] where the continuous-wave (CW) laser-pumped DR approach was used to operate the Rb clock in an ambient environment. However, it was shown that the medium- to long-term scale stability of the clock was limited by the light shifts (LS) effect and the stem temperature coefficient (TC).

In this thesis, we demonstrate an Rb clock using a compact magnetron-type microwave cavity [36] with a volume of only 45 cm^3 with a low quality factor (≈ 150) operating in the Ramsey-DR (based on POP) scheme and we show that the presence of a high-Q cavity is not required. The magnetron-type microwave cavity is designed and developed at the LTF in collaboration with the LEMA-EPFL [36]. In the Ramsey-DR scheme, in contrast to the CW-DR scheme, because the optical and microwave pulses are separated in time the LS effects can be strongly reduced and this results in improving the medium- to long-term stability of the clock. Simultaneously, a newly homemade (at the LTF) vapor cell with a stem volume 10 times smaller (compared to the previous version [35]) is used in our Rb clock, which reduces the stem TC by an order of magnitude with respect to the previous work. We note that, we operate our Ramsey-DR Rb clock in an ambient environment.

This thesis is split into five chapters as follows:

Chapter 1

This chapter presents a basic theory of the DR principle used in an Rb atomic clock. First, the atomic structure of the Rb atom in view of accessing its "clock levels" is presented. Then, an overview of the interaction of an atom with electromagnetic (optical and microwave) fields is given. This is followed by presenting the Ramsey-DR scheme for a three-level system. The "intrinsic" population and coherence relaxation times of the Rb atoms in our particular vapor cell are estimated based on the theory presented in [9]. Finally, principal effects leading to the short- and medium- to long-term frequency stability of the Rb clock are given.

Chapter 2

This chapter presents the experimental setup used in this thesis. The setup is the Rb atomic clock that is demonstrated in this thesis. It contains three main components: 1) a frequency-stabilized laser head (LH), 2) a physics package that consists of a microwave magnetron-type cavity and a vapor cell and 3) an electronic package. The detailed characterizations of each component are given in this chapter. Based on these characterization results, we demonstrate an Rb atomic clock operating in the Ramsey-DR scheme.

Chapter 3

This chapter gives the experimental measurements by using our Rb atomic clock. First, we show how to obtain a Ramsey pattern by operating our Rb clock in the Ramsey-DR scheme. The configuration of the $\pi/2$ microwave pulses is optimized based on Rabi oscillations. Then, the contrast of the clock signal, which is the central fringe of the Ramsey pattern, is optimized as a function of the durations and intensities of the optical pumping and optical detection pulses. We obtain a clock signal with a contrast of up to 35 % and a linewidth of 160 Hz. The uniformity of the microwave field is evaluated based on Rabi oscillations. The vapor cell and the stem temperature coefficients (TC) are presented. The LS coefficients and their impact on the clock frequency stability are measured and compared in our Rb clock operating in both the Ramsey-DR and CW-DR schemes. We use the LS theory and simulations in the CW-DR scheme and present a preliminary LS model and estimate the intensity LS in the Ramsey-DR scheme.The microwave power shift (PS) coefficient and its impact on the clock frequency stability are measured in our Ramsey-DR Rb clock. Moreover based on our investigations on microwave PS effect, we show how to suppress the this effect in our Ramsey-DR Rb clock. The short-term stability of $2.4 \times 10^{-13}\tau^{-1/2}$ is demonstrated for our Ramsey-DR Rb clock and validated with our newly presented analytical expression. We demonstrate our formula, in addition to estimate the short-term stability of our Rb clock, allows precise predictions of the best Ramsey time in the Ramsey-DR scheme. Finally, we present budget of instabilities in both short-term and medium- to long-term scales for our Ramsey-DR Rb clock based on the quantitative measurements of relevant instability sources.

Chapter 4

In this chapter, we measure the population and coherence relaxation times of Rb atoms in the vapor cell of our Rb atomic clock. For this, first, we use three existing methods of 1) Franzen [37], 2) CW-DR [35] and 3) Ramsey-DR [38]. Then, we introduce our proposed Optically-Detected Spin-Echo (ODSE) method inspired by NMR spin-echo [39] to measure both population and coherence relaxation times in our vapor cell. We demonstrate that, in contrast to the mentioned existing methods, the ODSE method suppresses the impact of the inhomogeneity of the static magnetic field on the coherence relaxation time in the vapor cell –which is a source of relaxation processes– and allows measuring the "intrinsic" coherence relaxation times of the atoms in the cell.

Chapter 5

A summary, conclusions and future prospects of this work are presented in this chapter.

1 Pulsed Double Resonance Atomic Clock

Atomic clocks, like other mechanical or electronic clocks, are used to keep track of the time interval based on oscillations. Generally, an oscillation is a periodic variation between two events. The number of these variations per unit of time is defined as the frequency of the oscillation. In mechanical clocks, for instance a pendulum clock, the pendulum is the clock's oscillator and the oscillations are the back and forth swinging motions of the pendulum. Similarly, in digital clocks, the oscillations of a quartz-crystal (resonator) are counted by a digital counter. In atomic clocks (atomic frequency standards), the atomic transition between two atomic states of a proposed element defines the oscillation. This atomic transition provides a stable frequency reference which is used to stabilize the frequency of a local oscillator. According to the Bohr atomic model, atoms can only make a transition between two energy eigenvalues, E_1 and E_2, by emitting or absorbing a photon whose energy is exactly equal to the energy difference between the two energy levels:

$$E_2 - E_1 = h\nu_B, \tag{1.1}$$

where h is the Planck constant and ν_B is the Bohr transition frequency. Based on this principle and the fact that the Bohr frequency is an inherent property of an atom, we can build an atomic clock by stabilizing the frequency of a local oscillator to the frequency of an atomic transition. A typical simple model of an atomic clock is shown in figure 1.1. In an atomic clock, a quartz-crystal plays the role of the local oscillator. An electronic servo-loop is used to stabilize the frequency of the quartz oscillator to the atomic frequency.

In this chapter, we present our studies on an Rb vapor cell atomic clock. Since the 1960s Rb vapor cell clocks have been used as time references in various applications such as telecommunication and navigation system for their several advantages: they are, for instance, reliable, easy to operate, compact, portable, consume less power, and last but not least have good short-term stability (around $10^{-12}\tau^{-1/2}$).

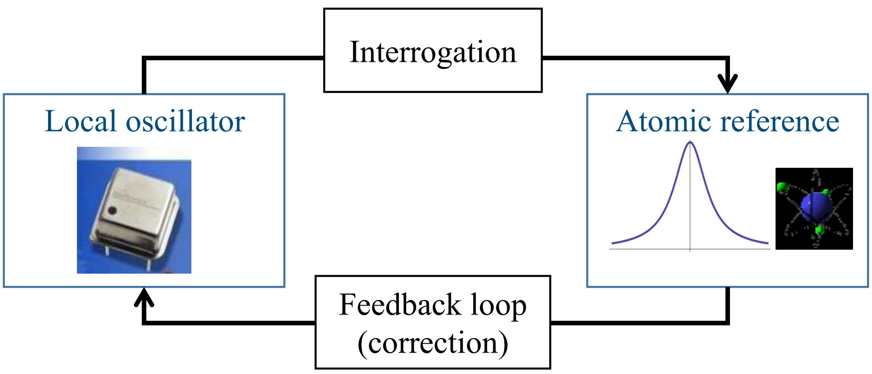

Figure 1.1: Basic principle in atomic clocks. The figure is taken from [40].

In our Rb atomic clock, the isotope ^{87}Rb is used as the atomic reference that is confined in a vapor cell.

This chapter starts with an overview of the Double-Resonance (DR) principle. Then, we present the atomic structure of the Rb atom. Considering the Rb atom as a simple three-level system, we present the optical-microwave DR theory to obtain the clock resonance line. Next, we introduce the Ramsey-DR technique which is used in this work to operate the Rb atomic clock. This is followed by presenting the relaxation mechanisms that occur in the vapor cell. Finally, the sources of frequency instabilities in our Rb clock are investigated.

1.1 Double-Resonance (DR) Principle

In vapor cell atomic clocks, a technique called "Optical-Microwave" DR is widely used to operate the clocks. This technique involves two electromagnetic fields interacting with an electric dipole transition, and a magnetic dipole transition where the laser is responsible for the electric dipole transition and the microwave radiation is responsible for the magnetic dipole transition. Figure 1.2 shows schematics of such a vapor cell atomic clock. In previous studies at the Laboratoire Temps-Fréquence (LTF), Bandi et al. [41] presented their investigations on an Rb atomic clock operating in the "Continuous-Wave Double-Resonance" (CW-DR) scheme where both laser and microwave fields are applied simultaneously to interrogate the atoms. In Bandi's work, the LS effect was one of the limiting factors of the medium- to long-term clock frequency stability [35]. In another approach, also with the DR technique, the pulsed-optical-pumped (POP) scheme was used to operate an Rb atomic clock [42, 43]. Using this scheme allows strong reduction of the LS effect because the optical pumping, microwave interrogation and optical detection phases are separated in time. In this thesis, we use the Ramsey-DR scheme [44] based on the POP scheme to operate our Rb atomic clock. The details of this scheme will be explained in section 1.5.

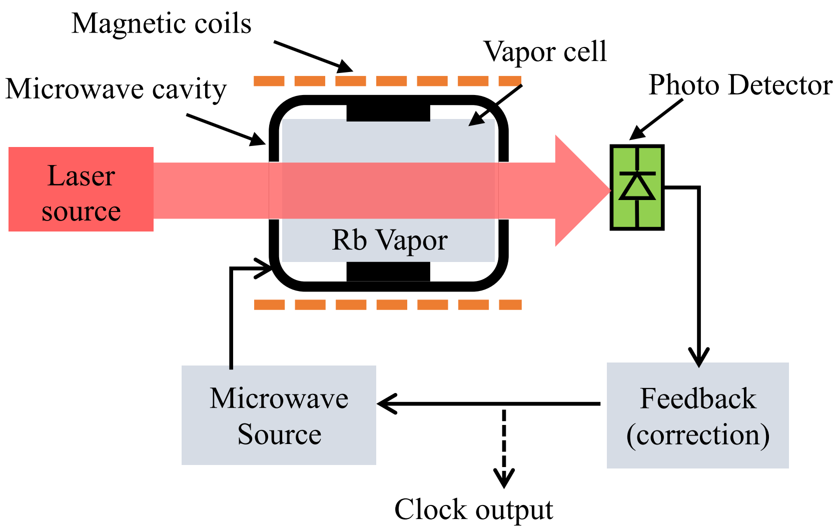

Figure 1.2: Schematics of a vapor cell atomic clock operating in the optical-microwave technique.

1.2 Rb Atomic Structure

Rubidium is an alkali metal element which is placed in the first group and fifth period of the periodic table. Two isotopes, ^{85}Rb and ^{87}Rb with abundances of 72% and 28% respectively, can be found in nature [45, 46]. Historically, the Rb atom is used essentially because of its optical spectral characteristic. The ^{87}Rb isotope is more favorable than ^{85}Rb because of its reduced number of ground states ($F = 1$ and $F = 2$ for ^{87}Rb in contrast to $F = 2$ and $F = 3$ for ^{85}Rb) allows a more efficient optical pumping. Therefore, our vapor cell is filled with ^{87}Rb.

Rubidium has the atomic number $Z = 37$; the first 36 electrons completely fill the first four atomic subshells, and it has one electron in its valence shell. This valence electron is placed in the $5S$ orbital and according to the quantum mechanic principles its total angular momentum is only possible of being $J = +1/2$[1]. The spin-orbit interaction is responsible for the atomic fine structure where their total electron angular momentum can be either $J = +1/2$ or $J = +3/2$ depending on the electron spin angular momentum S. These two atomic fine structures are shown by $5P_{1/2}$ and $5P_{3/2}$ as shown in figure 1.3. Moreover, due to the interaction (coupling) between the nucleus spin angular momentum, I, and the (total) angular momentum of the electron, J, the fine structure is split into a hyperfine structure characterized by the total angular momentum of the atom F. F can take the following range of integer values:

$$|J-I| \leq F \leq |J+I|. \tag{1.2}$$

The nuclear angular momentum I for ^{87}Rb is equal to $+3/2$. This information combined with equation (1.2) describes how the fine energy levels of $5S_{1/2}$, $5P_{1/2}$ and $5P_{3/2}$ split to two, two and four hyperfine energy levels respectively. The small nucleus spin of $I = \frac{3}{2}$ is one of the advantages of ^{87}Rb compared to $I = \frac{5}{2}$ in ^{85}Rb or $I = \frac{7}{2}$ in ^{133}Cs. The smaller I results in a smaller number of Zeeman levels that increases the population of the pair levels involved in the "clock transition" (see section 1.2.1) and consequently provides a larger signal [23]. Moreover, the ground state hyperfine transition frequency of 6.834 GHz can be easily synthesized from quartz oscillators [23]. The fine and hyperfine structures of ^{87}Rb are shown in figure 1.3. In ^{87}Rb, the two transitions of $5S_{1/2} \leftrightarrow 5P_{1/2}$ and $5S_{1/2} \leftrightarrow 5P_{3/2}$ are conventionally called D1-line and D2-line, respectively (see figure 1.3). D1-line has the wavelength of 795 nm and D2-line has the wavelength of 780 nm. In this thesis, we use the D2-line of the ^{87}Rb because the electric dipole moment of the optical transition in D2-line is approximately two times higher than the one of D1-line [45] which results in higher contrast of the resonance line [34].

1.2.1 ^{87}Rb Clock Transition

Applying an external static magnetic field (C-field) lifts the degeneracy of ^{87}Rb hyperfine ground states into their respective Zeeman levels. The direction of the C-field defines the z axis of the coordinate system and provides a quantization axis. Each hyperfine energy level with the total angular momentum of F splits into $2F+1$ Zeeman levels and the quantum number m_F is used to call them. The quantum number m_F can take the integer values of:

$$-F \leq m_F \leq F. \tag{1.3}$$

In ^{87}Rb, the hyperfine levels $|5S_{1/2}, F = 1\rangle$ and $|5S_{1/2}, F = 2\rangle$ split into three and five Zeeman energy levels respectively which are shown in figure 1.4. For ^{87}Rb atoms at zero C-field, the hyperfine frequency splitting is $E_{hfs}/h \approx 6.8$ GHz [45]. In the presence of a weak C-field, the Zeeman level shift is explained

[1] In quantum mechanics, the total angular momentum of an electron, j, is the sum of the orbital angular momentum of the electron, l, and the electron spin angular momentum, s, which mathematically is expressed by $j = |l \pm s|$.

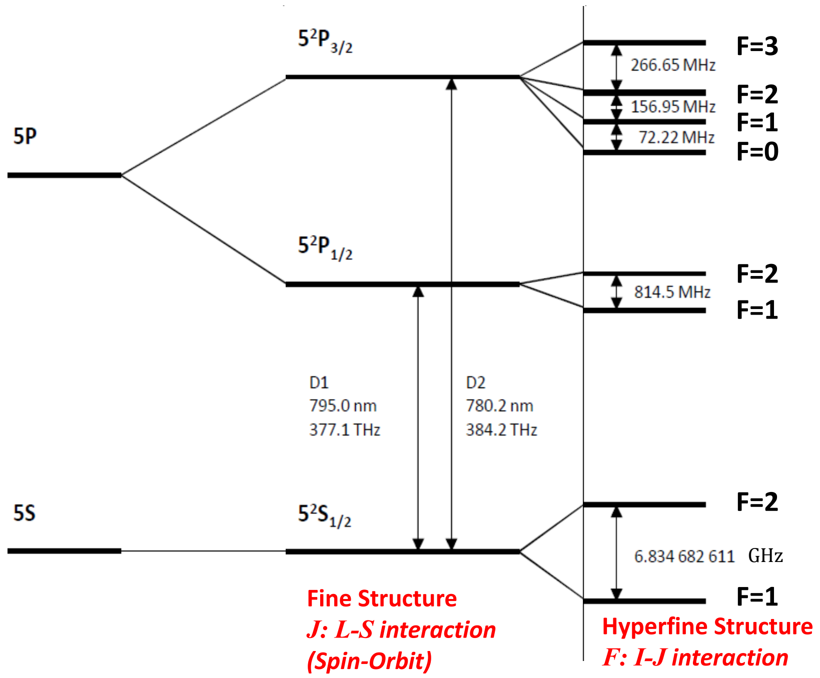

Figure 1.3: Fine and hyperfine structure of ^{87}Rb [45].

by the Breit-Rabi formula [9, 47] as:

$$E(F,m_f) = -\frac{E_{hfs}}{2(2I+1)} - g_I\mu_B B_0 m_F \pm \frac{E_{hfs}}{2}(1+\frac{4m_F}{2I+1}x+x^2)^{1/2} \tag{1.4}$$

where $\pm$ sign is taken to be the same as is $m_F = m_I \pm m_J$. I and g_I[1] are the nucleus spin angular momentum and Landé g-factor respectively, μ_B is the Bohr magneton, B_0 is the amplitude of the C-field and x reads as:

$$x = \frac{(g_J+g_I)\mu_B B_0}{E_{hfs}} \tag{1.5}$$

where g_J is the bound electron's Landé g-factor. By combining equations (1.4) and (1.5) and knowing $I = 3/2$ for ^{87}Rb, the frequency difference of $\nu_{(F=2,m_F)} - \nu_{(F=1,m_F)}$ can be calculated as a function of m_F and B_0:

$$\frac{E(F=2,m_{F_2}) - E(F=1,m_{F_1})}{h} = \frac{E_{hfs}}{h} + (m_{F_1}+m_{F_2})\frac{g_J\mu_B}{4h}B_0 + \frac{(g_J\mu_B)^2}{2hE_{hfs}}B_0^2. \tag{1.6}$$

This equation shows the corresponding Bohr frequencies of the allowed transitions (according to the selection rules within the ground state transitions can only happen when $\Delta m_F = m_{F_2} - m_{F_1} = 0, \pm 1$). The first term in equation (1.6) induces the hyperfine splitting $E_{HFS}/h = 6\,834\,682\,610.90429(9)$ Hz [48]. The second and third terms in equation (1.6) correspond to the linear and quadratic frequency shift with respect to the static magnetic field amplitude which can be given by $0.7\cdot(m_{F_1}+m_{F_2})$ MHz/G and 575.14 Hz/G^2 respectively after inserting the atomic constants [9]. Equation (1.6) shows that the transition between the two states of $|F=1, m_F=0\rangle$ and $|F=2, m_F=0\rangle$ is not affected by the C-field at the first order and it is much less affected by a weak C-field (below 100 mG) than any other transition (due the second term in equation (1.6) becomes zero). Therefore, the transition

[1] Note that in [9] the nucleus magnetic moment is defined as: $\vec{\mu}_I = g_I\mu_B(\frac{m_e}{m_p})\vec{I} \approx 5\times10^{-4} g_I\mu_B$, where m_e and m_p are the electron mass and proton mass respectively.

$|F=1, m_F=0\rangle \leftrightarrow |F=2, m_F=0\rangle$ is suitable to be chosen as the "clock transition", and these two states are called "clock levels" (see figure 1.4). The environmental magnetic field through the second order coefficient causes perturbations (section 1.7.3.1) and the magnetic shields are used to minimize this effect.

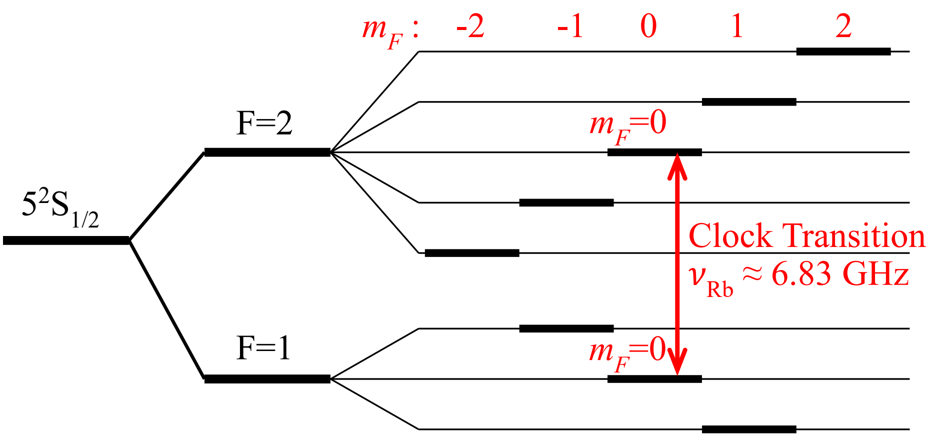

Figure 1.4: Zeeman splitting of $|5S_{1/2}, F=1\rangle$ and $|5S_{1/2}, F=2\rangle$ hyperfine levels of ^{87}Rb.

1.3 Atom-Fields Interaction in ^{87}Rb

The interaction of atoms with radiation fields is analyzed in density matrix formalism [49]. The time evolution of the atomic density matrix operator $\hat{\rho}$ under the action of Hamiltonian $\hat{H}$ is described by Liouville equation:

$$\frac{d}{dt}\rho = \frac{1}{i\hbar}[\hat{H}, \rho], \tag{1.7}$$

where, ρ is the density operator in the interaction and $\hat{H}$ includes contributions of the interaction of atoms with applied fields on the density matrices. Here, we consider ^{87}Rb atomic structure based on a three-level-system to simplify the presentation of the DR theory. The theory of DR technique is presented in detail in [9, 50, 51]. The schematic of the three-level-system for the ^{87}Rb is shown in figure 1.5. In this system, the three levels are: two ground states $|1\rangle$ and $|2\rangle$ and one excited state $|3\rangle$. However, in reality, the two ground states $F=1$ and $F=2$ of ^{87}Rb atoms consist of eight Zeeman sub-levels (see figure 1.4) and the excited state involves more than one level (see figure 1.3). The ground states $|1\rangle$ and $|2\rangle$ are associated with the clock levels of $|F=1, m_F=0\rangle$ and $|F=2, m_F=0\rangle$ in ^{87}Rb with the atomic transition frequency ω_{12}. The two ground state transitions are driven by a microwave radiation with an angular frequency of ω_μ. The excited state $|3\rangle$ corresponds to the $5^2P_{3/2}$ state in the ^{87}Rb atomic structure (see figure 1.3). The excited state $|3\rangle$ is used for the optical pumping with a laser at the frequency ω_L. In the following we describe interactions of the Rb atom with microwave and optical fields in the context of the Ramsey-DR scheme, which will be discussed more fully in section 1.5.

In addition to the applied fields, random perturbations also affect the states of the system and give rise to the relaxation phenomena. In analogy with NMR experiments, relaxations can be defined with two parameters of population relaxation and coherence relaxation. Population relaxation describes how the excited atoms relax back to thermal equilibrium, and coherence relaxation describes how the

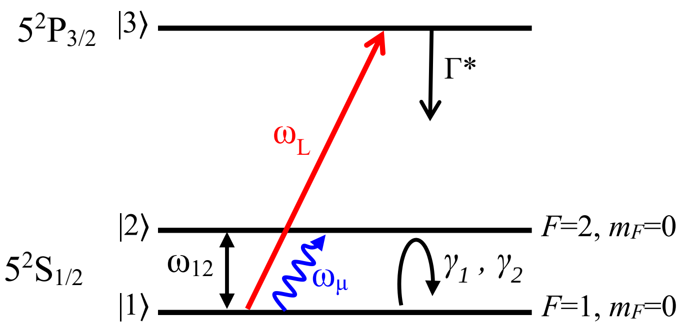

Figure 1.5: Schematic of a three-level-system in ^{87}Rb for a DR interrogation with laser-microwave fields.

coherent atoms lose coherence and relax back to zero due to the relaxation processes. The population relaxation time and the coherence relaxation time between the two ground states $|1\rangle$ and $|2\rangle$ are shown by T_1 and T_2 respectively. The relaxation rates, γ_i, (γ_1 and γ_2 are population and coherence relaxation rates, respectively) are the inverse of the relaxation times:

$$\gamma_i = \frac{1}{T_i}. \tag{1.8}$$

In atomic clocks, as in NMR experiments, various types of collisions of the atoms and also the inhomogeneity of the magnetic field are the relaxation sources. More details of the relaxation processes will be presented in section 1.6.

1.3.1 Interaction with Light: Optical Pumping

At a thermal equilibrium and in absence of any interaction field, according to the Boltzmann distribution, both ground states of ^{87}Rb atoms are approximately equally populated, and the excited state is empty. For example, at $T = 65°$C, the population ratio between the clock levels ($|1\rangle$ and $|2\rangle$), and the excited state ($|3\rangle$), are calculated by:

$$\frac{n_{|2\rangle}}{n_{|1\rangle}} = e^{\frac{-(E_2-E_1)}{k_B T}} \approx 0.999 \approx 1, \qquad \frac{n_{|3\rangle}}{n_{|2\rangle}} = e^{\frac{-(E_3-E_2)}{k_B T}} \approx 1.2\times10^{-24} \approx 0, \tag{1.9}$$

where $(E_2 - E_1)/h \approx 6.8\,\text{GHz}$ and $(E_2 - E_3)/h \approx 380\,\text{THz}$. The optical pumping technique [19] is used to create a population inversion between the two ground states and prepare the initial state. A schematic of optical pumping is shown in figure 1.6. The optical pumping is usually done with either a lamp [19, 52] or a laser [23]. Using a laser is more efficient than the lamp due to the higher intensity, narrower radiation spectrum and independence of filtering [23]. In our system, we shine the Rb vapor cell with a laser, whose frequency, ω_L, is tuned to a transition between a ground state and an excited state. For example, in our simplified three-level model, ω_L is tuned to the transition $|1\rangle \leftrightarrow |3\rangle$. In this condition, the Rb atoms are excited from the state $|1\rangle$ to the state $|3\rangle$ by absorbing light. Then, they may decay back from the state $|3\rangle$ to either ground states and repopulate them with an approximately equal probability (figure 1.6.b). If the laser continues to shine upon the atoms for a while, the atoms spontaneously decaying into the state $|1\rangle$ will be re-excited, whereas the atoms in the state $|2\rangle$ remain unaffected. As a result, after a number of excitation–emission cycles, all atoms will be found in the $|2\rangle$ state (figure 1.6.c).

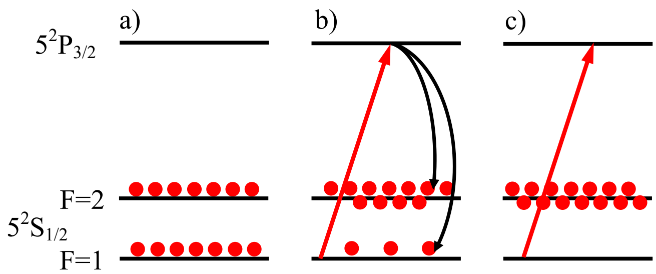

Figure 1.6: Schematic of optical pumping process: a) Atoms are in their thermal equilibrium condition and they equally occupy both ground states $F = 1$ and $F = 2$; b) the pumping laser whose frequency is tuned to the frequency between $F = 1$ and $F = 3$ ground states excites atoms from $F = 1$ ground states. Simultaneously, atoms may decay from the excited state back to either of the ground states; c) After a number of excitation–emission cycles, all of the population is pumped from $F = 1$ to the $F = 2$ state (in absence of relaxations between the ground state).

1.3.2 Microwave Interaction

As mentioned in section 1.2.1, in the Rb atomic clock, the two clock levels are involved in the clock transition. In this context, we consider only the two ground states $|1\rangle$ and $|2\rangle$ in the three-level-system and model the interaction of a microwave field on such a system. Microwave radiation is used to interrogate atoms in the ground states forming the clock levels. This is usually done with an oscillating microwave field which is produced by a microwave generator. Applying a microwave field, $\vec{B}(\vec{r},t) = \vec{B}_0 \cos(\omega_\mu t)$ perturbs the system. B_0 is the amplitude of the field and ω_μ is its angular frequency (see figure 1.5). We assume that the magnetic dipole moment arises from a single atom but the treatment can be generalized by summing over all of the atoms. Moreover, for simplicity we assume that the magnetic dipole moment is parallel to the microwave field and we neglect spatial variation of the magnetic field across the atom. The Rabi frequency of such a microwave field is written as:

$$b_e = \frac{\mu_B}{\hbar} B_z(r), \tag{1.10}$$

where μ_B is the Bohr magneton. For this system, the probability of finding the atom in state $|2\rangle$ at a time t is calculated by solving the time-dependent Schrödinger equation and is given by [51]:

$$P_2 = \frac{b_e^2}{b_e^{'2}} \sin^2\left(\frac{b_e^{'} t}{2}\right), \tag{1.11}$$

where $b_e^{'}$ is:

$$b_e^{'2} = b_e^2 + (\Delta\omega)^2. \tag{1.12}$$

$\Delta\omega = \omega_\mu - \omega_0$ is the frequency detuning between the angular frequency of the microwave field, ω_μ, and the atomic frequency between the two states, ω_0. If the microwave radiation occurs for a duration of τ_m, from equation (1.11), P_2 is written as:

$$P_2 = \frac{b_e^2}{b_e^{'2}} \sin^2\left(\frac{b_e^{'}\tau_m}{2}\right) = (b_e\tau_m/2)^2 \left(\frac{\sin(b_e^{'}\tau_m/2)}{b_e^{'}\tau_m/2}\right)^2. \tag{1.13}$$

P_2 has its maximum at the resonance condition when $\omega_\mu = \omega_0$ and its first minimum occurs at $\omega_\mu - \omega_0 = \pm 2\pi/\tau_m$. The probability function (1.13) has a (sinc $(x))^2$ shape[1] and its central peak full-width-at-half-

[1] $\mathrm{sinc}\,(x) = \frac{\sin(x)}{x}$.

maximum (FWHM), $\Delta\nu_{1/2}$, is the inverse of the interaction time τ_m [51]:

$$\Delta\nu_{1/2} = \frac{1}{\tau_m}. \tag{1.14}$$

Figure 1.7 shows P_2 as a function of $b_e t$ for three cases of frequency detuning $\Delta\omega$ is equal 0, b_e and $2b_e$. For zero detuning, P_2 increases to unity when the condition $b_e t = \pi$ is fulfilled. For non-zero detuning, by increasing the frequency detuning the maximum of P_2 decreases.

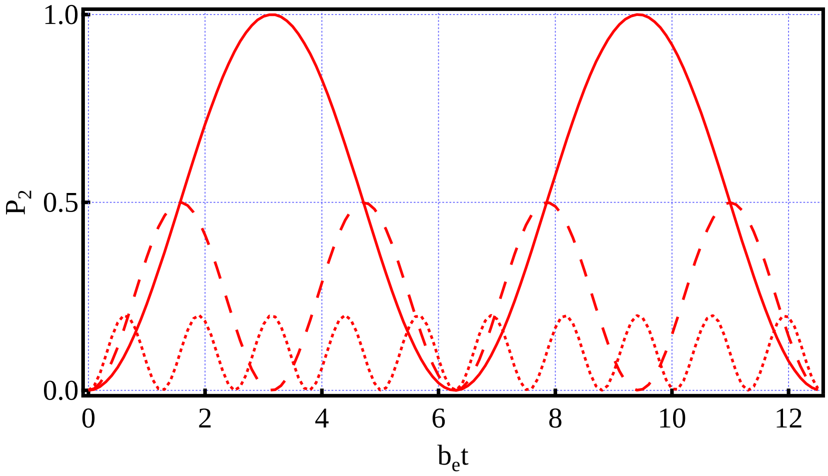

Figure 1.7: The probability function P_2 versus $b_e \cdot t$ for $\Delta\omega = 0$ (solid line), $\Delta\omega = b_e$ (dashed line) and $\Delta\omega = 2 \cdot b_e$ (dotted line).

1.3.2.1 Concepts of π and $\pi/2$ Pulses

Here, we present[2] the concept of a π (or $\pi/2$) pulse which is well-known in interferometry experiments. A π pulse with a duration of t_π, with a Rabi frequency of b_e and with an angular frequency in resonance with the frequency of an atomic transition can transfer the atomic population from one atomic level to the other, when the condition $t_\pi \cdot b_e = \pi$ is fulfilled. Similarly, for a $\pi/2$ pulse the condition $t_{\pi/2} \cdot b_e = \pi/2$ is fulfilled. If a $\pi/2$ pulse is applied to an atomic system with two atomic levels, a superposition of the states is created. In this condition, the probability of finding the atoms in each level is equal to 1/2. Technically, to create a π (or $\pi/2$) pulse the duration and the amplitude (which is proportional to the Rabi frequency) of the pulse should be adjusted (see section 3.1.1). We will explain the π and $\pi/2$ pulses in more details in section 1.4.

1.3.2.2 Interrogation by Two Microwave Pulses: Ramsey Technique

From equation (1.14), increasing the pulse duration, τ_m, results in a narrower signal which is of interest when considering atomic clocks. Rather than use this approach, N. Ramsey developed a smart method in the 1950s which is still being used in various atomic clocks [53, 44, 54]. The "Ramsey technique" is based on two identical electromagnetic pulses with the same duration of τ_m that are separated by an interval "Ramsey time", T_R, during which no electromagnetic field is applied. The timing sequence of the Ramsey technique is shown in figure 1.8.

To obtain the probability of finding an atom in the state $|2\rangle$ after the second pulse, Ramsey calculated

[2]This is valid for the ideal case where no relaxation process is taken into account.

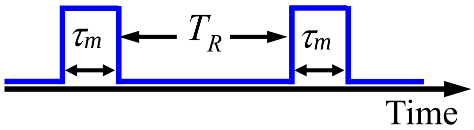

Figure 1.8: Timing sequence of the Ramsey scheme.

separately the probability amplitude after the first radiation and the probability amplitude after the second radiation and summed these two contributions [51]. Finally, the probability amplitude P_2 can read as [51, 53]:

$$P_2 = 4(\frac{b_e^2}{b_e'^2})\sin^2(\frac{b_e'\tau_m}{2})\Big(\cos\frac{b_e'\tau_m}{2}\cos\frac{\Delta\omega T_R}{2} - \frac{\Delta\omega}{b_e'}\sin\frac{b_e'\tau_m}{2}\sin\frac{\Delta\omega T_R}{2}\Big)^2, \tag{1.15}$$

where b_e is given by equation (1.10), b_e' is given by equation (1.12) and $\Delta\omega = \omega_\mu - \omega_0$ is the frequency detuning. Near the resonance, $\Delta\omega \ll b_e$ holds; therefore, we can neglect the second term in parentheses of equation (1.15), and it is reduced to:

$$P_2 = (b_e\tau_m)^2\Big(\frac{\sin(b_e'\tau_m)}{b_e'\tau_m}\Big)^2(\cos\frac{\Delta\omega T_R}{2})^2. \tag{1.16}$$

When the frequency of the applied microwave field is in resonance with atomic frequency i.e. $\omega \approx \omega_0$ then $\Delta\omega \approx 0$ and consequently $b_e \approx b_e'$. Then equation (1.16) can be written as:

$$P_2 \approx \frac{1}{2}\sin^2(b_e\tau_m)(1+\cos(\Delta\omega T_R)). \tag{1.17}$$

According to this equation, the optimal excitation of the atom is achieved when $b_e\tau_m = \pi/2$ and $\Delta\omega T_R = 2n\pi$. This means that in the Ramsey scheme when two resonant $\pi/2$ pulses are applied, they add together and act as a π pulse which results in the full transfer of the atomic population from one state to the other. Here, it is assumed that a zero phase shift occurs between the two pulses during the Ramsey time. The FWHM of the resonance curve can be calculated by [9, 51]:

$$\Delta\nu_{1/2} = \frac{1}{2T_R}. \tag{1.18}$$

Comparing equations (1.14) and (1.18) shows that, for the same interrogation time, the resolution obtained by the Ramsey technique is two times better than when one microwave pulse is applied. This is one of the advantages of the Ramsey technique.

1.4 Bloch Sphere

The Bloch representation was originally developed by Felix Bloch and modeled the Nuclear Magnetic Resonance (NMR) phenomena in 1946 [55]. It is known from NMR experiments that a spin 1/2 in the presence of a magnetic field splits into a doublet through the Zeeman effect. The Zeeman-split levels are formally equivalent to the two-level atom [56]. In 1957, Feynman et al. used this equivalence and adapted the Bloch representation to two-level atoms [57]. In the Bloch representation, poles of the Bloch sphere are used to represent geometrically pure states of a two-level system. A so-called "Bloch vector" describes the states in the Bloch sphere. The Bloch vector starts from the origin towards a point on the surface of the Bloch sphere. Figure 1.9 shows a typical Bloch sphere and a Bloch vector.

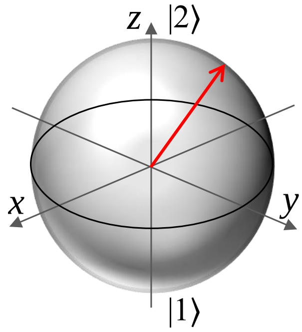

Figure 1.9: A typical Bloch sphere. The north and south poles correspond to state $|1\rangle$ and state $|2\rangle$ respectively. The states on the equator correspond to superposition states.

In the Bloch representation for a two-level system (with a ground state $|1\rangle$ and an exited state $|2\rangle$), the south and north poles of the Bloch sphere correspond to state $|1\rangle$ and $|2\rangle$ respectively. Whereas, the equator corresponds to the superpositions of the two states[1]. The magnitude of the z-component of the Bloch vector, gives the atomic population difference between the two states. Therefore, if all the atomic population fill the state $|1\rangle$ (or $|2\rangle$) and the state $|2\rangle$ (or $|1\rangle$) is empty, the Bloch vector is parallel to the z-axis and points to the south (north) pole of the Bloch sphere. If both states are equally and uncoherently populated, the Bloch vector is only a point in the center of the Bloch sphere. If the atoms are in coherent superposition state of the two states, the Bloch vector has a component in the xy plane. The Bloch sphere and the Bloch vector are particularly useful to visualize the atomic population of the clock levels in Rb atoms qualitatively in different sequences of pulsed techniques such as the Ramsey-DR and the Spin-Echo (see chapter 4) schemes. Figure 1.10.a shows a Bloch sphere that represents a two-level system in a condition that the state $|1\rangle$ is populated and the state $|2\rangle$ is empty. The Bloch vector pointing towards the south pole of the Bloch sphere. As discussed above, in a two-level system, an applied resonance π pulse results in transfer of the atoms from one state to the other. In the Bloch sphere, a resonance π pulse rotates the Bloch vector by an 180° angle around the x axis and flips it towards the north pole of the Bloch sphere (figure 1.10.b). Similarly, applying a resonance $\pi/2$ pulse is applied to the two-level system results in the creation of the superposition of the states and in the Bloch sphere; it rotates the Bloch vector by a 90° angle around the x axis and points towards the equator (figure 1.10.c). In our presentation, we have neglected the impact of any relaxation mechanism.

1.5 Ramsey-DR Scheme

In section 1.3.2.2, the Ramsey technique with microwave interactions was presented. In this section, we present the Ramsey-DR technique using optical-microwave DR technique. The Ramsey-DR scheme is based on the POP scheme [42]. This scheme is used in this thesis to operate the Rb atomic clock. In the Ramsey-DR technique, the light is used for optical pumping and optical detection, while the microwave field is used for atomic interrogation. Alley introduced the idea of pulsed optically pumping in 1960 [58]. His theory was developed by Arditi and Carver to make the first atomic clock that worked with microwave pulse coherent techniques [59]. In the Ramsey-DR scheme, in contrast to the CW-DR scheme, three phases of optical pumping, microwave interrogation and optical detection are separated in

[1]The choice of assigning the north and south poles of the Bloch sphere to the states is arbitrary.

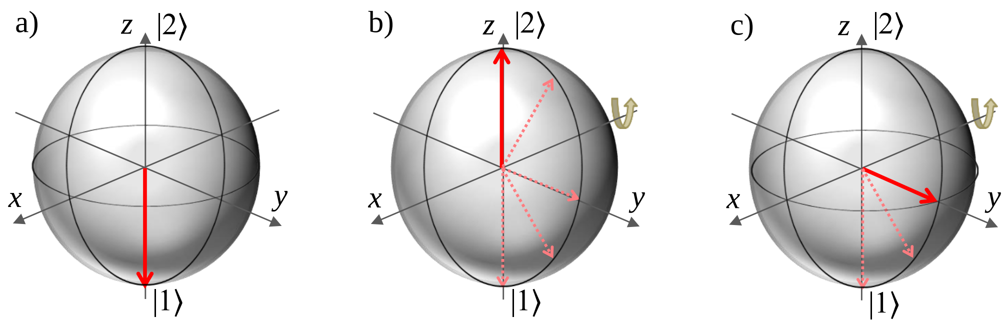

Figure 1.10: Representation of a two-level system with a Bloch sphere. a) the state $|1\rangle$ is populated and the state $|2\rangle$ is empty; therefore, the Bloch vector points towards the state $|1\rangle$. b) Applying a resonance π pulse results in rotation of the Bloch vector by an 180° angle around the x-axis and flips it towards the north pole of the Bloch sphere (the state $|2\rangle$). c) Applying a resonance $\pi/2$ pulse results in rotation of the Bloch vector by a 90° angle around the x-axis.

time. Therefore, during the optical pumping and optical detection no microwave radiation is applied and similarly during the microwave interrogation the light is off. This avoids the shift induced by optical coupling (light shift). The Ramsey-DR eliminates in principle the light shift (LS) effect [60, 61]. In the following we describe the various sequences of the Ramsey-DR scheme. For this, we consider the Rb atomic structure based on a three-level system that has been explained in section 1.3 and shown in figure 1.5.

The timing sequence of the Ramsey-DR scheme is shown in figure 1.11. In this scheme, the light is delivered by a laser source and the microwave radiation is provided by a microwave synthesizer. In the Ramsey-DR scheme, the first sequence is the optical pumping where a laser pulse with a duration of t_p creates a population imbalance between the ground states $|1\rangle$ and $|2\rangle$ via the excited state. After the optical pumping pulse, the initial state is created (figure 1.11c). Then, in the absence of the light, the microwave radiation is used to drive the ground state transition (the clock transition $|F=1,\, m_F=0\rangle \leftrightarrow |F=2,\, m_F=0\rangle$ in our atomic clock). In the Ramsey-DR scheme, the microwave interrogation is defined by two $\pi/2$ pulses that are separated with an interval Ramsey time T_R. The $\pi/2$ pulses have the same frequency, intensity, and the duration, τ_m. The first $\pi/2$ microwave pulse creates a coherent superposition state. During the Ramsey time, atomic spins continue their free evolution at their Larmor frequency. Since the frequency of the microwave field is in resonance with the atomic frequency between the ground state levels (clock frequency of Rb atoms in our atomic clock), the condition $\Delta\omega T_R = 2n\pi$ in equation (1.17) is fulfilled. Therefore, the second resonant $\pi/2$ microwave pulse converts the accumulated atomic phase into a population difference between the ground states. Finally, in the last part of the sequence, the optical detection pulse with the duration of t_d takes place by a laser with the same frequency as during optical pumping. The laser amplitude in the optical detection is much lower than during the optical pumping to avoid further repumping of the atoms. The sequence of the Ramsey interaction in a three-level system with a representation of the Bloch vector during the microwave interrogation is illustrated in figure 1.11.

Using the Ramsey scheme, a transmission signal as a function of the frequency of the microwave field gives the Ramsey pattern, which is a measure of the atomic ground state polarization. The stabilization of the quartz oscillator to the central fringe of the Ramsey pattern realizes the clock [13, 23]. In section 3.1, various Ramsey patterns that are obtained experimentally at various operating parameters will be presented and discussed.

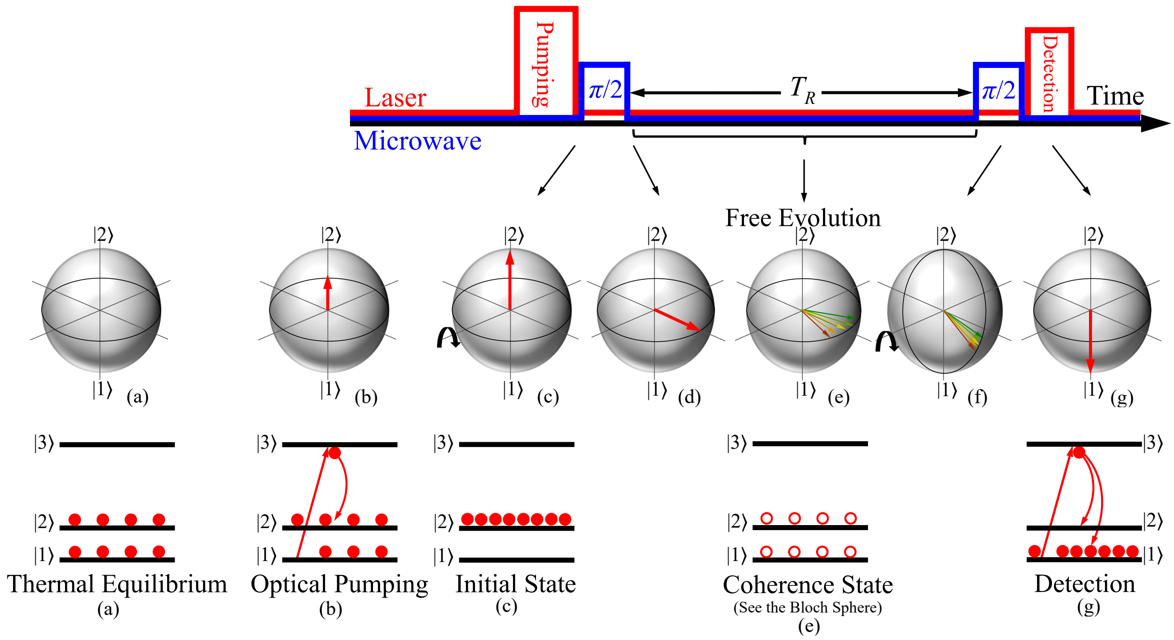

Figure 1.11: Ramsey-DR scheme.
Upper: Timing sequence of the Ramsey-DR scheme. Middle: State evolution represented by the Bloch sphere
Bottom: Schematic representation of the Ramsey-DR scheme in a three-level system.
(a): Atoms are at thermal equilibrium. Both ground state levels are equally populated due to the Boltzmann distribution.
(b): During the optical pumping only the laser is on. During this interaction, excited atoms stay for a short time ($\approx$ nanosecond) in the excited state $|3\rangle$ and then randomly decay back to the ground state $|1\rangle$ or $|2\rangle$. The optical pumping makes level $|1\rangle$ depopulated.
(c): Optical pumping creates a population imbalance between the ground states and prepares the initial state (no relaxation is considered). Bloch vector represents the atoms that are in level $|2\rangle$.
(d): The first $\pi/2$ pulse is applied after the optical pumping. The Bloch vector rotates 90°.
(e): The first $\pi/2$ pulse creates a coherent superposition state. Then during the Ramsey time both laser and microwave are off. During T_R, the Bloch vector represents the free evolution of spins at the Larmor frequency.
(f): The second $\pi/2$ pulse brings all the components of the diffused vector to the population difference axis (vertical). The Bloch vector rotates another 90°.
(g): During the optical detection, in absence of the microwave, atoms in level are detected optically with the laser. Bloch vector represents the atoms in the level $|1\rangle$.

1.6 Intrinsic Relaxations in a Vapor Cell

In a vapor cell atomic clock, the linewidth (in the case of the CW-DR scheme) and the contrast of the resonance line are influenced by various parameters, and ultimately, by the relaxation processes occurring in the cell. Alkali atoms in the vapor cell, like in NMR, may lose their polarization due to various types of collisions, interactions with electromagnetic fields, or as a result of the inhomogeneity of the static magnetic field.

In our Rb atomic clock, the Rb atoms are confined in a vapor cell in the presence of buffer gases. Buffer gases are used to reduce the mean free path of the rubidium atoms by preventing them to collide directly with the vapor cell's walls and lose their polarization. Rubidium atoms may collide with the cell walls, buffer gases and with other Rb atoms (this process is called spin exchange) and lose their polarization. These collisional relaxations depend only on the cell design (dimensions and geometries), cell temperature and pressure, but they do not depend on any electromagnetic field. Therefore, they are known as "intrinsic" relaxations [62]. One can estimate the total intrinsic relaxation rates by summing the contributions of the three collisional relaxations: cell wall collisions γ_{iCW}, buffer-gas collisions γ_{iBG} and spin exchange γ_{iSE}:

$$\gamma_i = \gamma_{iCW} + \gamma_{iBG} + \gamma_{iSE}. \tag{1.19}$$

In the following, we give an overview of each of these relaxation sources. We use the relaxation theory and formula presented in [9] to estimate the intrinsic population and intrinsic coherence relaxation times in our particular vapor cell (see section 2.3.1) and particular experimental conditions. The estimated intrinsic relaxation times are valid only for the clock transition of ^{87}Rb atoms and we use notation T_i to show them.

1.6.1 Cell-Wall Relaxations

Buffer gases are used in the vapor cells for various reasons. The most important one is to prevent the Rb atoms from colliding directly with the cell walls, because the cell wall collisions induce relaxations. The Rb atoms collide with the cell walls and lose the state of polarization. The motion of atoms through buffer gases can be explained by the diffusion equation which depends on the cell dimension, cell temperature, T, and buffer-gas pressures in the cell, P. Our vapor cell has a cylindrical geometry with a radius of $a = 1.25$ cm and length of $L = 1.25$ cm. In the lowest order diffusion approximation, the diffusion equations responsible for the populations and coherence relaxations, respectively, are given by [9]:

$$\gamma_{iCW} = \Big[(\frac{2.405^2}{a^2} + \frac{\pi^2}{L^2}) D_0 \frac{P_0}{P} \Big], \tag{1.20}$$

where D_0 are the diffusion constants proportional to $T^{3/2}$ and P_0 is the standard atmospheric pressure (760 Torr= 1013.25 mbar). The diffusion constants, D_0, for Rb atoms with Argon (Ar) and Nitrogen (N_2) at temperature $T = 27$°C were measured in [63]. Table 1.1 presents the diffusion constants, D_0 for our vapor cell at the cell temperature of $T = 64$°C. The total buffer-gas pressure $P = 25$ Torr. For our vapor cell, based on the experimental measured parameters in table 1.1 and the cell dimensions, the cell-wall population and coherence relaxation rates are calculated with equation (1.20) and are given in table 1.3.

Table 1.1: Diffusion constants of Rb interacting with buffer gases [9].

Buffer Gas	D_0 (m^2s^{-1})
Ar	1.54×10^{-5}
N_2	1.66×10^{-5}

1.6.2 Buffer Gas Relaxations

Adding buffer gases leads to increasing the flight time that Rb atoms need to reach the cell walls, or in other words, they reduce the mean free path of Rb atoms from a few centimeters to a few micrometers in a vapor cell. N_2 and Ar are used as buffer gases in our vapor cell. Nitrogen has been chosen because of its large quenching cross section that can reduce the lifetime of the excited states in Rb atoms [9]. However, N2 induces a positive pressure shift and it is mixed with Ar with a negative pressure shift. Collisions of Rb atoms with buffer gases change the electron density at the Rb nucleus and result in changing the hyperfine coupling in the Rb atoms [64] and consequently results in line broadening. The relaxation rates that arise from collisions between a Rb atom and the buffer gas (molecules or atoms) depend on the collisional cross-sections between the Rb atom and the buffer gas, σ, the cell temperature, and the buffer-gas pressures P with:

$$\gamma_{iBG} = L_0 \bar{v}_r \sigma_i \frac{P}{P_0}, \tag{1.21}$$

where $L_0 = 2.6867774(47) \times 10^{25}$ m^{-3} at 0°C is Loschmidt's constant. σ_1 is the collisional cross-section responsible for population relaxation, and σ_2 is the collisional cross-section responsible for the coherence relaxation. The temperature dependence of the above equation appears in the mean velocity of the colliding atoms and buffer gases, $\bar{v}_r$ which is given by:

$$\bar{v}_r = \sqrt{\frac{8k_BT}{\pi\mu}}, \tag{1.22}$$

where T is the cell temperature in Kelvin unit. k_B is the Boltzmann constant and μ is the reduced mass of the colliding particles. The collision cross-sections between Rb atoms with Ar and N_2 buffer gases responsible for population and coherence relaxations that are obtained experimentally [9] are given in table 1.2.

Table 1.2: Collisional cross-sections of Rb with Ar and N_2 [9].

Collisions	σ_1 (m^2)	σ_2 (m^2)
Rb-Ar	37×10^{-27}	37×10^{-27}
Rb-N_2	8.3×10^{-27}	350×10^{-27}

The contribution of the population and coherence relaxation rates induced by each buffer gas are calculated by using equation (1.21) and the coefficients in table 1.2 at the working conditions of P = 25 Torr and the cell temperature $T = 64\,°$C. In our Rb vapor cell with Ar and N_2 buffer-gas mixture, the buffer-gas vapor pressure ratio is $r = P_{Ar}/P_{N_2} = 1.6$. The population and coherence relaxation rates, γ_{1BG} and γ_{2BG} respectively, for such a mixture are obtained from the formula below and the results are given in table 1.3.

$$\gamma_{i(Ar+N_2)} = \frac{r\gamma_{i(Ar)} + \gamma_{i(N_2)}}{r+1}. \tag{1.23}$$

1.6.3 Spin Exchange Relaxations

In the vapor cell, Rb atoms may collide with other Rb atoms. This collision type may also result in a line broadening [9]. During this collision, the two atoms in $S_{1/2}$ state with opposite spins collide and spin states of the two atoms may exchange with conservation of the total spin [65]. This phenomenon is called spin-exchange. The spin-exchange collision relaxation is characterized by the cross section σ_{SE}. The spin-exchange relaxation rates are calculated as [9, 66]:

$$\gamma_{1SE} = n\bar{v}_r\sigma_{SE} \quad , \quad \gamma_{2SE} = \frac{6I+1}{8I+4}\gamma_{1SE}, \tag{1.24}$$

where γ_{1SE} and γ_{2SE} are the spin-exchange relaxation rates of the atomic populations and coherence, respectively. n is the atomic density of the Rb atoms in the vapor cell, $\bar{v}_r$ is the average relative velocity of the Rb atoms (equation (1.22)) and Rb-Rb spin exchange cross section is $\sigma_{SE} = 1.6 \times 10^{-18}\mathrm{m}^2$ [9, 66]. I is the nuclear spin which for ^{87}Rb is $\frac{3}{2}$. By applying these values to the above equations, spin-exchange relaxation rates are calculated and are given in table 1.3.

1.6.4 Summary of Intrinsic Relaxation

All of the above contributions to the intrinsic population and coherence relaxation rates are given in table 1.3. The total expected relaxation rates in our cell are calculated with equation (1.19). Finally, both intrinsic relaxation times, particularly, for the clock transition are calculated (inverse of the relaxation rates) to be $T_1 \approx T_2 = 4.5$ ms. The reported literature values for D_0 and σ_i show considerable scatter [37, 63, 67, 68], which result in a total uncertainty of %7 for both intrinsic T_1 and T_2.

Table 1.3: Calculated intrinsic relaxation rates/times in Rb vapor cell, at T = 64 K

	γ_1 (s^{-1})	γ_2 (s^{-1})
Diffusion to cell walls (γ_{iCW})	25	25
Buffer gas collisions (γ_{iBG})	12	79
Spin-exchange (γ_{iSE})	185	116
Total relaxation rates ($\Sigma\gamma_i$)	222	220
Estimated relaxation times (ms)	T_1 = 4.5	T_2 = 4.5

1.7 Frequency Instabilities in an Rb Atomic Clock

To characterize an oscillator or an atomic clock, frequency accuracy and stability of the oscillator are key values. Accuracy describes the deviation of an averaged measurement value from the standard of the quantity being measured. The instantaneous frequency of an oscillator may vary with time. This random variation is known as oscillator instability. In other words, the stability of an oscillator defines how well it can reproduce the same frequency over a given time. Typically, there are two types of instabilities: 1) short-term instabilities and 2) long-term instabilities. In Rb high-performance atomic clocks, short-term instabilities refer to fluctuation over an interval time 0.1 s to 100 s and long-term instabilities to longer than 10000 s. These ranges can be varied for different applications. Generally, the frequency of an oscillator is non-stationary data because it contains time dependent noise contributions in itself. This is the main reason that the standard deviation does not work to estimate the frequency stability of an oscillator. Instead of the standard deviation method, a statistic method called Allan deviation is used to estimate stability in the time domain. In the following we present more details about the Allan deviation and various sources of instability in our Rb atomic clock.

1.7.1 Allan Deviation

David W. Allan introduced the two-sample variance in order to identify frequency noise processes such as white, flicker and random walk frequency noises and characterize the variations of the oscillator over time due to different noise processes [69]. The Allan variance is widely used to measure the frequency stability in atomic clocks and oscillators. The Allan variance is expressed mathematically as $\sigma_y^2(\tau)$ and its square root is the Allan deviation. The stability of an atomic standard's frequency is investigated in the time domain.

The output frequency of the clock under test, $y(t)$, is measured at regular time intervals of τ, where $\tau = t_{i+1} - t_i$. An example of the signal used for the Allan variance calculation is shown in figure 1.12. The mean clock fractional frequency $\overline{y_i}$, is given by:

$$\overline{y_i} = \frac{1}{\tau}\int_{t_i}^{t_{i+1}} y(t)dt, \tag{1.25}$$

and the Allan deviation for N number of samples can be calculated as [69]:

$$\sigma_y(\tau)_{Allan} = \sqrt{\frac{1}{2}\langle(\overline{y_{i+1}} - \overline{y_i})^2\rangle} = \sqrt{\frac{1}{2(N-1)}\sum_{i=1}^{N-1}(\overline{y_{i+1}} - \overline{y_i})^2}. \tag{1.26}$$

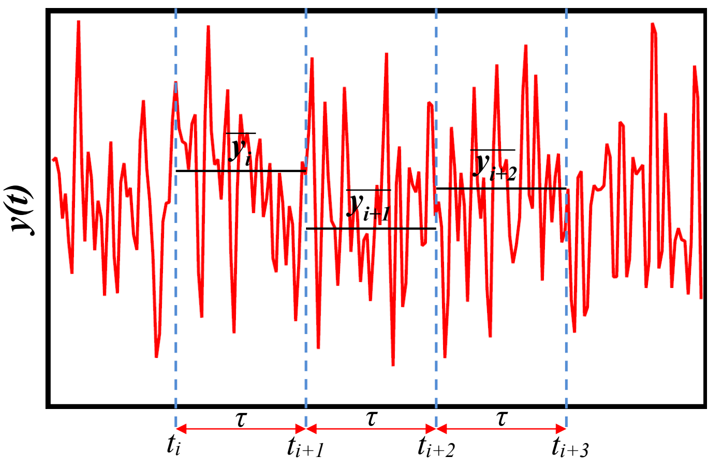

Figure 1.12: Typical frequency fluctuations of an atomic standard or oscillator.

For a set of N frequency measurements, the averaging time $\tau = m\tau_0$ and the overlapping Allan deviation is defined as [70],

$$\sigma_y(\tau) = \sigma_y(m\tau_0) = \sqrt{\frac{1}{2m^2(N-2m+1)} \sum_{j=1}^{N-2m+1} \sum_{i=j}^{j+m-1} (\overline{y_{i+m}} - \overline{y_i})^2}. \tag{1.27}$$

1.7.2 Short-Term Frequency Stability

It was mentioned before that the short-term frequency stability typically refers to the stability of a measured frequency signal over an interval time of less than 100 seconds. In an atomic clock, various sources of instabilities such as fluctuations of the C-filed, intensity and frequency of the laser, amplitude and phase noise of the applied microwave radiation can limit the short-term frequency stability. In our Rb atomic clock operating in the Ramsey-DR scheme with optical detection, instability sources are mainly among: the instability associated with the total optical detection noise, phase noise of microwave interrogating through the Dick effect [71] and LS via the laser intensity noise and the laser frequency noise. In this section, we present the contributions of these sources in terms of Allan deviation. The total short-term frequency instability is given by summation of all the above noise contributions in terms of Allan variance and it is given by:

$$\sigma_y^2(\tau) = \left(\sigma_y^{det}(\tau)\right)^2 + \left(\sigma_y^{LO}(\tau)\right)^2 + \left(\sigma_y^{LS}(\tau)\right)^2, \tag{1.28}$$

where $\sigma_y^{det}(\tau)$ is the instability associated with the total optical detection noise, $\sigma_y^{LO}(\tau)$ with the phase noise of the microwave interrogating and $\sigma_y^{LS}(\tau)$ with the instability due to the intensity and frequency light shifts via the laser intensity noise and the laser frequency noise. In the following, we explain each of these limitation factors in more details. $\sigma_y^2(\tau)$ in equation (1.28) has instability contributions induced by fluctuations of other parameters such as: C-field, atmospheric pressure and temperature, but their fluctuations in the short-term scale (around 1 s) are quite low. Thus, these contributions are neglected in the above equation.

1.7.2.1 Optical Detection Stability Limit

A single-frequency laser, such as the one used in our Rb atomic clock (see section 2.2.), can be characterized by intensity noise (or amplitude noise) and phase noise. The instability induced by the laser detection noise includes shot noise, the laser's amplitude modulation (AM) noise, additional AM noise from the Acousto Optical Modulator (AOM) and the noise from frequency-modulation (FM) noise (laser+AOM) to AM noise conversion in the vapor cell [72].

The shot-noise-limit is the lowest possible intensity noise level for a laser beam observed in measurements with a photodiode. The theoretical shot-noise-limit in an atomic clock operating in the Ramsey-DR scheme with the optical detection can be expressed as [34]:

$$\sigma_y^{SN}(\tau) = \frac{1}{\pi Q_a R_{SN}} \sqrt{T_C}\, \tau^{-1/2}, \tag{1.29}$$

where Q_a is the atomic quality factor which is given by:

$$Q_a = \frac{\nu_{Rb}}{\Delta\nu_{1/2}}, \tag{1.30}$$

where $\Delta\nu_{1/2}$ is the linewidth of the atomic resonance line which in our case is the linewidth of the Ramsey central fringe, and ν_{Rb} is the frequency of the clock transition in an Rb atom. In equation (1.29), R_{SN} is the signal-to-noise ratio which is proportional to the contrast of the Ramsey central fringe and T_C is the cycle time of the Ramsey-DR scheme.

In this section we investigate the optical detection noise's influence on the clock's stability based on our newly developed theory presented in Ref. [73]. In an atomic clock operating in pulsed mode like the Ramsey-DR scheme with optical detection, the periodic optical detection also causes down-conversion of out-of-band AM noise near the cycle frequency f_C ($= \frac{1}{T_C}$) and its harmonics. The fluctuations of the laser amplitude during the optical detection phase induce further instabilities to the clock frequency. We use a so-called "sensitivity function" $g(t)$, which is the response of the atomic system to a phase step of the interrogating oscillator with respect to a frequency change occurring at time t [71]. In our particular Ramsey-DR scheme with an optical detection, the sensitivity function is defined by:

$$g(t) = \begin{cases} 0, & 0 \leqslant t < T_C - t_d \\ 1, & T_C - t_d \leqslant t \leqslant T_C \end{cases}, \tag{1.31}$$

where t_d is the duration of the optical detection phase in the Ramsey-DR scheme. For this sensitivity function $g(t)$, the Fourier coefficients g_n^s and g_n^c at n^{th} harmonics of f_C and the average value g_0 are respectively given by:

$$g_n^s = \frac{1}{T_C}\int_0^{T_C} g(t)\sin(\frac{2\pi nt}{T_C})dt, n \text{ is an integer} \tag{1.32a}$$

$$g_n^c = \frac{1}{T_C}\int_0^{T_C} g(t)\cos(\frac{2\pi nt}{T_C})dt, n \text{ is an integer} \tag{1.32b}$$

$$g_0 = \frac{1}{T_C}\int_0^{T_C} g(t)dt. \tag{1.32c}$$

At very low frequencies, the down-converted detection noise can be assumed white and will be completely compensated in a closed frequency loop [74, 75]. Therefore, the final white AM clock loop noise $S_{RIN}^{LLO}(0)$ in the narrow range (at frequencies both above and below harmonics nf_C) is [75]:

$$\begin{aligned} S_{RIN}^{LLO}(0) =& 2\sum_{n=1}^{\infty} \frac{(g_n^s)^2 + (g_n^c)^2}{(g_0)^2} S_{RIN}^{det}(nf_C) \\ =& 2\sum_{n=1}^{\infty} (\mathrm{sinc}\,(\pi n f_C t_d))^2 S_{RIN}^{det}(nf_C), \end{aligned} \tag{1.33}$$

where $S_{RIN}^{det}(f)$ is the power spectral density of the relative intensity noise (RIN) of the optical detection signal. For a given detection time t_d, the corresponding white AM noise variance σ_{RIN}^2 is expressed as:

$$\sigma_{RIN}^2 = \frac{S_{RIN}^{LLO}(0)}{2t_d}. \tag{1.34}$$

The final clock instability induced by the optical detection noise, in short-term range, can be expressed by [34, 73]:

$$\sigma_y^{det}(\tau) = \frac{1}{\pi C Q_a}\left(\sum_{n=1}^{\infty}(\mathrm{sinc}(n\pi f_C t_d))^2 S_{RIN}^{det}(n f_C)\right)^{1/2}\sqrt{\frac{T_C}{t_d}}\,\tau^{-1/2}. \quad (1.35)$$

This noise contribution is proportional to the inverse of the contrast C of the atomic resonance line. It means that a high contrast Ramsey central fringe (or a clock signal) results in improving the signal-to-noise ratio and at the same time reduces the weight of this noise [34]. In addition, our analytical calculations show that the clock instability induced by the detection noise significantly depends on the detection time t_d. In our system the contribution of the optical detection noise is measured at the level of $\sigma_y^{det} \approx 2.2\times10^{-13}\,\tau^{-1/2}$ when the duration of the detection pulse is $t_d = 0.7$ ms. The measurement and analysis for this result is presented in section 3.7.

1.7.2.2 Phase Noise of the Microwave Interrogating

In atomic frequency standards operating in a pulsed mode like Ramsey-DR scheme, the frequency noise of the interrogation oscillator degrades the frequency stability. This phenomenon is known as the Dick effect [71]. The Dick effect causes some additional noise limit by transferring phase noise of the interrogating signal to atomic signal. For $\pi/2$ microwave pulses this noise is expressed as [34]:

$$\sigma_y^{LO}(\tau) = \left(\sum_{k=1}^{\infty}\mathrm{sinc}^2(k\pi\frac{T_R}{T_C})S_y^{LO}(k f_C)\right)^{1/2}\tau^{-1/2}, \quad (1.36)$$

where $f_C = 1/T_C$ is the cycle frequency in Ramsey-DR scheme and $S_y^{LO}(f)$ is the power spectral density of the microwave fractional frequency fluctuations which is given by:

$$S_y^{LO}(f) = \left(\frac{f}{\nu_0}\right)^2 S_\phi(f). \quad (1.37)$$

In the above equation, f is the Fourier frequency, ν_0 is the carrier frequency of our local oscillator (see section 2.5) which is 6.835 GHz and $S_\phi(f)$ is the power spectral density of the phase noise. Figure 1.13 shows the phase noise of our local oscillator which was measured and presented in [41]. From equation (1.36) and the measured phase noise of the LO shown in figure 1.13, the Dick effect stability limit is estimated at the level of $\sigma_y^{LO} \approx 7.5\times10^{-14}\tau^{-1/2}$ for our Rb clock operating in the Ramsey-DR scheme with typical Ramsey time of $T_R = 3$ ms and a cycle frequency of $f_C \approx 200$ Hz.

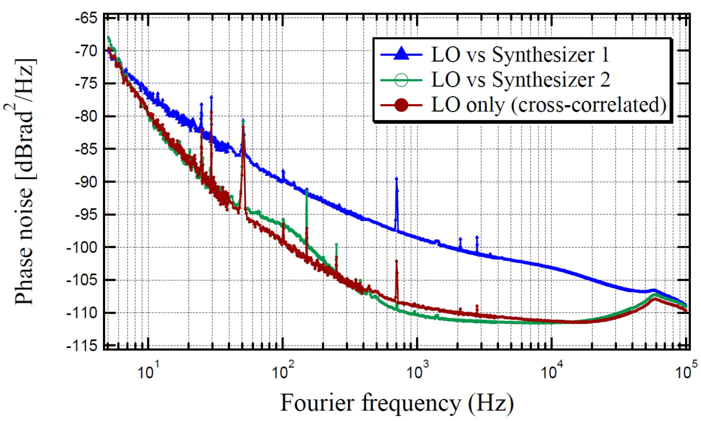

Figure 1.13: Cross-correlated phase noise measurement at 6.8 GHz carrier frequency. Brown color represent the phase noise of the LO only. The figure is taken from [41].

1.7.2.3 Light Shift Noise

Fluctuations in both intensity and frequency of the laser affect the clock frequency stability via the LS effects (see section 1.7.3.6). The total LS instability can be expressed by:

$$\Big(\sigma_{LS}(\tau)\Big)^2 = \Big(\sigma_\alpha(\tau)\Big)^2 + \Big(\sigma_\beta(\tau)\Big)^2, \tag{1.38}$$

where, $\sigma_\alpha(\tau)$ and $\sigma_\beta(\tau)$ are the induced instabilities associated with the laser intensity and the laser frequency noises, respectively, which are assumed to be uncorrelated. $\sigma_\alpha(\tau)$ and $\sigma_\beta(\tau)$ are given as:

$$\sigma_\alpha(\tau) = \frac{|\alpha|\,\sigma_{\Delta I_L/I_L} I_L}{\nu_{Rb}}\tau^{-1/2}, \tag{1.39a}$$

$$\sigma_\beta(\tau) = \frac{|\beta|\,\sigma_{\Delta\nu_L/\nu_L}\nu_L}{\nu_{Rb}}\tau^{-1/2}. \tag{1.39b}$$

In the above equation, $|\alpha|$ is the absolute value of the intensity LS coefficient, I_L is the laser intensity, $\sigma_{\Delta I_L/I_L}$ is the relative intensity stability of the laser, $|\beta|$ is the absolute value of the frequency LS coefficient, ν_L is the frequency of laser for the D2-transition (384.23 THz) and $\sigma_{\Delta\nu_L/\nu_L}$ is the relative frequency stability of the laser.

1.7.3 Medium- to Long-Term Frequency Stability

In an atomic clock, the clock frequency is influenced by fluctuations of physical quantities such as magnetic field, amplitude and intensity of the microwave field, and the frequency of the laser during the optical pumping/detection, the residual light during the Ramsey time and also environmental parameters like temperature, atmospheric pressure and humidity. All these effects shift the output clock frequency with respect to the unperturbed atomic reference transition. Since the vapor cell atomic clocks are among the secondary frequency standards, only the sensitivity of a given shift to the experimental parameter variation is evaluated (i.e. stability), but not the absolute shift (i.e. accuracy). In the other words, in the vapor cell atomic clock we are interested in investigating the impact of the fluctuations on the medium- to long-term frequency stability. The output clock frequency, ν_{clock}, can be given by:

$$\nu_{clock} = \nu_{Rb} + \Delta\nu_{Zeeman} + \Delta\nu_{BG} + \Delta\nu_{SE} + \Delta\nu_{LS} + \Delta\nu_{CP}, \tag{1.40}$$

where ν_{Rb} is the unperturbed frequency of the clock transition in ^{87}Rb used in the vapor cell, $\Delta\nu_{Zeeman}$ is the second order Zeeman shift, $\Delta\nu_{BG}$ is the shift due to ^{87}Rb-buffer gas collisions, $\Delta\nu_{SE}$ is the spin-exchange shift due to ^{87}Rb-^{87}Rb collisions, $\Delta\nu_{LS}$ is the light-shift and $\Delta\nu_{CP}$ is the shift due to cavity-pulling. In the following we present each of these frequency shifts in our Rb atomic clock.

1.7.3.1 Second-Order Zeeman Shift

The static magnetic field (C-field) applied to lift the degeneracy of the ^{87}Rb hyperfine ground states into their respective Zeeman levels also results in a small shift of the clock transition frequency. This phenomenon is called the second-order Zeeman shift; the C-field fluctuation perturbs the output clock frequency. This effect was discussed in section 1.2.1 and presented in the third term of equation (1.6). Considering the clock transition, $m_{F_1} = m_{F_2} = 0$, in this equation the clock frequency shift corresponding to the second order Zeeman effect is given by:

$$\Delta\nu_{Zeeman} = \frac{(g_J\mu_B)^2}{2hE_{HFS}} B_0^2 = A_0 B_0^2, \tag{1.41}$$

where B_0 is the C-field amplitude which in our experiments is typically at the level of about 100 mG, and A_0 is calculated to be 575.14 Hz/G^2. The first-order C-field sensitivity coefficient is calculated by partial derivation of equation (1.41) with respect to B_0:

$$\delta_{B_0}^{\nu_{Zeeman}} = \frac{\partial\Delta\nu_{Zeeman}}{\partial B_0} = 2A_0B_0. \tag{1.42}$$

The second-order Zeeman shift and its coefficient are calculated with the above formula and they are summarized in table 1.4. The instability induced by the second-order Zeeman shift of about $1.7\times10^{-14}/\%$ is estimated for our Rb clock.

Table 1.4: Second order Zeeman shift and its coefficient when the static magnetic field is 100mG.

Quadratic Shift	Magnetic coefficient	
$\Delta\nu_{Zeeman}$ (Hz)	$\delta_{B_0}^{\nu_{Zeeman}}$ (Hz/mG)	$\delta_{B_0}^{\nu_{Zeeman}}$ (/%)
5.75	1.15×10^{-1}	1.7×10^{-14}

1.7.3.2 Buffer-Gas Shift

The buffer gases are used to prevent collisions between the alkali atoms and the walls of the glass cell. Nevertheless, the collisions between Rb atoms and buffer gases include a shift at the clock resonance frequency. In the case of alkali atom collisions with the buffer gases, their hyperfine splitting is modified by changing the electron density [65]. This is a result of two forces: attractive long-range Van der Waals interactions and repulsive short-range Pauli exclusion forces. Van der Waals interactions decrease the electronic density at the nucleus, and therefore reduce the hyperfine splitting. Pauli exclusion forces act in the opposite direction, and they increase the electronic density at the nucleus and enhance the splitting [76]. This shift can be expressed empirically by [9]:

$$\Delta\nu_{BG} = P_0\Big(\beta + \delta(T-T_0) + \gamma(T-T_0)^2\Big), \tag{1.43}$$

where P_0 is the total gas pressure at the sealing temperature, and T is the cell temperature. $T_0 = 60°\mathrm{C}$ is the reference temperature for which the coefficients are measured. β, δ and γ are the pressure coefficient, the linear temperature shift coefficient, and the quadratic temperature shift coefficient of the buffer gas, respectively. Typical coefficient values for buffer gases N_2 and Ar are given in table 1.5. The buffer gas temperature coefficient, TC_{BG} is calculated from equation (1.43) by:

$$TC_{BG}(T) = \frac{\partial\Delta\nu_{BG}}{\partial T} = P_0(\delta + 2\gamma(T-T_0)). \tag{1.44}$$

$TC_{BG}(T)$ is minimum at a temperature of:

$$T_{inv} = T_0 - \frac{\delta}{2\gamma}, \tag{1.45}$$

where T_{inv} is the inversion temperature. If only a single buffer gas of either Ar or N_2 is used in the ^{87}Rb vapor cell, the inversion temperature can be obtained by using coefficients in table 1.5 either around $-200°$C or around $+300°$C, respectively. Therefore, a mixture of Ar and N_2 is chosen to make the temperature coefficient of the clock frequency negligible at a certain inversion temperature T_{inv}. In our system, a mixture of two buffer gases of Ar or N_2 with the vapor pressure ratio $r = P_{Ar}/P_{N_2} = 1.6$ is used. Then β, δ and γ coefficients are given by:

$$\beta = \frac{\beta_{N_2} + r\beta_{Ar}}{1+r}, \tag{1.46a}$$

$$\delta = \frac{\delta_{N_2} + r\delta_{Ar}}{1+r}, \tag{1.46b}$$

$$\gamma = \frac{\gamma_{N_2} + r\gamma_{Ar}}{1+r}. \tag{1.46c}$$

According to the coefficients presented in table 1.5, a pressure ratio of $r = 1.6$ and a total pressure of $P = 25$ Torr the corresponding calculated β, δ and γ coefficients are listed in table 1.5. We estimate the $T_{inv} \approx 69°$C by using the coefficients in table 1.5 and equation (1.45). Finally, from equation (1.43) $\Delta\nu_{BG}$ is estimated to be about 4.3 kHz. We also estimate the buffer-gas temperature coefficient $TC_{BG} \approx 0.01$ Hz/°C by using equation (1.44) at $T = T_{inv}$. The inversion temperature and the buffer-gas temperature coefficient are measured experimentally and presented in section 3.4.

Table 1.5: Calculated pressure shift and temperature coefficients for buffer gases Ar and N_2 at $T_0 = 60°$C [9] and for a mixture of Ar+N_2 with pressure ratio of $r = P_{Ar}/P_{N_2} = 1.6$.

Buffer gases	β (Hz Torr^{-1})	δ (Hz Torr^{-1} K^{-1})	γ (Hz Torr^{-1} K^{-2})
Ar	-59.7	-0.32	-0.35×10^{-3}
N_2	546.9	0.55	-1.5×10^{-3}
Ar+N_2	173.6	1.46×10^{-2}	-0.8×10^{-3}

1.7.3.3 Spin-Exchange Shift

In section 1.6.3, we discussed the spin exchange collisions between Rb atoms and their effect on broadening of the resonance line. These collisions also create phase shift of the atomic magnetic moment and results in an average frequency shift at the atomic transition [66, 77, 78]. The corresponding frequency shift of the clock operating in the Ramsey-DR scheme is expressed by [66]:

$$\Delta\nu_{SE} = -\frac{1}{8\pi} n\bar{v}_r \lambda_{SE} \langle\Delta\rangle_{T_R}, \tag{1.47}$$

where $n = 2.86 \times 10^{17}$m^{-3} is the atomic density of the Rb atoms in the vapor cell which mainly relates to the temperature of the stem. $\bar{v}_r \approx 400$ m/s is the average relative velocity of the colliding ^{87}Rb atoms, and $\lambda_{SE} = 6.9\times10^{-15}$ cm^2 is the spin-exchange cross section responsible for the frequency shift [77]. The spin-exchange shift, $\Delta\nu_{SE}$, is temperature dependent as the atomic density of the Rb atoms, n, and the average relative velocity of the Rb atoms are functions of the temperature. In equation (1.47),

$\langle\Delta\rangle_{T_R}$ is the average value of the population inversion during the Ramsey time T_R. $\langle\Delta\rangle_{T_R}$ was obtained approximately equal to 4×10^{-3} for a cell temperature of 60°C (in our Rb clock the cell temperature is set to 63.2°C (see section 3.4)) and reported in ref. [78]. Finally, the contribution of the spin-exchange effect in the clock frequency shift is obtained $\Delta\nu_{SE} = -0.01\,\text{Hz}$ or $\frac{\Delta\nu_{SE}}{\nu_{Rb}} \approx -1.5\times10^{-12}$. In our Rb clock, at the stem operating temperature around 332 K, for a variation of the temperature of one degree we have $\Delta n/n \approx 10\%$. Therefore from equation (1.47), we can evaluate a temperature sensitivity caused by spin exchange of $\approx 1.6\times10^{-13}/\text{K}$. This result is about one order of magnitude lower than the one presented by Bandi et al. [35, 41] and is at same level presented by Micalizio et al. [78].

1.7.3.4 Cavity-Pulling

In an Rb atomic clock which contains a microwave cavity, the cavity-pulling effect is a phenomenon that may create a shift in the clock frequency. This effect is due to the feedback of residual field in the microwave cavity on the atomic sample in the Ramsey-DR scheme and also to the detuning of the cavity from ν_{Rb} [42]. The frequency shift induced by cavity pulling for an atomic clock operating in the Ramsey-DR scheme can be obtained from [43]:

$$\Delta\nu_{CP} = -\frac{4}{\pi}\frac{Q_{cav}}{Q_a}\Delta\nu_c c(\theta) \tag{1.48}$$

where Q_{cav} and Q_a are the cavity quality factor and the resonance atomic quality factor, respectively and are given by equations (2.2) and (1.30). Q_{cav} is about 150 for our cavity (see section 2.3.2) and Q_a is at the level of 4.1×10^7. $\Delta\nu_c$ is the cavity detuning from ν_{Rb} and for our cavity is $\nu_{cav} - \nu_{Rb} \approx 1.3\,\text{MHz}$ (see section 2.3.2.1). In the above equation $c(\theta)$ is given by [43]:

$$c(\theta) = \frac{-1}{\gamma_2 T_R}\log\left(\cosh\left(\frac{k}{\gamma_2}(1-e^{\gamma_2 T_R})\right) + \cos\theta\sinh\left(\frac{k}{\gamma_2}(1-e^{\gamma_2 T_R})\right)\right), \tag{1.49}$$

where θ is the microwave pulse area ($\theta = b\tau_m$, b is the microwave Rabi frequency and τ_m is the duration of the microwave pulse) and k is the number of microwave photons emitted by an atom in 1 s and is defined by [42]:

$$k = \frac{\mu_0\mu_B^2\eta n Q_{cav}}{\hbar(2I+1)}, \tag{1.50}$$

where μ_0 is the vacuum permeability, and μ_B is the Bohr magneton. η is the cavity filling factor [79] and in our cavity is measured to be 0.136 [41]. I is the nuclear spin which in ^{87}Rb is 3/2 and n is the atomic density of Rb atoms in the vapor cell which in our case is $2.86\times10^{17}\,\text{m}^{-3}$. Applying all these values and constants in equation (1.50) gives $k = 1.49\,\text{s}^{-1}$. In the case of applying exact $\pi/2$ microwave pulses, the second term in equation (1.49) becomes zero. In our measurements when $T_R = 3\,\text{ms}$ and $\gamma_2 = 220\,\text{s}^{-1}$ (see section 1.6), $\Delta\nu_{CP} = 2.14\times10^{-5}\,\text{Hz}$ in equation (1.48). The cavity temperature coefficient is measured $\frac{\Delta\nu_{cav}}{\Delta T_{cav}} = -40\,\text{kHz/K}$ (see section 2.3.2.2). Hence for our Ramsey-DR Rb clock, we can estimate the temperature sensitivity of the cavity pulling $\frac{\Delta(\Delta\nu_{CP})}{\Delta T_{cav}} \approx 6.58\times10^{-7}\,\text{Hz/K}$ equivalent to a relative value of $\frac{\Delta(\Delta\nu_{CP})/\nu_{Rb}}{\Delta T_{cav}} \approx 9.63\times10^{-17}\,/\text{K}$ from equation (1.48). This result is more than two orders of magnitude lower than for the Rb clock presented by Micalizio et al. [34]. This difference can be explained by the quality factors and the temperature sensitivities of the cavities used in the clocks.

1.7.3.5 Microwave Power Shift (PS)

The microwave power sensitivity of the clock transition frequency is reported for Rb vapor cells with buffer gases in [9, 80, 81, 82]. This sensitivity is most likely a consequence of the microwave field inhomogeneity inside the vapor cell and it is known as microwave power shift $\Delta\nu_{\mu w}$. In an Rb clock operating in the Ramsey-DR scheme, the measured clock frequency is also a function of the microwave power (or microwave pulse area). During the microwave interrogation (Rabi pulses), due to the microwave field inhomogeneity inside the vapor cell, different parts of the atomic sample in the cell experience different microwave powers (or microwave pulse area) and consequently have different frequencies contribute to the resonance signal. This phenomenon results in frequency shift of the measured resonance line which is known as position-shift as it depends on the atom's position inside the cell [83, 78]. The microwave power shift sensitivity influences the cavity pulling which is seen from $c(\theta)$ in equation (1.48). Therefore, from equation (1.48) it is possible to deduce the sensitivity of the clock frequency to the amplitude of the microwave pulse, with the assumption of working at $\theta = \theta_0$ [78]:

$$\left.\frac{\partial \Delta\nu_{CP}}{\partial \Delta\theta}\right|_{\theta=\theta_0} = -\frac{8}{\pi}\frac{Q_{cav}}{Q_a}\Delta\nu_c \sinh\left(\frac{k}{2\gamma_2}(1-e^{\gamma_2 T_R})\right), \tag{1.51}$$

For our Ramsey-DR Rb clock with a microwave cavity with a low quality factor, we estimate the sensitivity from equation (1.51) and using values given in section 1.7.3.4 to be:

$$\frac{\Delta(\Delta\nu_{CP})/\nu_{Rb}}{\Delta\theta/\theta} \approx 4.5\times 10^{-14}/\%. \tag{1.52}$$

This result is at the same level for the one presented by Micalizio [78]. We present preliminary results from the microwave power shift in our Ramsey-DR Rb clock in section 3.6.

1.7.3.6 Light-Shift (LS)

Light shift or AC Stark shift is a well-known phenomenon in light-matter interactions. Light shift is one of the instability sources in the atomic frequency standards [84]. It appears when the laser frequency is detuned from the central frequency of the optical transition [85]. The LS effect is due to a virtual absorption and re-emission of the off-resonance incident photon. These virtual transitions produce a coupling between the wave functions of the levels involved in the process which results in an energy shift of the level [50]. In 1968, Mathur presented the LS theory in relation to alkali atoms and demonstrated that the LS is proportional to the intensity and frequency of the applied light [86].

Light shift for a specific transition coupled by a light field with the frequency of ν_L for the ground state level can be expressed as [84]:

$$\Delta_{LS} = \frac{1}{4}|\Omega_R|^2 \frac{\nu_L - \nu_{opt}}{(\nu_L-\nu_{opt})^2 + (\Gamma^*/2)^2}, \tag{1.53}$$

where, Ω_R is the optical Rabi frequency of the light field, ν_{opt} is the transition frequency where the light field is resonant, and Γ^* is the intrinsic decay rate of the excited states. In our Rb clock, we use the laser for optical pumping and optical detection that emits at the D2 line of ^{87}Rb (see figure 1.3) which is achieved by the laser field coupling one of the ground state components in $5\,^2S_{1/2}$ to the excited state $5\,^2P_{3/2}$. This model allows a qualitative understanding of the LS effect. However, it stands for an average shift induced to the degenerated hyperfine ground states and not specifically to the clock states, while in the ^{87}Rb atomic clocks, the clock levels are coupled to several partially resolved excited states; therefore, the contribution of each has to be considered [87]. In this thesis, we use the model presented by M. Pellaton [87], in which only the allowed transitions from the clock levels to the excited states' Zeemans sublevels are considered. In addition, in this model the impact of buffer gases on both shift and a broadening of the optical transitions are included where both are proportional to the pressure. We use the following expression for the LS [87]:

$$\Delta_{LS} = \left(\frac{\Omega_R}{4\pi}\right)^2 \sum_{F_e} \int d\nu_D g(\nu_D) \left(\frac{\delta\nu_L'}{(\frac{BG_{\Gamma^*}}{4\pi})^2 + (\delta\nu_L')^2} - \frac{\delta\nu_L}{(\frac{BG_{\Gamma^*}}{4\pi})^2 + (\delta\nu_L)^2} \right), \tag{1.54}$$

where $g(\nu_D)$ is the Gaussian distribution of the frequencies, and BG_{Γ^*} is the total broadening of the excited state (the intrinsic decay plus the impact from buffer gases). In an atomic clock, the LS can be expressed locally, that is, for a given laser frequency and laser intensity by two coefficients known as intensity light shift α_{LS} and frequency light shift β_{LS} coefficients. The intensity light shift coefficient α_{LS} is calculated from equation (1.53) at a fixed laser frequency as:

$$\alpha_{LS} = \left.\frac{\partial \Delta\nu_{LS}}{\partial I_L}\right|_{\nu_L:\text{const.}} . \tag{1.55}$$

In the same way, the frequency light shift coefficient β_{LS} is given when the laser intensity is fixed:

$$\beta_{LS} = \left.\frac{\partial \Delta\nu_{LS}}{\partial \nu_L}\right|_{I_L:\text{const.}} . \tag{1.56}$$

In an atomic clock operating in the Ramsey-DR scheme, due to the separation of the light and microwave pulses, a reduction of the LS effect is expected. However, in practice in the Ramsey-DR scheme, LS may have two origins: 1) a residual light during the time that the laser is switched off (from the beginning of the first $\pi/2$ pulse until the end of the second $\pi/2$ pulse) due to non-perfect background light suppression (see section 2.2) and 2) incomplete optical pumping which results in the residual hyperfine coherence. The first origin can be explained by the AC Stark shift effect due to the coupling between light and induced atom's dipole [88] and the second origin can be explained by the residual coherence during the optical pumping pulse [42]. In this work we concentrate on the first one and more details about LS are presented in section 3.5.

1.8 Summary of Frequency Shift Coefficients

Table 1.6 shows the summary of the shift sensitivities to relevant parameters influence on the clock frequency. The values for the sensitivity coefficients are typical for an Rb buffer gas cell in the experimental conditions encountered in chapter 3. In this table, light shift and microwave power shift are measured quantities in chapter 3.

Table 1.6: Summary of the perturbing frequency shifts for our Ramsey-DR Rb clock. Light shift and microwave power shift are measured quantities (see Chapter 3).

Physical effect	Sensitive variable	Coeff.	Absolute coeff.	Relative coeff.	Frequency shift (approx.)
Zeeman	Magnetic field		$115\,\mathrm{Hz/G}$	$+1.7\times10^{-8}\,/\mathrm{G}$	$6\,\mathrm{Hz}$
Buffer gas	Temperature	TC_{BG}	$0.01\,\mathrm{Hz/K}$	$1.32\times10^{-12}\,/\mathrm{K}$	$4250\,\mathrm{Hz}$
Spin exchange		TC_{SE}	$1.1\,\mathrm{mHz/K}$	$1.6\times10^{-13}\,/\mathrm{K}$	$< 0.1\,\mathrm{Hz}$
Cavity pulling		TC_{CP}	$0.6\,\mu\mathrm{Hz/K}$	$9.6\times10^{-17}/\mathrm{K}$	$< 1\,\mathrm{mHz}$
Light shift	Intensity	α_{LS}	$0.144\,\mathrm{mHz}/\%$	$2\times10^{-14}\,/\%$	$< 0.01\,\mathrm{Hz}$
	Frequency	β_{LS}	$-38\,\mathrm{mHz/MHz}$	$-5.5\times10^{-14}\,/\mathrm{MHz}$	$< 1\,\mathrm{mHz}$
Cavity pulling	μW pulse area		$0.3\,\mathrm{mHz}/\%$	$4.5\times10^{-14}\,/\%$	$< 1\,\mathrm{mHz}$
Microwave	μW power		$-0.02\,\mathrm{Hz}/\mu\mathrm{W}$	$-2.6\times10^{-13}\,/\%$	$< 0.1\,\mathrm{Hz}$
				Total Frequency shift (approx.)	$\approx 4256\,\mathrm{Hz}$

1.9 Conclusion

In this chapter, the DR technique with an electric dipole transition and a magnetic dipole transition for ^{87}Rb atomic clock was briefly presented. The Ramsey-DR scheme based on optical-microwave DR technique was presented and described visually with Bloch spheres. We calculated both intrinsic population and coherence relaxation times (T_1 and T_2, respectively) particularly for the clock transition of ^{87}Rb atoms in our particular vapor cell (see section 2.3.1) with buffer gases to be about 4.5 ms. The experimental results are presented in chapter 4. The basics of the clock frequency stability analysis were explained while discussing the importance of Allan deviation. The short-term frequency stability in our Rb atomic clock was predicted at the level of approximately $3\times10^{-13}\tau^{-1/2}$ by considering the phase noise of the microwave interrogation through the Dick effect, the LS, and the instability associated to the total optical detection noise. In our study, a new analytical formula was developed to predict the clock's short-term stability by considering the duration of the optical detection phase of the Ramsey-DR scheme. The verification of the this formula is presented in section 3.7.

2 Experimental Setup

This chapter describes the experimental setup used in this work. Our experimental setup is an Rb atomic clock which is developed in this thesis. This setup consists: 1) a laser system which is designed and build in the LTF, 2) a physics package that contains a newly developed Rb vapor cell and a magnetron-type microwave cavity which is designed, developed and built in collaboration with Laboratory of ElectroMagnetics and Acoustics (LEMA) at Ecole Polytechnique Fédérale de Lausanne (EPFL) in the context of an SNSF project[1] and 3) a microwave source local oscillator (LO) which is designed, developed and built in Istituto Nazionale di Ricerca Metrologica (INRIM). We present the detailed characterizations and evaluations of the required components of the Rb clock, such as the laser system, physics package –which contains the microwave cavity, the vapor cell and the C-field coils– and the microwave source (the local oscillator (LO)), in view of the DR spectroscopy and clock operation.

2.1 Rb Clock Setup

The schematic and photograph of this Rb atomic clock setup are shown in figures 2.1 and 2.2. It consists of three main functional blocks: 1) a laser system, 2) a physics package and 3) a microwave source LO. The laser system is a compact frequency-stabilized laser which is used as an optical source [89]. The laser system presented here was realized as a result of the efforts of P. Scherler and F. Gruet both from the LTF who designed, constructed and characterized it, and M. Pellaton who produced the evacuated reference Rb cell. The physics package contains a cylindrical Rb vapor cell which is placed in a magnetron-type microwave cavity [36]. The Rb vapor cell is designed and developed at LTF, and fabricated by M. Pellaton. The magnetron-type microwave cavity is designed and built at the LTF in collaboration with LEMA–EPFL. The Rb vapor cell is filled with isotopically enriched ^{87}Rb and a mixture of Ar and N_2 as buffer gases. The microwave cavity with a volume of only 45 cm^3 and with a low quality-factor (≈ 200) resonates at the ^{87}Rb clock transition frequency of ≈ 6.835 GHz. It is surrounded with a magnetic coil (C-field coil) that generates a static magnetic field oriented parallel to the cell's symmetry axis and the laser propagation vector ($\vec{Z}$ direction). In order to support an atomic clock operating in a pulsed scheme, the implemented electronic package was designed and developed at INRIM- in Italy [90]. It includes the LO that generates a ≈ 6.835 GHz radiation resonant with the ^{87}Rb clock transition, the servo, and the oven-controlled crystal oscillator (OCXO) quartz oscillator. The characteristics of each component will be presented next.

In the following, a detailed description and characterization is given for each functional block of our Rb clock. We discuss the choices of experimental parameters and how they can affect the clock

[1] Within the projects FNS:"Microwave Cavities for High Performance Double Resonance Atomic Clocks and Sensors" no. 140712 (2012-2015) and "Study of microwave cavities for high performance pulse pumped double resonance atomic clocks" no. 162346 (2015-2018).

performances. Finally, we conclude that this Rb clock is capable of being operated in a Ramsey-DR scheme and can achieve a stability comparable to state-of-the-art results. In the next chapter, we will discuss the main results of our Rb clock obtained in the Ramsey-DR scheme.

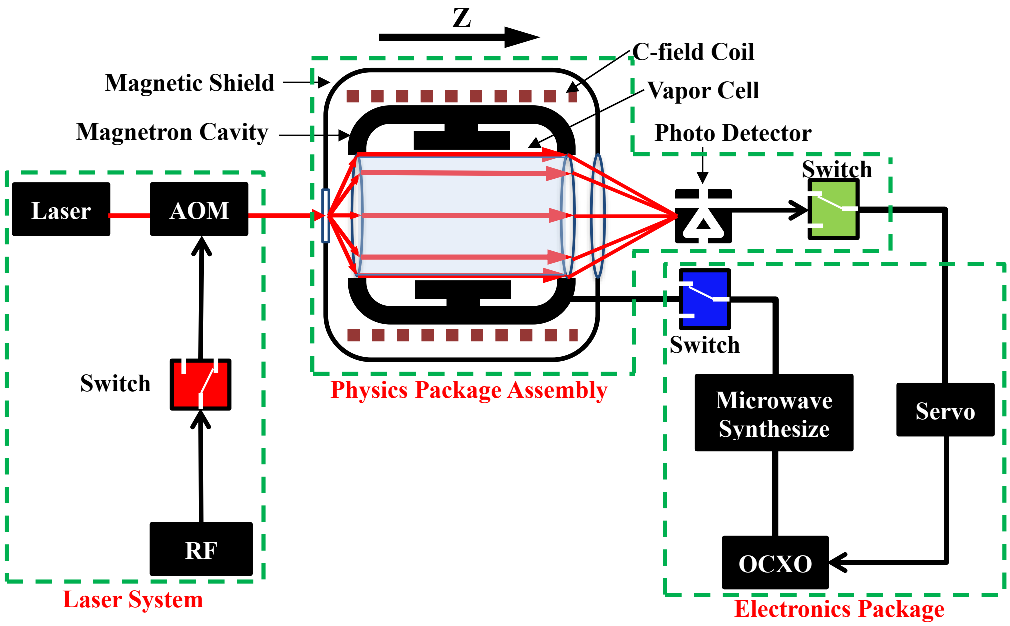

Figure 2.1: Schematic of the clock experimental setup with three functional blocks; 1) a laser system, 2) a physics package and 3) an electronic package.

2.2 Laser System

The frequency stabilized laser system is designed and built at the LTF. A photograph and the schematics of the LH are shown in figure 2.3. The optical part of the LH occupies only 1 liter while its overall volume is 2.4 liters, including room for control electronics. A Distributed Feedback (DFB) diode laser with an integrated Peltier element and a collimating lens is used as an optical source. The laser emits at 780 nm that corresponds to the D2 transition of ^{87}Rb atoms. An optical isolator (OI) is used to avoid any light feed-back in to the diode. The frequency of the laser is stabilized to the sub-Doppler absorption lines using an evacuated ^{87}Rb reference cell by the method of saturated-absorption spectroscopy [91]. The reference cell is surrounded by two magnetic shields in order to protect the atoms from any external magnetic field fluctuations. In the LH, an Acousto Optical Modulator (AOM) is integrated that allows shifting the light's frequency. In addition, the AOM is used as a fast switch to control the duration and intensity of the laser during the optical pumping and the optical detection pulses in the experiments discussed in this thesis. The RF synthesizer from Agilent E8257D is used as an RF source to drive the AOM.

The following discussion reports the detailed test results and characteristics of the laser system which were mainly performed by F. Gruet from the LTF.

2.2.1 Laser System Properties

Laser diode properties such as power, frequency tuning and absorption spectrum were measured and characterized by F. Gruet and subsequently reported here. For the laser diode of the LH, power

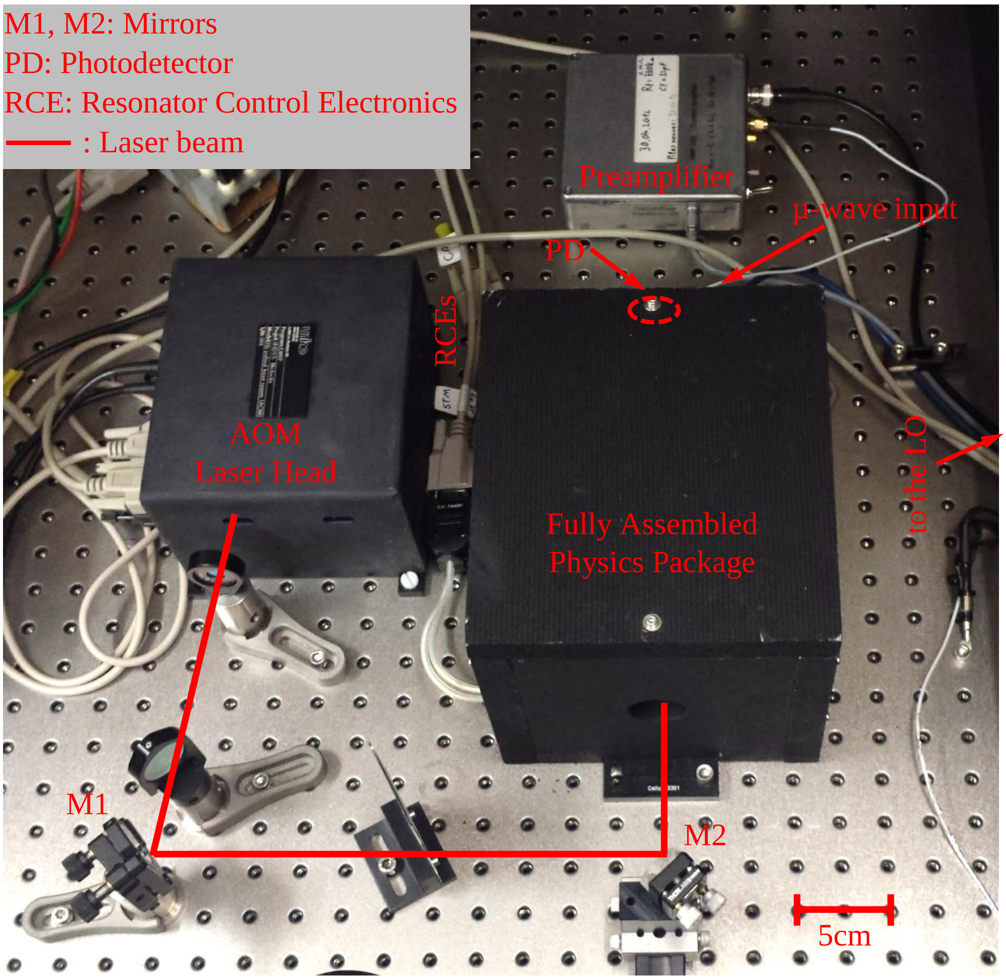

Figure 2.2: Photograph of the Rb atomic clock used in this thesis.

versus current and temperature tuning coefficients are 0.8 W/A and −0.9 mW/K, respectively. Wavelength versus current and temperature tuning coefficients are 2 pm/mA (−1 GHz/mA) and 55 pm/K (−30 GHz/K), respectively. The wavelength of 780 nm is reached at a laser temperature of about 37°C and a current of 95 mA. The laser system output power was measured at 15 mW at 100 mA. The ON/OFF ratio was measured at 40 dB ($ON = 12$ mW, $OFF = 1\,\mu$W). However, this measurement was quite sensitive to the background light in the laboratory, and the measured ON/OFF ratio might be limited by this effect. Figure 2.4 shows the recorded saturated absorption spectrum (see section 2.2.4) of the Rb reference cell (blue trace) with another absorption spectrum obtained with the output beam of the laser system (using another, external Rb cell, red trace). In this case, the output beam of the laser system is shifted by −160 MHz using the AOM double-pass technique.

The AOM rise/fall time was measured about 4.5 μs from figure 2.5. It corresponds to the time interval measured between 10% and 90% of the maximum light signal. The rise/fall time specification of the RF switch used is typically 5 ns and the switching time is typically 10 ns. Therefore, the measured rise/fall times are not limited by the switch.

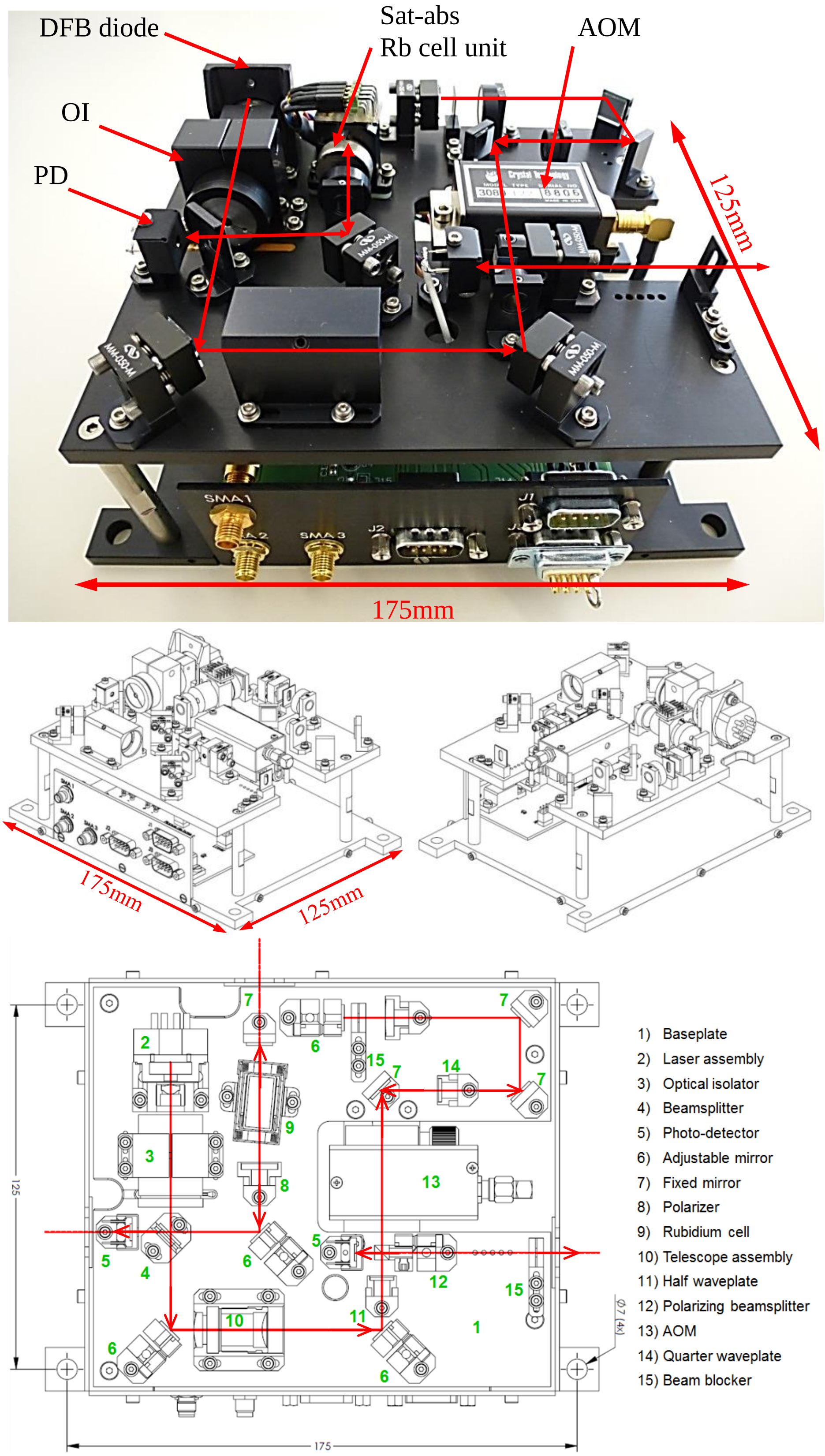

Figure 2.3: Photograph and CAD design of the laser head (OI: optical isolator, PD: photo detector, M: mirror, L: lens, BS: beam splitter, PBS: polarization beam splitter, $\lambda/4$: quarter-wave plate, $\lambda/2$: half-wave plate)

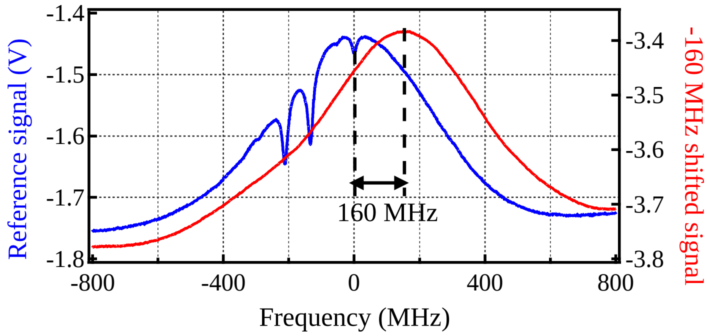

Figure 2.4: Saturated absorption reference spectrum (blue) of the laser system and Doppler broadened absorption spectrum (red) obtained with the output beam of the laser system on the $F_g = 2$ ground-state hyperfine level. The frequency shift is -160 MHz due to the AOM. The figure was made by F. Gruet.

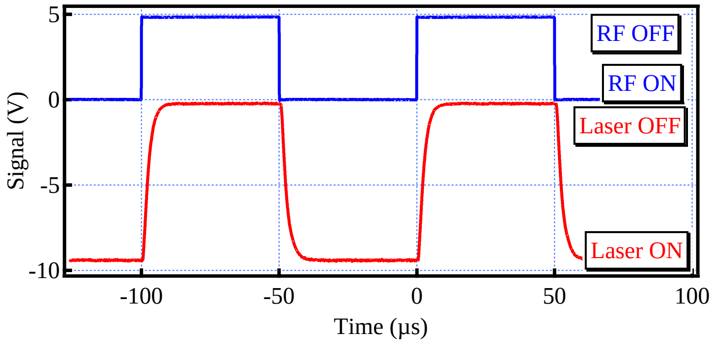

Figure 2.5: AOM rise/fall time was measured about 4.5 μs. The figure was made by F. Gruet.

2.2.2 Frequency and Intensity Stability of the Laser Head (LH)

The frequency stability was measured by beat note between the laser system and a reference LH. Both lasers were locked on the same atomic transition (cross-over 21-23); the beat frequency then corresponds to the -160 MHz AOM shift of the laser system. Figure 2.6 shows the beat frequency stability measurement of about 90 hours. At 1 s, the relative stability is at the level of 1.5×10^{-11} and stays below 1×10^{-11} from 3 s to 10^5 s. A bump is present from 1 000 to 10 000 seconds might possibly arise from the temperature variations impacting on the AOM or the laser head control electronics

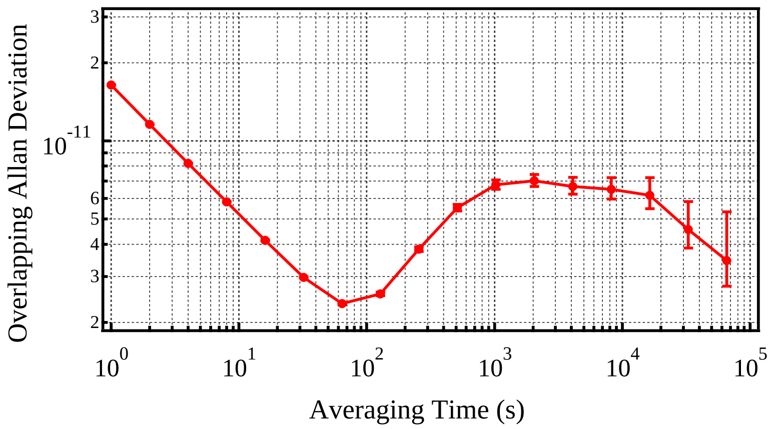

Figure 2.6: Frequency stability of the beat note between the laser system and the reference LH. The figure was made by F. Gruet.

During the frequency stability measurement, the optical power of the saturated absorption signal has been recorded and its relative stability is shown in figure 2.7. The result is given with drift (dashed line) and with drift removed (drift = 3.9×10^{-3}/day).

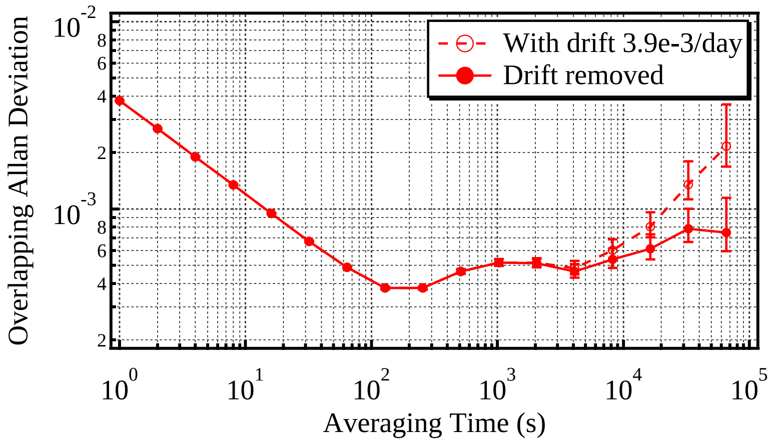

Figure 2.7: Relative power stability, measured on the saturated absorption signal detector. The figure was made by F. Gruet.

2.2.3 Relative Intensity Noise (RIN) and Frequency Modulation (FM) Noise

The relative intensity noise (RIN) of the laser system was measured before and after a double-pass through the AOM. Before the double-pass (the blue curve in figure 2.8), the RIN behavior is the same as the laser diode alone. However, after the double-pass through the AOM, the noise level is increased in the frequency band between 10 Hz and 5 kHz (the red curve in figure 2.8). The slight increase of noise after 20 kHz is due to the noise limit of the external detector used for the measurement.

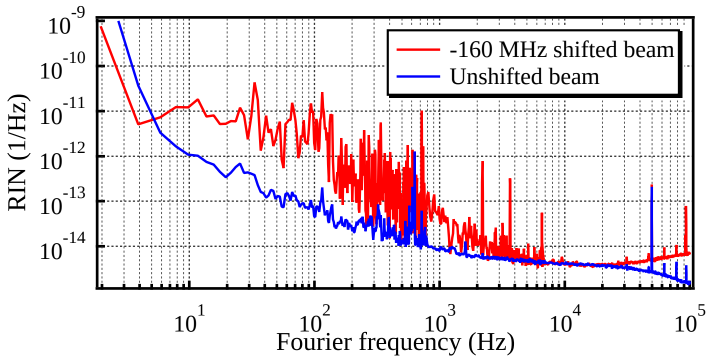

Figure 2.8: RIN measurements of the laser system before (blue) and after (red) the AOM. The figure was made by F. Gruet. The noise floor was approximately at the level of 3.7×10^{-15} (1/Hz).

Figure 2.9 shows the frequency modulation (FM) noise at the output of the laser system which is measured in the double-pass configuration, with -160 MHz total shift in free-running using FM-to-AM demodulation using the Rb atomic absorption line from an external Rb vapor cell and the detector.

2.2.4 Saturated Absorption

The method of saturated absorption spectroscopy [91] allows resolving the sub-Doppler peaks by overcoming the Doppler broadening effect. This method is based on the velocity-selective saturation of the Doppler-broadened transitions. There, two counter-propagating laser beams derived from a single

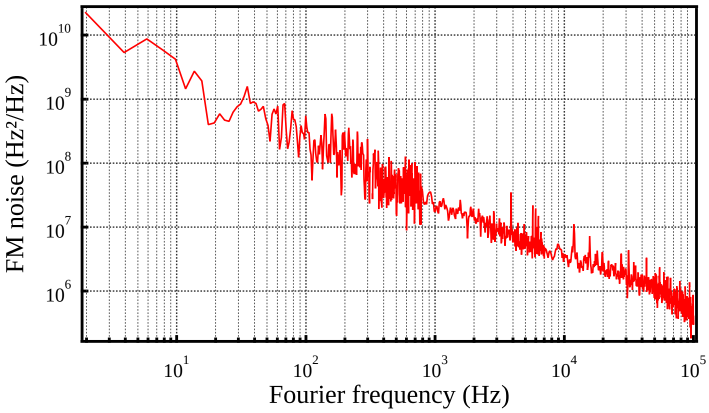

Figure 2.9: Frequency noise at the output of the laser system in double-pass configuration, with a shift of -160 MHz. The figure was made by F. Gruet.

laser source with the same frequency but different intensity are sent through the atomic vapor cell. The "pump" beam has a high intensity, while the "probe" beam with a weak intensity through the atomic vapor is recorded with a photodiode and gives the actual spectroscopic signal. If the pump beam is blocked, the probe beam is recorded and Doppler-broadened absorption spectrum is obtained. Once the pump beam is unblocked, the absorption spectra will be changed. When the laser beam frequency is off-resonance the atoms moving either in the same propagation direction or in the opposite direction with respect to the laser beam experience a red-shifted or blue-shifted frequency, respectively. On the other hand, when the laser beam frequency is on resonance, only atoms that move perpendicular to the laser beam experience no Doppler shift from either of the beams. In turn, these atoms are addressed via the pump and probe beams simultaneously. Assuming that the atoms have a two-level system, the pump beam depletes the ground state level and promotes atoms to the excited state. Therefore, the probe beam detects a reduced number of atoms in the ground state.

Real atoms have multiple upper and lower energy levels which add complexities to the simple two-level system. For the D2 line of ^{87}Rb, transitions between two lower levels and four upper levels can all be resolved with our laser. Because several upper or lower levels are close enough in energy, their Doppler-broadened profiles overlap. Then additional narrow absorption dips called "cross-over dips" appear. Since, these narrow width dips are sensitive to the broadening by the collisions, they are observable under the condition that the buffer gas pressure is low [92]. Figure 2.10 shows a typical saturated absorption spectrum of the Rb sub-Doppler peaks obtained from the reference cell in the LH. The polarization of the pump and probe beams also influences the sub-Doppler peaks due to population redistribution among the Zeeman sublevels. Therefore, the probe beam is either transmitted or absorbed based on the polarization used [93]. In this work, a linear polarization of the laser beam is used which is parallel for both pump and probe beams; therefore, we observe a sub-Doppler peak with increased absorption on the $F_g = 1$ component.

2.3 Physics Package

We have designed and built a new physics package at the LTF. CAD diagram of the physics package is shown in figure A.1. The physics package contains two main components: an Rb vapor cell and a microwave cavity. The Rb vapor cell is placed in the microwave cavity. A C-field coil which generates a static magnetic field surrounds the microwave cavity. In our physics package, three temperature

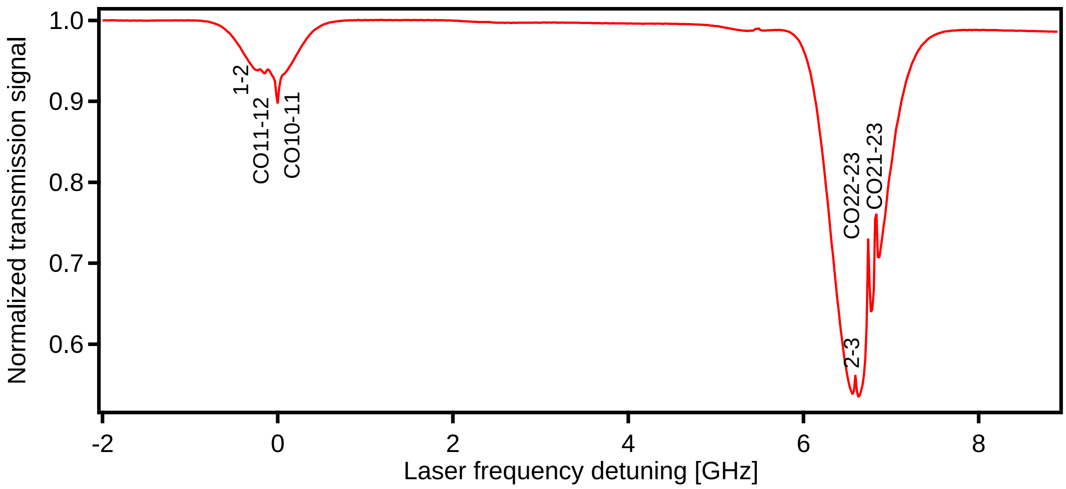

Figure 2.10: Saturated absorption spectra of ^{87}Rb obtained from the reference cell in the LH. The sub-Doppler lines are labeled and correspond to below transitions: 1-2: F_g=1→F_e=2, CO11-12: F_g=1→F_e=1,2 cross-over, CO10-11: F_g=1→F_e=0,1 cross-over,2-3: F_g=2→F_e=3, CO22-23: F_g=2→F_e=2,3 cross-over and CO21-23: F_g=2→F_e=1,3 cross-over.

controllers are implemented to control and record the temperatures of the cell-stem, the microwave cavity and the external shielding. Finally all these components are isolated with a magnetic shield to reduce any interaction with external fields. The following discussion presents, the main characteristics of the vapor cell and the microwave cavity.

2.3.1 Rb Vapor Cell

Generally, vapor cells are made of borosilicate or quartz glass. The vapor cells are often cylindrical or spherical in shape in order to facilitate fabrication and placing them into the cavity resonator. In principle, the two end windows of a cylindrical cell are flat to avoid any lensing effect with the light propagating along the length of the cell.

The vapor cell used in our Rb clock is designed and produced at the LTF and made from borosilicate. The ID number of this vapor cell was "3301". The photograph of the vapor cell is shown in figure 2.11. The vapor cell is filled with ^{87}Rb (99% isotopic purity) and buffer gases of Ar and N_2. The vapor cell has two distinctive regions: a cell-volume, which holds the Rb vapor, and the cell-stem that acts as a reservoir for Rb atoms. The cell-stem can avoid accumulation of the metallic Rb onto the cell walls. In addition, the vapor pressure inside the cell-volume and consequently the density of Rb atoms inside the cell-volume can be controlled by controlling the cell-stem temperature. In our vapor cell, the cell-volume has a cylindrical shape with an outside diameter of $\phi = 25$ mm and a length of $l = 25$ mm; the cell-stem has a length of 8.6 mm. This vapor cell with the external volume of around 12.3 cm^3 is considered a large cell. The internal volumes of the cell and the stem are $V_{cell} = 8553$ mm^3 and $V_{stem} = 5.1$ mm^3, respectively. At a constant buffer gas pressure, the larger dimensions of a cylindrical vapor cell result in a reduction in the cell-wall diffusion relaxation rates, γ_{1CW} and γ_{2CW} (according to equation (1.20)) that consequently can improve the short term stability of the vapor cell atomic clock. The vapor cell is filled with ^{87}Rb and buffer gases of Ar and N_2. Adding buffer gases leads to increasing the flight time of Rb atoms to reach to the cell wall and prevents the direct collision of the Rb atoms into the cell walls. In other words, they reduce the mean free path of Rb atoms from a few centimeters to a few micrometers in a vapor cell. Particularly N_2 buffer gas quenches the fluorescence of the excited

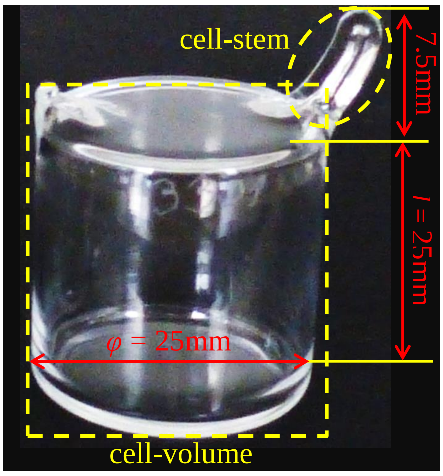

Figure 2.11: Photograph of the cylindrical buffer-gas Rb vapor cell with both diameter and length of 25 mm including a 7.5 mm cell-stem as an Rb reservoir. Cell-ID "3301".

Rb atoms that transfer from the excited state P to the ground state [9]. Using N_2 as a buffer gas causes a positive temperature coefficient frequency shift on the Rb clock transition, which is compensated by using Ar with a negative temperature coefficient frequency shift [9]. The total pressure of the mix buffer gases is chosen in a way to minimize the relaxation rate in the clock cell, which in our case was 33 mbar. The buffer gas vapor pressure ratio of r $= \frac{P_{Ar}}{P_{N_2}} = 1.6$ was selected in order to achieve the inversion temperature of around 65 °C.

Calosso et al. presented the "enhanced temperature sensitivity" (ETS) for vapor cells used in the POP clock is due to the large volume of the cell-stems that serve as cold points and reservoirs for the metallic Rb in these cells [94]. This effect describes how the temperature fluctuation in the cell-stem results in the redistribution of buffer gases in the entire cell due to the buffer-gas density variations between the cell-volume and the cell-stem, which is a result of a temperature gradient between them. Therefore, in our newly designed Rb vapor cell used in this work, a reduced ETS was achieved by strongly reducing the volume of the cell-stem down to $V_{stem} \approx 5\,\text{mm}^3$ which is about 10 times smaller than in the vapor cell used in previous study at the LTF by Bandi et al. [41, 35]. According to [94], in a vapor cell with a total volume of $V = V_{cell} + V_{stem}$, the stem TC, TC_{stem}, is proportional to the stem volume, V_{stem}, by:

$$\frac{\partial \nu_{clock}}{\partial T_{stem}} \approx n_s a'_0 \cdot \frac{v_s}{T_{stem}}, \tag{2.1}$$

where, T_{stem} is the stem operation temperature, $n_s = N/V$ is the average buffer gas density and $v_s = V_{stem}/V$. In the above formula a'_0 denotes the buffer-gas mixture in the cell volume and is related to β coefficient in equation (1.46) and is estimated approximately $a'_0 \approx 5.4 \times 10^{-15}$ Hz·cm^3 [94]. In our vapor cell, $v_s = 5.6 \times 10^{-4}$ and at the cell filling temperature of 293 K with a total buffer gas pressure of 30 mbar, we obtain $n_s \approx 7 \times 10^{17}$ cm^{-3}. Therefore for our Rb vapor cell, using the above values in equation (2.1), we estimate the relative stem TC at the level of $TC_{stem} \approx 9.8 \times 10^{-13}/\text{K}$ when the stem temperature is T_{stem} =60°C. This result is in good agreement with the measurement result shown in section 3.4. The estimated TC_{stem} for our Rb vapor cell is more than one order of magnitude lower than the one used in Bandi et al. ($\approx 1.1 \times 10^{-11}/\text{K}$ [35]) and is about two orders of magnitude lower than the one used in Calosso e .al. ($\approx 1.5 \times 10^{-10}/\text{K}$ [94]).

2.3.2 Microwave Cavity

Microwave resonator cavities are widely used in various applications such as frequency standards [9, 95], Electron Spin Resonance [96], Electron Paramagnetic Resonance [97] and Nuclear Magnetic Resonance (NMR) [98]. In all these applications, the field uniformity, the thermal and mechanical stability, and the robustness and reliability of the microwave cavity have to be considered in view of their performances. Typically, resonators are designed in various types such as split-ring [98], slotted-tube [99, 100], which is also known as a loop-gap-resonator.

We used a high-performance magnetron-type microwave cavity in this thesis. The photograph of this microwave cavity is shown in figure 2.12. CAD diagram of this microwave cavity is shown in figure A.2. This microwave cavity is designed and built at the LTF in collaboration with LEMA-EPFL, Lausanne, Switzerland and is based on the one presented in [36]. Numerical simulation results obtained via ANSYS HFSS for this cavity can be found in [101]. Our microwave cavity has a cylindrical shape with an external diameter of 36 mm and a length of 34.2 mm with a total volume of about 35 cm^3, which is considered a compact sized cavity. The open space inside the cavity is used to locate a 25 mm diameter vapor cell.

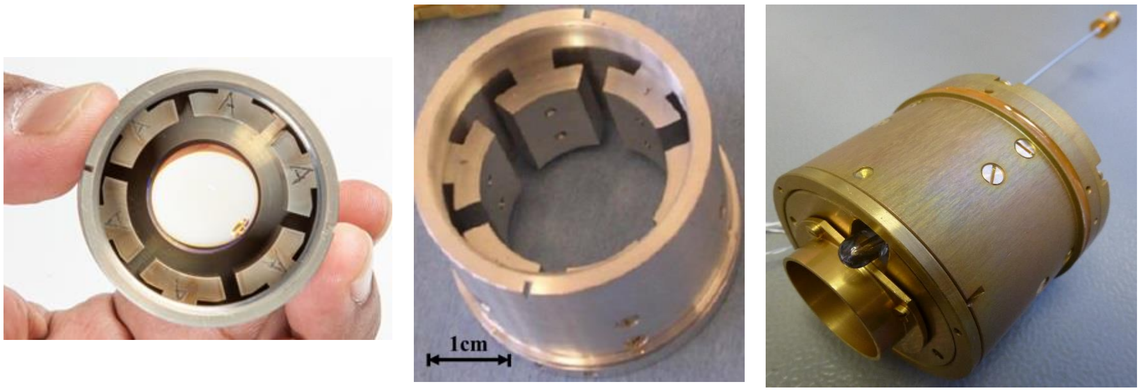

Figure 2.12: Photographs of the magnetron-type microwave cavity with six electrodes. The right photograph shows the assembled microwave cavity when the vapor cell is loaded.

The microwave cavity resonates at the ^{87}Rb clock's transition frequency of $\approx$6.835 GHz in a TE$_{011}$-like mode. Generally, in cylindrical microwave cavities, the TE$_{011}$ mode has the electric field that is mainly concentrated in the gaps between the electrodes and the magnetic field is confined within the loop perpendicular to the electric field. We are interested in the TE$_{011}$-like mode due to its magnetic field uniformity across the cell. Figure 2.13 shows the magnetic field distribution inside the cavity with a cylindrical geometry [51].

In the following we present the characterizations of the microwave cavity by measuring its resonance frequency, quality factor, temperature sensitivity and field orientation factor (FOF), which influence the clock's signal contrast and the clock's stability. We note that all the frequency measurements in this thesis were done against our H-Maser reference system.

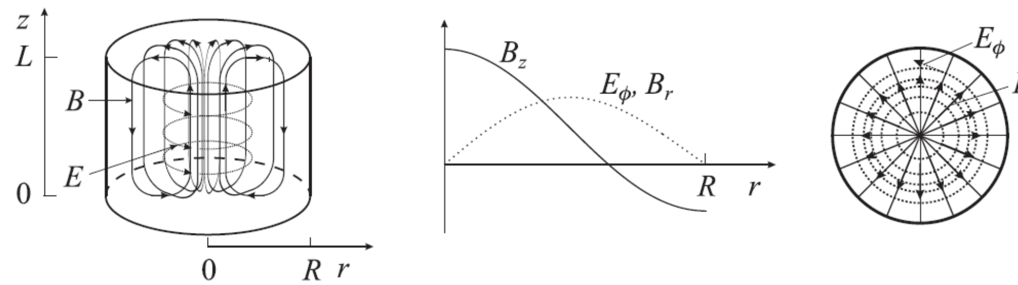

Figure 2.13: Left: Magnetic (full lines) and electric field lines (dashed lines) of TE_{011} mode in a cylindrical cavity. Middle: Radial field component amplitudes. Left: Top view. The figure is taken from [51].

2.3.2.1 Resonance Frequency and Quality Factor of the Cavity

The resonance frequency of the microwave cavity is obtained from the S_{11} parameter measured with the setup, a photograph of which is shown in figure 2.14. The measurement was done when the microwave cavity was mounted in the physics package and the vapor cell was placed in it. Microwaves with the frequency around 6.8 GHz and the power of -10 dBm pass through a circulator (JQL 6500T7100, no. 91003624) and are injected into the cavity using a microwave generator. A fraction of the microwave power is reflected back from the cavity to the circulator and passes through the microwave power detector (ZX 47-60 LN-S). Finally, the oscilloscope records the DC signal from the microwave power detector. The output power of the microwave detector is calibrated into the 1 MΩ oscilloscope resistance.

By scanning the microwave frequency around the resonance, a resonance frequency curve such as the one shown in figure 2.15 is observed. When the frequency of the injected microwave is in resonance with the cavity mode, more microwave power is coupled with the cavity and less power is reflected back to the circulator and consequently to the detector. From the resonance curve, the cavity's resonance frequency, ν_{cav}, and the quality factor, Q_{cav}, are obtained. The cavity quality factor is defined as:

$$Q_{cav} = \frac{\nu_{cav}}{\Delta\nu_{1/2}}, \tag{2.2}$$

where $\Delta\nu_{1/2}$ is the full-width half-maximum of the cavity resonance signal.

The cavity resonance frequency, ν_{cav}, is obtained when the microwave frequency is scanned near the resonance and the data was fitted to a quadratic function (inset of figure 2.15). The linewidth of the resonance curve, $\Delta\nu_{1/2}$, is obtained from the fitted the data to a Lorentzian function. When the cavity temperature was at T_{cav} = 65 °C, the cavity resonance frequency of $\nu_{cav} = 6,835,992,900\,\text{Hz} \pm 10\,\text{kHz}$ with a linewidth of $\Delta\nu_{1/2} \approx 46\,\text{MHz} \pm 1$ MHz was measured, which corresponds to the cavity quality factor of $Q_{cav} \approx 150$[1]. The cavity frequency detuning from the unperturbed clock frequency of ^{87}Rb, ν_{Rb}, was found to be $\Delta\nu_c = \nu_{cav} - \nu_{Rb} \approx 1.3$MHz which is a relevant parameter to estimate the cavity pulling instability (see section 1.7.3.4).

[1]This result was obtained when the cavity was loaded with the vapor cell. The cell temperature was 65 °C (close to the clock working condition).

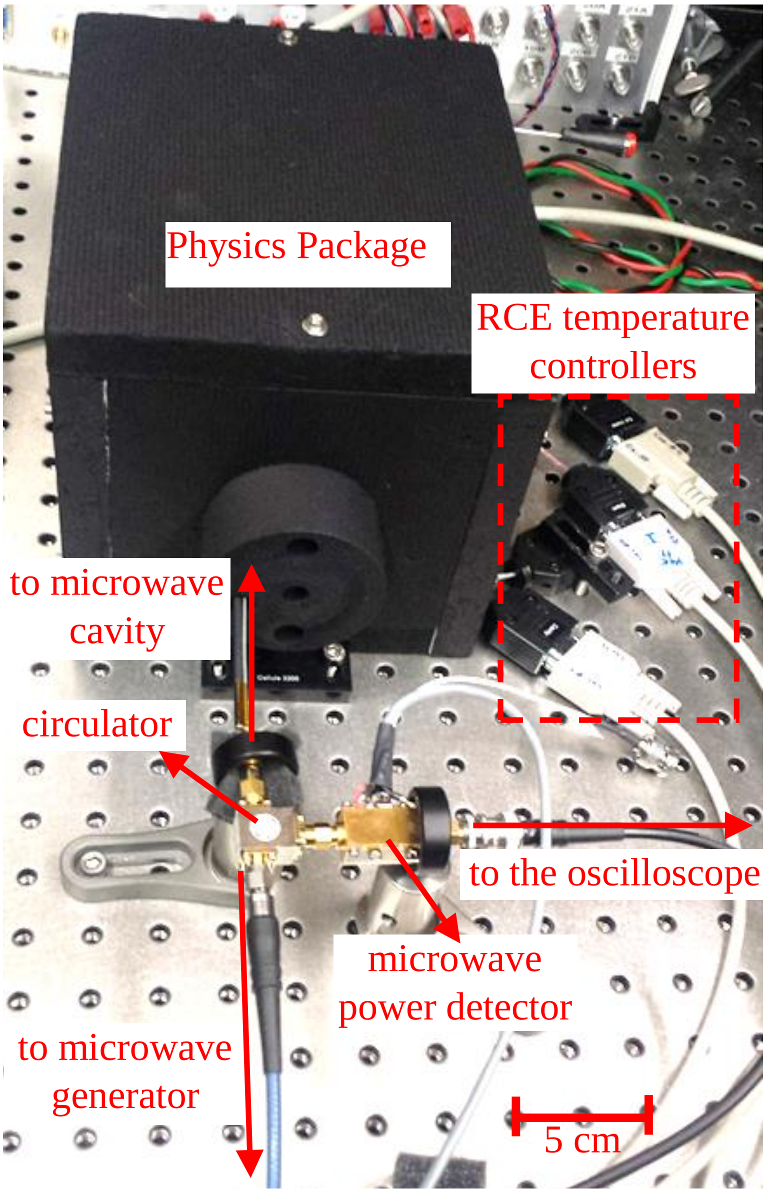

Figure 2.14: Photograph of the setup to measure the cavity resonance frequency.

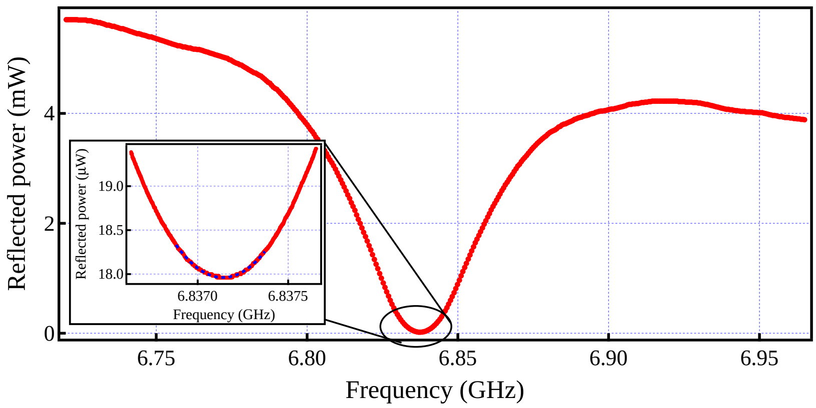

Figure 2.15: Cavity resonance frequency curve at ambient laboratory temperature of ≈ 21°C.

2.3.2.2 Cavity Temperature Coefficient

The temperature sensitivity of the cavity was measured while it was heated up step-by-step from the ambient temperature of 21°C. The waiting time between each step higher than T_{cav} = 40 °C was about three to four hours. The temperature set point propositions were based on the optimized working conditions of the previous Rb atomic clock in our laboratory [41]. The resonance frequency of the cavity was measured for each step (see section 2.3.2.1). Figure 2.16 shows the measured cavity resonance frequency as a function of the cavity temperature. By using a linear fit to this data, the temperature sensitivity of the cavity (the cavity temperature coefficient) is obtained $\Delta\nu_{cav}/\Delta T_{cav} \approx -40\,\text{kHz}/°\text{C}$. The cavity temperature coefficient is required to estimate the cavity pulling instability (see section 1.7.3.4 and equation (1.48)).

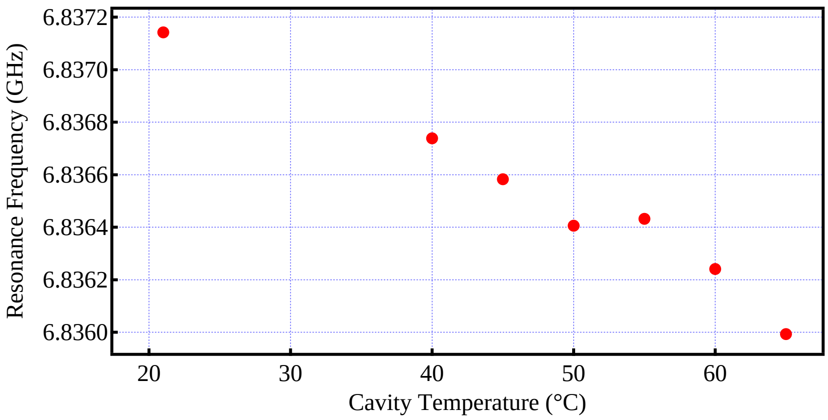

Figure 2.16: Measured cavity resonance frequency, ν_{cav}, as a function of the cavity temperature, T_{cav}. The waiting time between each step higher than T_{cav} = 40 °C was about 3-4 hours with the note that the waiting time between $T_{cav} = 50$°C and $T_{cav} = 55$°C was about 12 hours. The uncertainties are smaller than the circle sizes.

2.3.2.3 Field Orientation and Zeeman

Section 1.2.1 discussed how in an external static magnetic field (directional, z-axis) the hyperfine states of $5^2S_{1/2} : |F=1\rangle$ and $|F=2\rangle$ split into their corresponding Zeeman sub-levels (figure 1.4) according to equation (1.4). Due to the selection rules ($\Delta m_F = 0, \pm 1$) there are nine possible transitions between the Zeeman sub-levels of the ground states (figure 2.17). In the Zeeman transitions, if $\Delta m_F = 0$ the transition is called π and if $\Delta m_F = \pm 1$ the transition is called σ. The magnetic dipole selection rules relate the π-transitions to the microwave magnetic field component parallel to the C-field ($H_{\parallel}$), and the σ-transitions to the orthogonal component ($H_{\perp}$). In the atomic clocks, we are mainly interested in the π-transitions that are obtained if the microwave magnetic field is oriented along the C-field over the cell volume. Therefore, this field orientation is characterized by a parameter "field orientation factor" (FOF) ξ defined by [36]:

$$\xi = \frac{\int_{V_{cell}} H_{\parallel}^2 dV}{\int_{V_{cell}} H_{\parallel}^2 dV + \int_{V_{cell}} H_{\perp}^2 dV}. \tag{2.3}$$

A Zeeman spectrum shown in figure 2.18 was obtained by scanning the frequency of the injected microwave to the cavity around the clock transition frequency of the ^{87}Rb. The peak numbers in figure 2.18 correspond to the transition numbers in figure 2.17. Despite the nine transitions shown in figure 2.17, only seven peaks are visible in the Zeeman spectrum (figure 2.18). This can be attributed to the fact that the peak number 1 (and 2) –in figure 2.18– corresponds to the overlapping of two peaks corresponding to the transitions $|F=1, m_F=0\rangle \leftrightarrow |F=2, m_F=-1\rangle$ and $|F=1, m_F=-1\rangle \leftrightarrow |F=2, m_F=0\rangle$

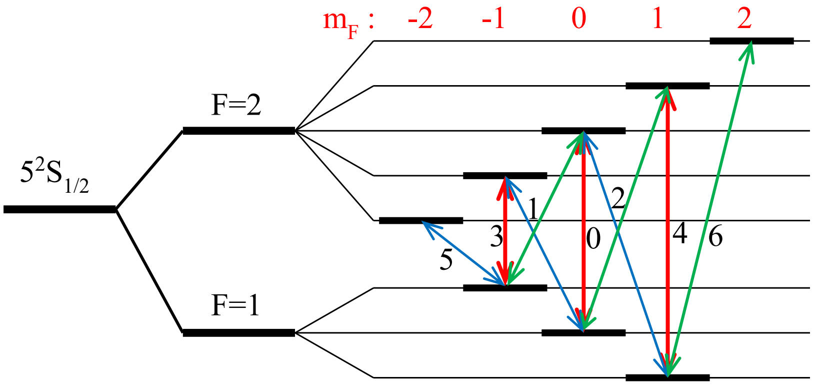

Figure 2.17: Possible transitions between the Zeeman sub-levels of two ground states: $5^2S_{1/2}\,|F=1\rangle$ and $|F=2\rangle$ in presence of a weak static magnetic field in ^{87}Rb.

($|F=1, m_F=0\rangle \leftrightarrow |F=2, m_F=1\rangle$ and $|F=1, m_F=1\rangle \leftrightarrow |F=2, m_F=0\rangle$) because the energy difference between these pairs is close to zero and their peaks are close to each other.

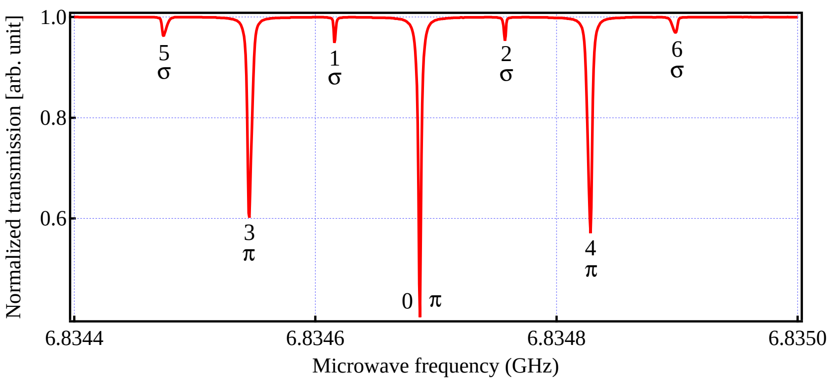

Figure 2.18: Zeeman spectra for the transitions between the two hyperfine levels. The injected microwave power to the cavity was $-20\,$dBm and the C-field amplitude was about 100 mG.

In a vapor cell, FOF is defined as the ratio of the magnetic field component needed to drive the clock transition with respect to the total field energy over the entire vapor cell volume. The FOF is determined experimentally by [36]:

$$\xi_{exp} = \frac{\int S_\pi}{\int S_\pi + \int S_\sigma}, \tag{2.4}$$

where $\int S_\pi$ and $\int S_\sigma$ are the integrated signal strengths over all the corresponding Lorentzian peaks for $\Delta m_F = 0$ and $\Delta m_F = \pm 1$, respectively, where π and σ transitions contribute with equal weight [87]. These signal strengths S_i are proportional to H_z^2, for small microwave powers. In our cavity, the FOF was measured $\xi_{exp} \approx 0.92$ at the Rb resonant frequency which means that 92% of the microwave field is oriented along the C-field. We note that this result was obtained after a demagnetization[1] of the cavity and before the demagnetization the FOF was measured about $\xi_{exp} \approx 0.85$.

[1]Principle of the demagnetization is to induce a magnetic induction into the magnetic shielding of the cavity which is greater than the shielding saturation induction and then run a hysteretic cycle of the material in decreasing slowly the magnetic induction down to zero.

2.3.3 Magnetic Shielding

We discussed above in section 1.2.1 that the clock transition frequency in the first order is unaffected by fluctuations of magnetic fields, but the second order fluctuations perturb its frequency. Therefore, it is necessary to suppress the magnetic field fluctuations in the vapor cell that are caused by changes in the external magnetic field outside of the physics package. In our physics package two layers of magnetic μ-metal shielding are used, which is the same as the one used for the physics package presented in [41] by T. Bandi. The inner shield's dimensions are as follows: a radius of 44 mm, a thickness of 0.8 mm and a length of 52 mm. The outer shield as a radius of 49 mm, a thickness of 0.8 mm and a length of 100 mm. T. Bandi measured the longitudinal shielding factor of $S_L \approx 3000 \approx 70\,\text{dB}$ in his physics package by using Helmholtz coils. We expect the same S_L in our physics package.

2.4 C-Field Inhomogeneity in the Vapor Cell

In section 1.6 we discussed how in an Rb atomic clock, in addition to the various collisions of the Rb atoms in the vapor cell, the inhomogeneity of the C-field in the vapor cell is also a source of relaxation processes. In this section, we evaluate the C-field inhomogeneity in the Rb vapor cell by using the Zeeman spectrum and measuring the broadening of the Zeeman lines.

The Zeeman spectrum is recorded by using CW-DR scheme when sweeping the microwave frequency and measuring the transmission signal with a photodetector after the vapor cell. Figure 2.19 shows the recorded Zeeman spectra for various C-currents (the current applies to the coils to create the C-field) from 0.8 mA to 5 mA (which correspond to field strength from 53 mG to 335 mG, see figure 2.20). The frequency detuning step is set to 10 Hz for each Zeeman spectrum. In these measurements, the laser input power and the injected microwave power to the cavity are set to 120 μW and 1 μW, respectively. The corresponding peaks in the Zeeman spectrum and the atomic transitions were presented in figures 2.17 and 2.18. The central peak in the Zeeman spectrum corresponds to the clock transition $|F=1,m_F=0\rangle \leftrightarrow |F=2,m_F=0\rangle$ and we label it with π^0 in the following. The peaks with higher amplitudes on the left-hand side and on the right-hand side of the π^0 peak correspond to $|F=1,m_F=-1\rangle \leftrightarrow |F=2,m_F=-1\rangle$ and $|F=1,m_F=1\rangle \leftrightarrow |F=2-,m_F=1\rangle$ transitions, respectively, and we label them with π^- and π^+ in the following.

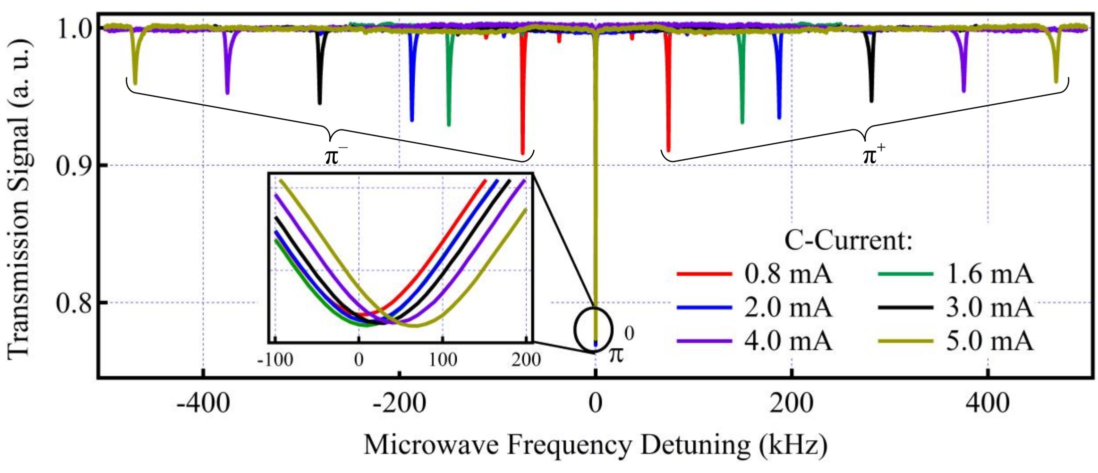

Figure 2.19: Recorded Zeeman spectra in various applied C-currents from 0.8 mA to 5 mA. The microwave frequency is detuned from 6,834,686,395 Hz.

From the Breit-Rabi formula (1.6) and the second order Zeeman shift (section 1.7.3.1), the frequency shift with respect to the C-field amplitude is obtained by $(m_{F_1} + m_{F_2})0.7\,\mathrm{MHz/G}$. With this relation, we can estimate the C-field strength in the vapor cell. For this, we obtain the frequency splitting between π^0 and π^+ peak positions, i.e. $\nu_{\pi^+} - \nu_{\pi^0}$, from the Zeeman spectrum and calculate the C-field amplitude B_0 in mG from:

$$B_0 = \frac{\nu_{\pi^+} - \nu_{\pi^0}}{700\,(\frac{\mathrm{Hz}}{\mathrm{mG}}) \cdot \left((m_{F_1}^{\pi^+} + m_{F_2}^{\pi^+}) - (m_{F_1}^{\pi^0} + m_{F_2}^{\pi^0})\right)}, \tag{2.5}$$

where, $m_{F_1}^{\pi^+}$ and $m_{F_2}^{\pi^+}$ are both equal to 1 and $m_{F_1}^{\pi^0}$ and $m_{F_2}^{\pi^0}$ are both equal to 0. Using the same treatment we calculate B_0 from the frequency splitting between π^- and π^0 peaks or between π^- and π^+ peaks. Figure 2.20 shows the obtained B_0 as a function of the applied C-current by using equation (2.5) in our Rb atomic clock for the three mentioned frequency splittings between π^-, π^0 and π^+ peaks. The calculated B_0 from these three peak splittings are in very good agreement (less than $\pm 0.5\%$ difference). In the following, we consider only the splitting and broadenings of the π^0 and π^+ peaks to estimate the C-field inhomogeneity in the vapor cell. Figure 2.20 shows how the C-field strength is linearly proportional to the applied C-current. By extrapolating to zero C-current, a residual C-field is achieved -0.67 ± 0.01 mG in the Rb vapor cell. The negative sign describes the direction of this residual field which is opposite to the applied C-field.

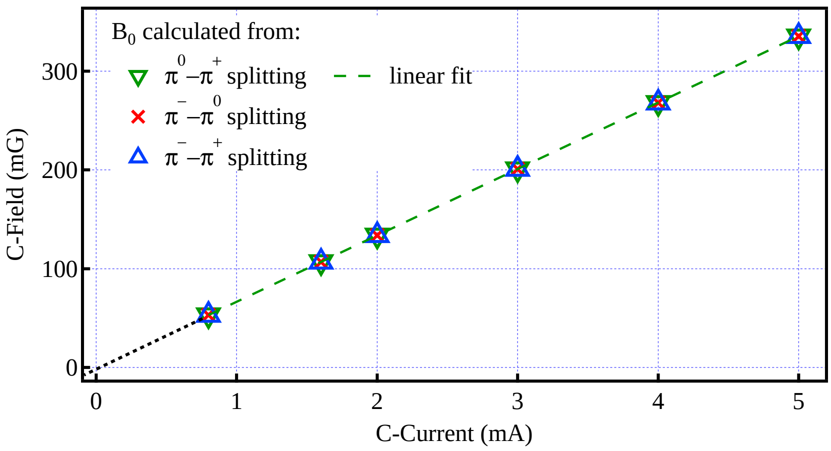

Figure 2.20: Calculated C-field amplitude B_0 from equation (2.5) as a function of the C-current in our Rb atomic clock. The uncertainties are not visible because they are less than ± 1 %.

We estimate the C-field inhomogeneity from the line broadening of π^0 and π^+ peaks in the Zeeman spectra. Figure 2.21 shows the π^0 peaks for different C-currents. These π^0 peaks have symmetric Lorentzian shapes and, in addition, have similar peak-heights and similar linewidths. We label their FWHM with $\Delta\nu_{50\%}^{\pi^0}$ and their broadenings at 20 % of the maximum peak-heights with $\Delta\nu_{20\%}^{\pi^0}$. For these π^0 peaks, $\Delta\nu_{50\%}^{\pi^0}$ and $\Delta\nu_{20\%}^{\pi^0}$ are extracted from the fitting data to Lorentzian functions. The results are listed in table 2.1. The statistical uncertainty is obtained below 1 Hz from the fits for thee line broadenings.

Figure 2.22 shows the π^+ peaks for different C-currents. In this graph, in order to compare the line-broadening more easily, the lowest transmission of each π^+ peak is centered to zero in the x axis. The π^+ peaks have asymmetric shapes towards the π^0 peaks (see figure 2.22). The asymmetric shapes of the π^+ and π^- peaks can be explained by the presence of the inhomogeneity of the C-field in the vapor cell. Since various Rb atoms in the cell may experience different C-fields. Figure 2.22 shows

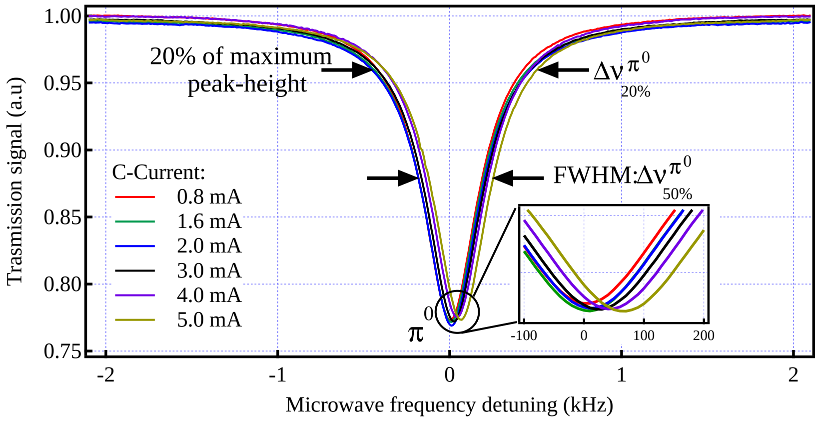

Figure 2.21: π^0 peaks from the recorded Zeeman spectra at various applied C-currents.

that increasing the C-current (or the C-field) results in a broader π^+ peak. With this observation we can claim that the larger C-field amplitude results in higher C-field inhomogeneity in the vapor cell. To prove this claim, we study the broadening of the π^+ peaks at different C-fields. Because of the asymmetric shapes of π^+ (and π^-) peaks, a single Lorentzian function does not fit them. Therefore, we extract their broadenings manually from each recorded Zeeman spectrum (figure 2.22) at two peak-height levels: 1) $\Delta\nu_{20\%}^{\pi^+}$ measured at 20 % of the maximum peak-height and 2) $\Delta\nu_{50\%}^{\pi^+}$ measured at 50 % of the maximum peak-height. These peak-height levels are shown in figure 2.22 only for the case of 0.8 mA C-current. The obtained broadenings for the π^+ peaks are listed in table 2.1.

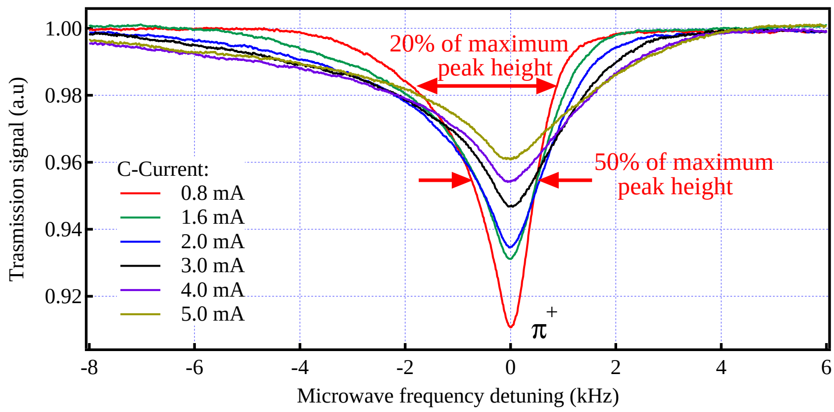

Figure 2.22: π^+ peaks from the recorded Zeeman spectra at various applied C-currents. In order to compare the line-broadening, the peak positions (lowest transmission) are centered to zero in the x axis.

Table 2.1 lists $\Delta\nu_{x\%} = \Delta\nu_{x\%}^{\pi^+} - \Delta\nu_{x\%}^{\pi^0}$, the broadening difference between the π^+ and π^0 peaks, as a function of the C-current (and the C-field) for both cases of 50 % and 20 % of the maximum peak-heights. We can estimate the absolute C-field inhomogeneity for various applied C-currents in the vapor cell by using equation (2.5). Consequently, from the absolute field inhomogeneity, we can calculate the relative C-field inhomogeneity in our vapor cell. The graphs in figure 2.23 show the absolute and relative C-field inhomogeneity as a function of the C-field in the vapor cell. It is seen that by increasing the C-field strength, the C-field inhomogeneity increases in the vapor cell (figure 2.23.a), and the relative C-field inhomogeneity slightly reduces by increasing the C-field strength (figure 2.23.b). However, at lower C-field strengths (less than 50 mG) the relative C-field inhomogeneity rises drastically (figure 2.23.b). This phenomenon can be attributed to the presence of the field distribution of the residual field in the coil due to the geometrical design of the coil. Figure 2.23.b shows that in our Rb atomic clock at the

Table 2.1: Obtained line broadenings for π^0 and π^+ peaks at 20% and at 50% of the maximum peak-heights and their broadening differences for various applied C-currents.

C-current (mA)	0.8	1.6	2	3	4	5
C-field (mG)	53	107	134	201	268	335
$\Delta\nu^{\pi^0}_{20\%}$ (Hz)	795	810	815	807	810	811
$\Delta\nu^{\pi^0}_{50\%}$ (Hz)	401	404	408	404	402	403
$\Delta\nu^{\pi^+}_{20\%}$ (Hz)	2670	3700	4370	5780	7180	8400
$\Delta\nu^{\pi^+}_{50\%}$ (Hz)	1240	1750	2020	2600	2950	3430
$\Delta\nu_{20\%}$ (Hz)	1900	2890	3555	4973	6370	7589
$\Delta\nu_{50\%}$ (Hz)	839	1346	1612	2196	2548	3027

working C-field of about 100 mG, the mean relative C-field inhomogeneity is below 2%. In chapter 4, we show the impact of this C-field inhomogeneity in the vapor cell on the coherence relaxation time T_2.

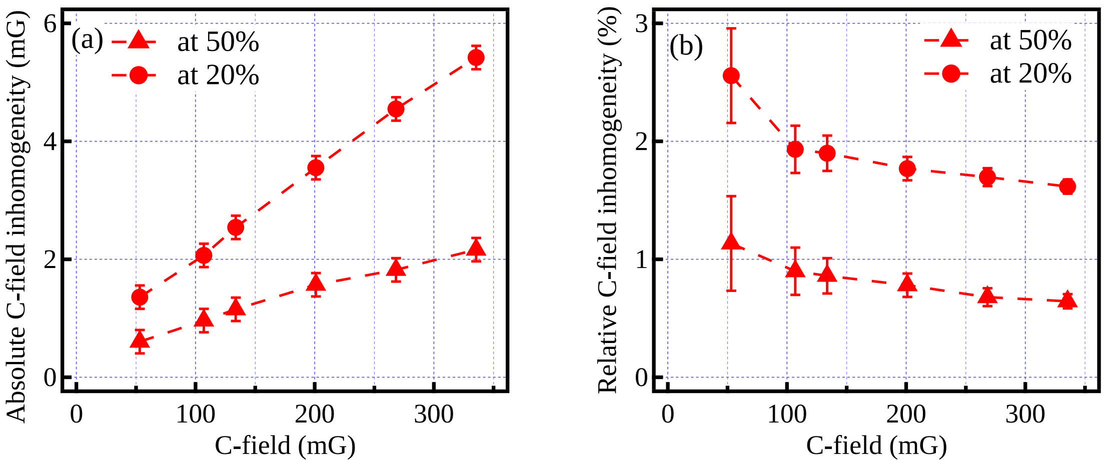

Figure 2.23: (a): Absolute C-field inhomogeneity as a function of measured C-field. (b): Relative C-field inhomogeneity as a function of measured C-field.

2.5 Local Oscillator (LO)

The LO is designed, developed and built at INRIM [34, 90]. Figure 2.24 shows the photograph of the LO which is used in this thesis. A so-called synthesis-chain is responsible for generating a microwave interrogation signal and controlling its frequency. The LO synthesizer generates 6.835 GHz of microwave frequency and a power output in the range of -40 dBm up to 0 dBm with steps of 1 μHz with a span of 1.5 GHz that ensures the full Zeeman spectrum. The LO is capable of operating in two modes: a sweep mode for covering and a locked mode for the clock operation. The measured output power of the locked OCXO at 10 MHz was 2 dBm. Phase noise of the LO is an important parameter in view of minimizing the Dick effect [71] that influences clock stability. Figure 1.13 (the brown curve) shows that the LO phase noise at the carrier frequency of 6.8 GHz has a flicker level at -70 dBrad^2/Hz and a noise floor at -111 dBrad^2/Hz [41]. As presented in section 1.7.2.2, from equation (1.36) the Dick effect stability limit was obtained at the level of $\sigma_y^{LO} \approx 7\times10^{-14}\tau^{-1/2}$. Bandi et al. reported a relative microwave power stability of the LO at the level of $\sigma P_{\mu w}/P_{\mu w} \approx 10^{-3}$ at 10^4 [41].

Figure 2.24: Photograph of the LO. The LO is designed, developed and built at INRIM [34, 90].

2.6 Conclusion

We presented the experimental setup used in this thesis which is an Rb atomic clock that consists of the following: 1) a laser frequency stabilized system, 2) a physics package that contained a microwave magnetron-type cavity and a vapor cell and 3) a local oscillator. The design details and characterizations of the laser system, microwave cavity and the vapor cell were presented. The laser source provides a stable intensity and a stable frequency. The laser output achieves a relative intensity stability below 10^{-11} and a frequency stability of below 10^{-4}, when the laser frequency is locked to a sub-Doppler Rb transition, in a time scale of 10^4 s. The chapter also discussed the compact magnetron-type cavity with six-electrodes with a volume of only 45 cm^3 that holds the enlarged 25 mm vapor cell and resonates at the ^{87}Rb ground state frequency. The microwave field of the magnetron-type cavity has a TE_{011}-like mode aligned with the applied C-field and with the propagation vector of the laser beam. For the microwave cavity, a relative low quality factor of approximately $Q_{cav} \approx 150$ was measured while its temperature sensitivity of $\Delta\nu_{cav}/\Delta T_{cav} \approx -40\,\mathrm{kHz}/^{\circ}\mathrm{C}$ was obtained. The field orientation factor of $\xi_{exp} \approx 92\%$ was obtained in the vapor cell using Zeeman measurements. We presented the newly designed and developed cylindrical vapor cell with an overall volume of about 12 cm^3. The vapor cell confines the Rb atoms with buffer gases N_2 and Ar. For this vapor cell, the cell-stem was produced with a volume 10 times smaller than the previous version [35] to reduce the impact of the redistribution of the buffer-gas density due to the temperature gradient between the cell-body and the cell-stem via the ETS effect [94]. We measured the stem temperature coefficient for our vapor cell at the level of $TC_{stem} \approx 1.1 \times 10^{-12}/\mathrm{K}$ which was in very good agreement with our estimation. We estimated the relative C-field inhomogeneity in the vapor cell at about 2% at the working point of an applied C-field about 100 mG. This C-field inhomogeneity is a source of relaxation phenomena that influences the coherence relaxation T_2 of the Rb atoms in the vapor cell. In chapter 4, we will demonstrate an experimental method to suppress this effect and measure the intrinsic T_2. Characterization and evaluation results of various components of our Rb clock can guarantee that this clock is capable to operate in the Ramsey-DR scheme; this will be shown in the next chapter.

3 Realization and Optimization of a Ramsey-DR Clock with a Low-Q Cavity

In this chapter, we demonstrate using a cavity with a low-quality factor for realizing a rubidium atomic clock (see chapter 2) that operates in the Ramsey-DR scheme as introduced in section 1.5. In section 3.1, first we recall the timing sequence of the Ramsey-DR scheme with laser and microwave pulses. Next, we use Rabi oscillations and adjust the microwave pulse parameters (duration and amplitude) to create a $\pi/2$ microwave pulse. Then, the Ramsey pattern is obtained, and the clock signal –the central fringe of the Ramsey pattern– is optimized as a function of intensity and duration of the laser pulses for both optical pumping and optical detection phases. In section 3.3, the uniformity of the microwave magnetic field in the cavity is evaluated. The temperature sensitivity of the vapor cell in terms of their influences on the clock frequency stability are presented in section 3.4. In section 3.5, we present the results of the LS measurements in our Rb atomic clock operating in the Ramsey-DR scheme. In addition, we present a preliminary model to describe the origin of this LS effect in our Rb atomic clock. Then, we present preliminary studies on the microwave power shift in our Ramsey-DR Rb clock. Finally, in section 3.7, we discuss the effect of the duration of the optical detection pulse on the clock stability.

3.1 Ramsey Signal

In this section, we show how to optimize the clock signal in terms of its contrast and linewidth obtained from our Rb clock setup described in chapter 2. We operate the Rb clock in the Ramsey-DR scheme, therefore the clock signal is the central fringe of the Ramsey pattern. We characterize the impact of the duration and intensity of laser and microwave pulses on the clock signal. We use the laser system (see section 2.2) for the optical pumping and optical detection sequences. The microwave synthesizer (see section 2.5) provides the microwave pulses. Figure 3.1 illustrates the timing sequence of the Ramsey-DR scheme. The physics behind the three sequences of optical pumping, microwave interrogation and optical detection were previously discussed in section 1.5. The pulse durations of optical pumping, microwave and optical detection are shown by t_p, τ_m and t_d, respectively, in figure 3.1 and in the following subsections.

The measurement results presented in this section are achieved when the cavity and cell-stem temperatures are set to $T_{cav} = 63.2\,^{\circ}\mathrm{C}$ and $T_{stm} = 59.2\,^{\circ}\mathrm{C}$ (see section 3.4), respectively, and the C-current is set to 1.6 mA which corresponds to a C-field about 100 mG (see section 2.4).

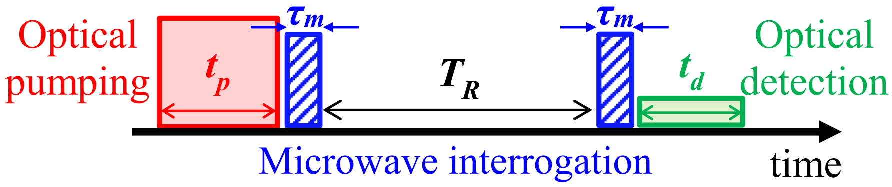

Figure 3.1: Timing sequence of Ramsey-DR scheme.

3.1.1 Microwave Pulse Parameters

In a ^{87}Rb atomic clock operating in a DR scheme, a clock resonance line can be observed when the microwave frequency sweeps near the frequency of the ^{87}Rb clock transition. Section 1.3.2.2 shows that the central fringe of the Ramsey pattern meets its maximum contrast if the microwave pulses are $\pi/2$ pulses. Therefore, in our Ramsey-DR atomic clock, we aimed to find a condition to create $\pi/2$ microwave pulses by adjusting the duration and amplitude of the applied microwave pulses to certain values. We recorded the central fringe of the Ramsey pattern while one of the two variables, the duration τ_m or the amplitude of the microwave pulses, varied and the other variable remained constant. In our experiments, we recorded the Ramsey central fringe and measured its contrast when the microwave pulse duration was fixed at $\tau_m = 0.4$ ms and the microwave pulse power was varied. Figure 3.2 shows the several recorded Ramsey central fringes for various microwave pulse powers. For these measurements, the laser frequency was stabilized to the sub-Doppler cross-over transition CO10-11 (see figure 2.10); t_p, t_d and T_R were set at 0.4 ms, 0.7 ms and 3 ms, respectively; and the laser input power to the cavity during optical pumping and optical detection were fixed at 13 mW and 125 μW, respectively.

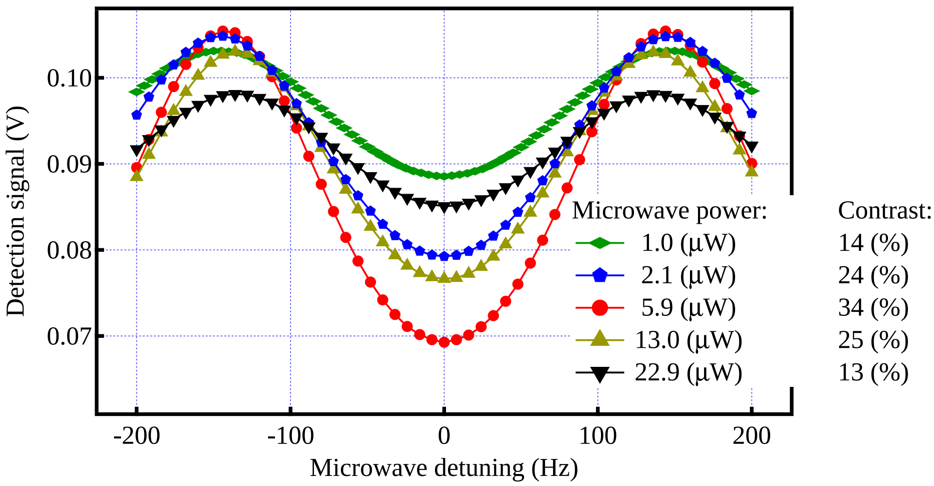

Figure 3.2: Recorded Ramsey central fringes for various microwave power injected to the cavity. The contrast of the Ramsey central fringe varies by varying the microwave power. In these measurements: $t_p = 0.4$ ms, $t_d = 0.7$ ms and $T_R = 3$ ms. The laser frequency is stabilized to the sub-Doppler cross-over transition CO10-11 (see figure 2.10) and its input power to the cavity during the optical pumping and optical detection is 13 mW and 125 μW, respectively. The microwave frequency is detuned from 6,834,686,395 Hz.

Generally, the Ramsey central fringe is characterized by its linewidth and its contrast. The linewidths of all Ramsey central fringes shown in figure 3.2 were measured about $\Delta\nu_{1/2} = 160 \pm 5$ Hz. However, figure 3.2 demonstrates that by increasing the microwave power, the Ramsey central fringe contrast increases until reaching a maximum and then decreases. This is clearly visible in figure 3.3 which shows the contrast of the Ramsey central fringe as a function of the microwave pulse power, also known as Rabi oscillation. The Rabi oscillation measurement is also used to evaluate microwave field uniformity inside the cavity (see section 3.3). In figure 3.3, the first maximum represents a configuration for each of the $\pi/2$ microwave pulses in our Rb clock, which occurs when the microwave pulse power is 5.9 μW and its duration is $\tau_m = 0.4$ ms. At this condition, the Ramsey central fringe contrast is approximately of 35%.

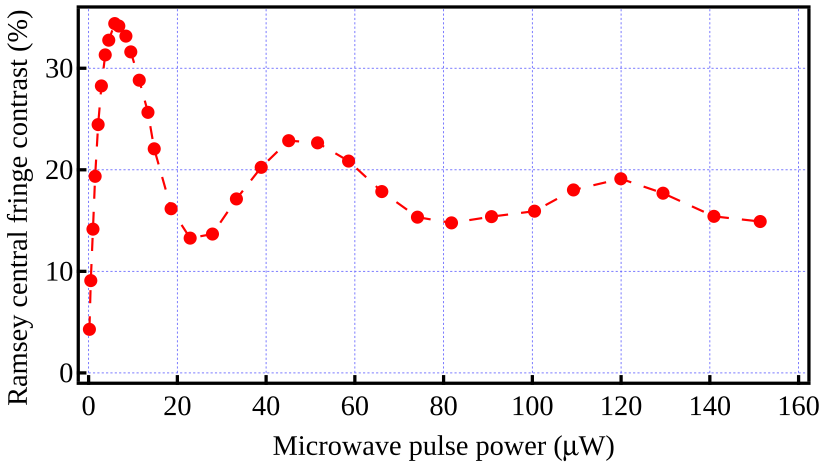

Figure 3.3: Rabi oscillations; Ramsey central fringe contrast as a function of input microwave power to the cavity.

Typically in Rabi oscillations, the microwave pulse area –defined as the product of pulse amplitude and pulse duration– is used rather than the microwave pulse power. Because the pulse amplitude is proportional to the square root of pulse power, the pulse area is also proportional to the multiplication of the square root of pulse power and the pulse duration. Figure 3.4 shows the contrast of the Ramsey central fringe as a function of microwave pulse area. The first maximum occurs when both of the microwave pulses are $\pi/2$. The second and the third maximums occur for $3\pi/2$ and $5\pi/2$ microwave pulses, respectively, when the microwave field is perfectly homogeneous across the cavity (which was not the case in our cavity). Next, we evaluated the effect of other parameters on the Ramsey signal when the microwave pulse power and duration were fixed at 5.9 μW and $\tau_m = 0.4$ ms, respectively.

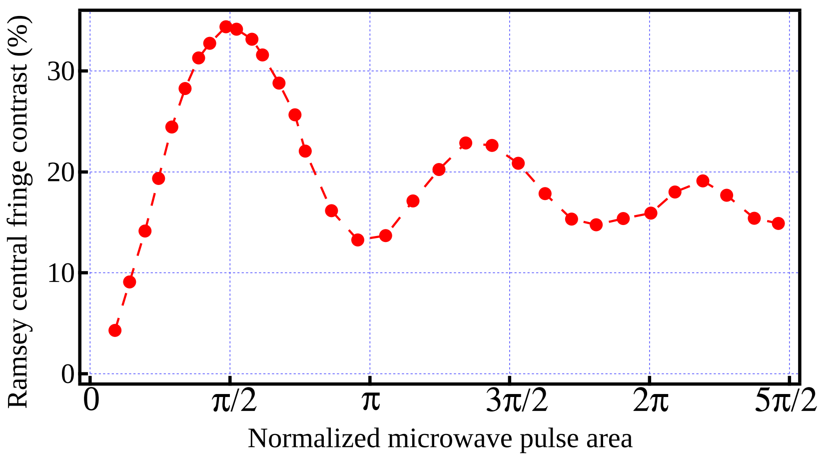

Figure 3.4: Rabi oscillations; Ramsey central fringe contrast as a function of the microwave pulse area (for each of the two microwave pulses employed) Due to the microwave field inhomogeneity in our cavity the second and third maximums do not occur for $3\pi/2$ and $5\pi/2$ microwave pulses, respectively.

3.1.2 Optical Pulses Parameters

We studied the effects of durations (t_p and t_d) and input powers (P_p and P_d) of optical pumping and optical detection pulses on the Ramsey central fringe. For these measurements, the Ramsey time was $T_R = 3\,\text{ms}$, and $\pi/2$ microwave pulse had an input power and a duration equal to $5.9\,\mu\text{W}$ and $\tau_m = 0.4\,\text{ms}$, respectively.

Figure 3.5 shows the Ramsey central fringe contrast as a function of optical pumping duration, t_p, when laser input powers to the cavity are fixed at $P_p = 13\,\text{mW}$ and $P_d = 125\,\mu\text{W}$ during optical pumping and optical detection pulses, respectively. Figure 3.5 shows that increasing t_p results in increased of the Ramsey central fringe contrast; at a t_p longer than 2 ms, the contrast became approximately 39% saturated. Figure 3.6 shows the Ramsey central fringe contrast versus optical pumping power P_p, when t_p and t_d were fixed at 0.4 ms and 0.7 ms, respectively. The Ramsey central fringe contrast was saturated at the level of approximately 35% for our working conditions.

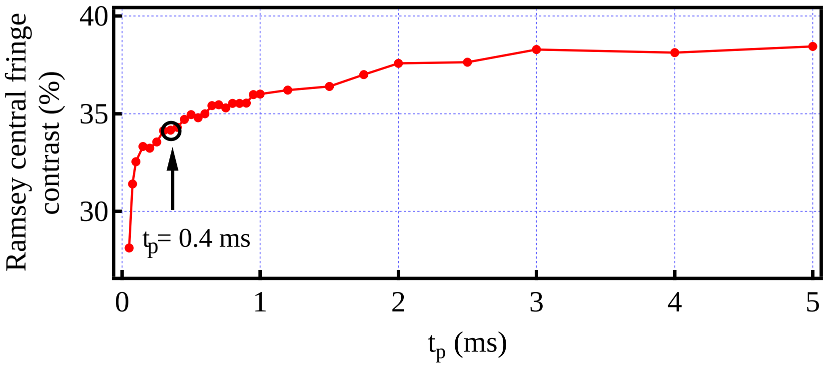

Figure 3.5: Ramsey central fringe contrast vs optical pumping pulse duration t_p when pumping power P_p=13 mW, detection power P_d=125 μW and detection pulse duration t_d=0.7 ms.

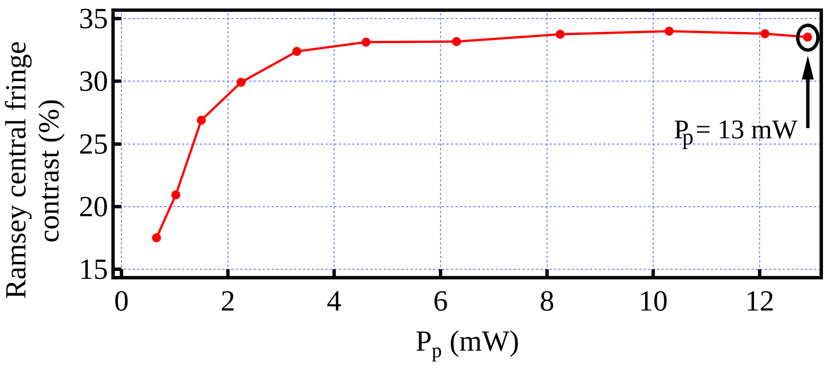

Figure 3.6: Ramsey central fringe contrast vs optical pumping power P_p when pumping pulse duration t_p=0.4 ms, detection power P_d=125 μW and detection pulse duration t_d=0.7 ms.

Figure 3.7 shows the Ramsey central fringe contrast as a function of optical detection duration t_d when the laser pumping and laser detection input powers were fixed at $P_p = 13\,\text{mW}$ and $P_d = 125\,\mu\text{W}$, respectively. Figure 3.8 shows the Ramsey central fringe contrast as a function of optical detection power P_d when the optical pumping and optical detection durations were fixed at $t_p = 0.4\,\text{ms}$ and $t_d = 0.7\,\text{ms}$, respectively. These figures demonstrate that increasing t_d or P_d result in decreasing contrast. This occurs because increasing detection duration or detection laser power causes re-pumping of the atomic sample, which consequently decreases the Ramsey central fringe contrast.

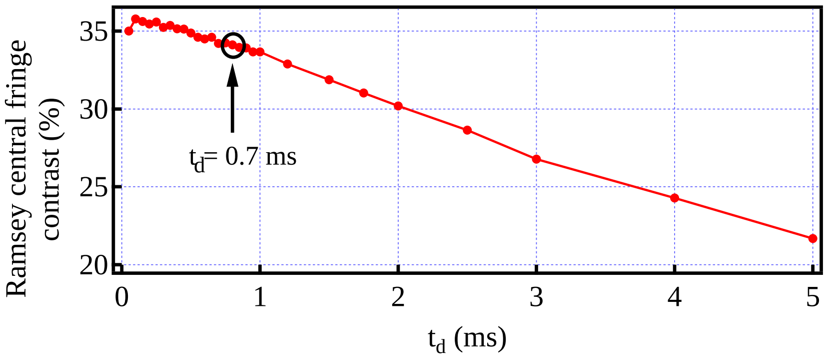

Figure 3.7: Ramsey central fringe contrast vs optical detection pulse duration t_d when pumping power P_p=13 mW, detection power P_d=125 μW and pumping pulse duration t_p=0.4 ms.

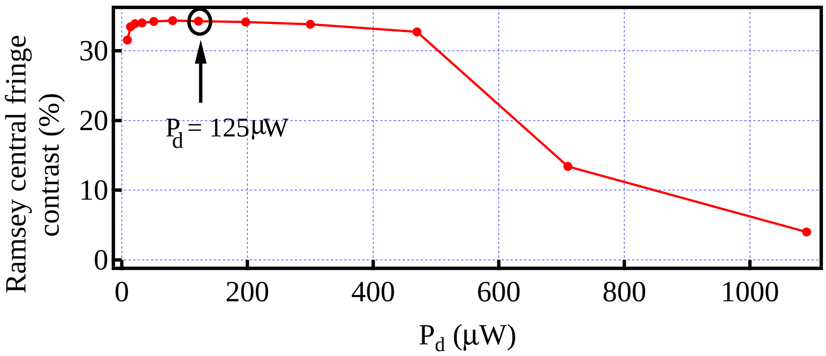

Figure 3.8: Ramsey central fringe contrast vs optical detection power P_d when pumping power P_p=13 mW, pumping pulse duration t_p=0.4 ms and detection pulse duration t_d=0.7 ms.

3.1.3 Ramsey Time

After optimizing the optical and microwave pulses parameters (see previous sections), here, we discuss the impact of the Ramsey time T_R on the clock signal. Figure 3.9 shows obtained Ramsey patterns for several Ramsey time from $T_R = 0.5$ ms to $T_R = 8$ ms. For these measurements, the laser stabilized to the sub-Doppler cross-over transition CO10-11 (see figure 2.10), optical pumping and optical detection durations were fixed at $t_p = 0.4$ ms and $t_d = 0.7$ ms, respectively, and laser pumping and laser detection powers were set to $P_p = 13$ mW and $P_d = 125\ \mu$W, respectively. The $\pi/2$ microwave pulses had a duration of $\tau_m = 0.4$ ms and a power of 5.9 μW. In all Ramsey patterns shown in figure 3.9, the envelope signals have the same linewidth of about 2500 Hz which is equal to $1/\tau_m$ (inverse of the duration of the Rabi pulses). By increasing the Ramsey time, the cycle time T_C increased, leading to a reduced detection signal level (consequently lower signal contrast) due to the atomic coherence decay (decoherence relates to T_2 relaxation, which was also measured and is presented in chapter 4.).

The contrast and linewidth of the Ramsey central fringes both decreased when Ramsey time (T_R) increased. These inverse relationships are clearly visible in figure 3.10, where contrast and linewidth of the Ramsey central fringe are plotted as functions of Ramsey time T_R. Generally, in atomic clocks, a clock signal with a higher contrast and a narrower linewidth is favorable to achieve better clock stability. However, as discussed above, in our Rb clock operating in the Ramsey-DR scheme, a trade-off exists between a high-contrast clock signal and a narrow fringe with respect to the Ramsey time T_R (see figure 3.10).

The Ramsey time is mainly limited by the relaxation mechanisms occurring inside the vapor cell

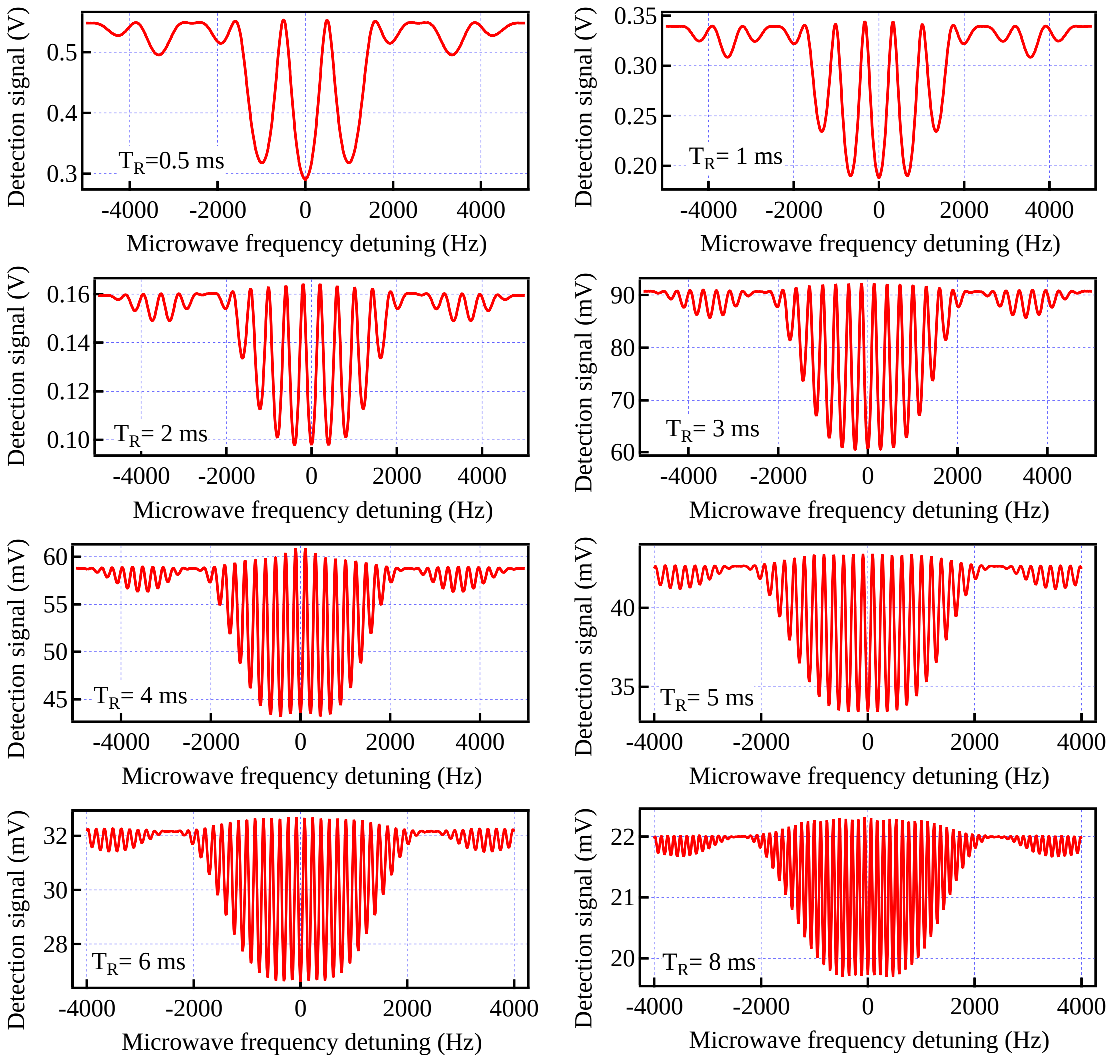

Figure 3.9: Recorded Ramsey patterns for various Ramsey time from $T_R = 0.5$ ms to $T_R = 8$ ms. $t_p = 0.4$ ms, $t_d = 0.7$ ms, $P_p = 13$ mW and $P_d = 125\,\mu$W. The $\pi/2$ microwave pulses have the duration of 0.4 ms and a power of 5.9 μW. Zero microwave detuning corresponds to 6,834,686,395 Hz.

and it is optimized when it is of the order of coherence relaxation time T_2 [34]. However,the optimum Ramsey time in our Rb clock is estimated in section 3.2 based on the measured short-term stability of our Rb clock. The theoretically calculated linewidth of the Ramsey central fringe based on equation (1.18) is also shown in figure 3.10 (black dashed line). Because equation (1.18) was obtained based on the $T_R \gg \tau_m$ assumption, our experimental results satisfy this theoretical equation for $T_R > 2$ ms but not for $T_R < 2$ ms. In another study, Micalizio et al. predicted the linewidth of the Ramsey central fringe when also taking to account the microwave pulse duration τ_m by [102]:

$$\Delta\nu_{1/2} = \frac{1}{2(T_R + 4\tau_m/\pi)}. \tag{3.1}$$

The green dashed line in figure 3.10 shows the estimated Ramsey central fringe linewidth based on the above formula where $\tau_m = 0.4$ ms. It is seen that, this estimation is in a better agreement with our measurement results compared to previous estimation from equation (1.18), particularly for short Ramsey times $T_R < 1$ ms.

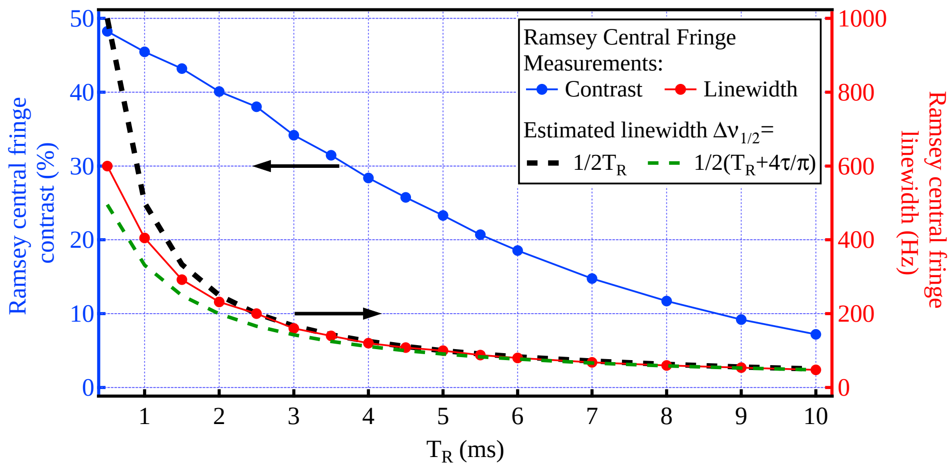

Figure 3.10: Blue circle: measured Ramsey central fringe contrast vs T_R. Red circle: measured Ramsey central fringe linewidth vs T_R. Black and green dash lines show the estimated Ramsey central fringe linewidth based on equations (1.18) and (3.1) respectively. For measurements and estimations the duration of the microwave pulse was $\tau_m = 0.4$ ms.

3.2 Short-Term Stability and the Ramsey Time

In section 3.1.3, the trade-off between a high-contrast clock signal and a narrow fringe with respect to the Ramsey time was shown in figure 3.10. Here, we evaluate the effect of the duration the Ramsey time T_R (and consequently the cycle time T_C) on the short-term stability of our Rb clock operating in the Ramsey-DR scheme. This evaluation was done based on the theoretical formula (1.35) and the measurement results presented in the following.

We estimated the shot-noise-limit $\sigma_y^{SN}(\tau)$ and the detection noise during the detection phase $\sigma_y^{det}(\tau)$ from equations (1.29) and (1.35), respectively, as functions of T_R. These estimated results are shown in figure 3.11. For the shot-noise-limit in equation (1.29), the signal-to-noise ratio R_{SN} was measured approximately at the level of 30,000 in our setup [103]. For the detection noise in equation (1.35), S_{RIN}^{det} was obtained from the RIN measured data shown in figure 3.31. The atomic quality factor Q_a was calculated from equation (1.30). In our calculations, we used the contrast and linewidth of the Ramsey central fringe, C and $\Delta\nu_{1/2}$ respectively, shown in figure 3.10. In our estimations, we considered that the durations of the optical pumping, microwave interrogation and optical detection pulses were constant and the Ramsey time varied. Therefore, the cycle time was equal to $T_C = T_R + 1.9$ ms.

Figure 3.11 shows that, the lowest shot-noise-limit was approximately at the level of $1.5 \times 10^{-14}\,\tau^{-1/2}$ and the minimum detection noise limit was approximately at the level of $2 \times 10^{-13}\,\tau^{-1/2}$. In addition, it is also seen that the minimum shot-noise happened when T_R was between 3 ms and 4 ms. This observation for T_R is in agreement with the obtained coherence relaxation time $T_2 \approx 4$ ms (see chapter 4). However, for the detection noise it is not the case and its minimum occurred when T_R was between 2 ms and 3 ms due to the RIN of the laser. Because the induced instability from the detection noise was about one order of magnitude higher than that of the shot-noise limit, we expect that the measured short-term stability of our Rb clock meets its lowest value at $2 < T_R < 3$ ms. Therefore, in addition to $\sigma_y^{SN}(\tau)$ and $\sigma_y^{det}(\tau)$ estimations, we measured the short-term stability $\sigma_y(\tau)$ in our Rb clock operating in the Ramsey-DR scheme at various Ramsey times T_R. The measurement results are also shown in figure 3.11. These measurements were done under experimental conditions presented in table 3.1. Therefore, the cycle time was equal to $T_C = T_R + 1.9$ ms (same to the one in above estimations). Figure 3.11 illustrates

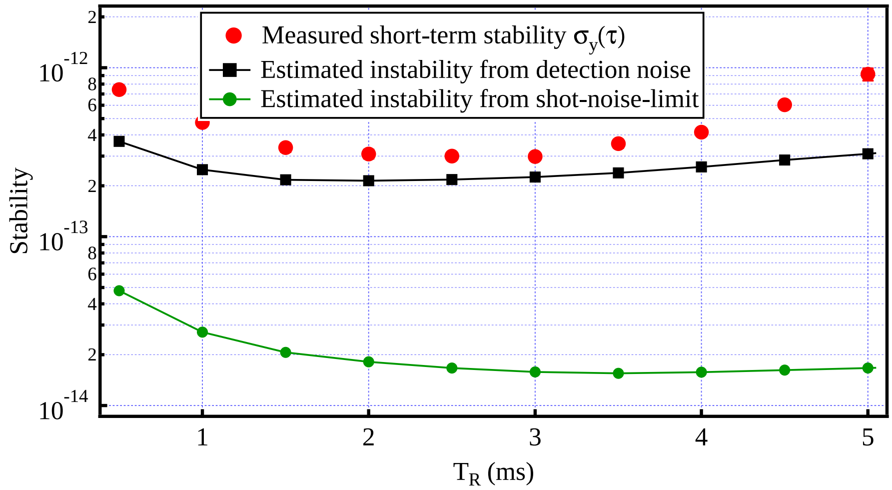

Figure 3.11: Short-term stability as a function of Ramsey time. Green circle: Estimated instability from the shot-noise-limit $\sigma_y^{SN}(\tau)$ (equation (1.29)) as a function of T_R. Black square: Estimated instability from the detection noise during the detection phase $\sigma_y^{det}(\tau)$ (equation (1.35)) as a function of T_R. Red circle: Measured short-term stability $\sigma_y(\tau)$ at different T_R and experimental conditions presented in table 3.1.

the lowest[1] measured short-term stability was obtained approximately at the level of $3 \times 10^{-13}\,\tau^{-1/2}$ when T_R was between 2 ms and 3 ms which was in agreement with our expectation. In figure 3.11, the difference between the measured short-term stability and the estimated $\sigma_y^{det}(\tau)$ data (i.e. the red circles and black squares) is slightly less than 1×10^{-13} (when $T_R \approx 3$ ms) which can be explained by the induced instabilities via the Dick effect. This observation in this figure is in good agreement with the estimated $\sigma_y^{LO}(\tau) \approx 7.5 \times 10^{-14}\,\tau^{-1/2}$ presented in section 1.7.2.2. Figure 3.12 shows a typical measured short-term stability performance when the Ramsey time was at $T_R = 3$ ms.

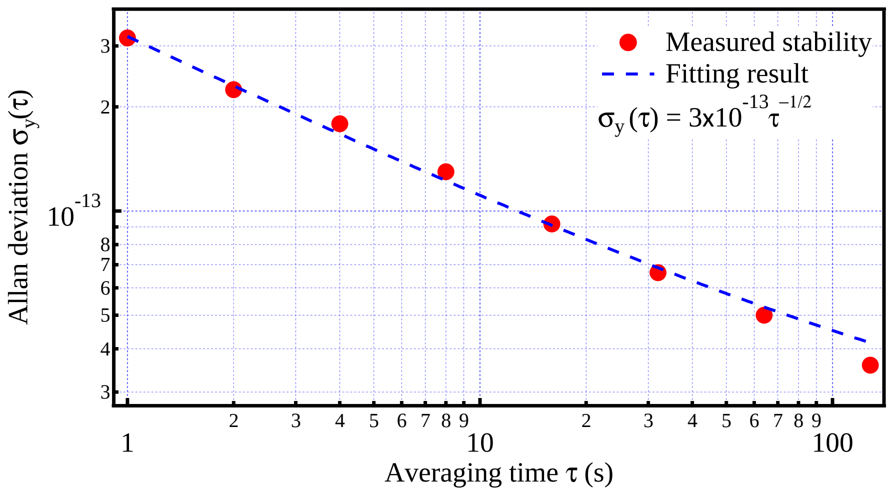

Figure 3.12: Typical measured short-term stability performance in our Ramsey-DR Rb clock when $T_R = 3$ ms.

3.2.1 Optimized Parameters Involved in the Ramsey-DR Scheme

Table 3.1 lists the optimized durations and input powers for three phases of optical pumping, microwave interrogation and optical detection in our Rb atomic clock operating in the Ramsey-DR scheme

[1] This was lowest stability for the setup and settings considered at the time of the study, as the very best short-term stability measured was $2.4 \times 10^{-13}\,\tau^{-1/2}$ (see figure 3.32).

based on the measurement results presented in previous sections.

Table 3.1: Optimized durations and input powers for three phases of optical pumping, microwave interrogation and optical detection in our Rb atomic clock.

Ramsey-DR sequence	Duration (ms)	Input power (mW)
Optical pumping	$t_p = 0.4$	$P_p = 13$
Rabi pulse	$\tau_m = 0.4$	$P_{\mu w} = 5.9 \times 10^{-3}$
Optical detection	$t_d = 0.7$	$P_d = 0.125$
Ramsey time	$T_R = 3.0$	—

3.3 Microwave Field Uniformity in the Cavity

The distribution of a microwave magnetic field inside a microwave cavity plays an important role in the performance of vapor cell atomic clocks, particularly for a clock operating in a pulsed regime such as the Ramsey-DR scheme [83]. The homogeneity of the microwave magnetic field over the volume occupied by the atoms inside the cavity is crucial for the clock signal and consequently for the clock performance. We evaluated the uniformity of the microwave field inside the microwave cavity which was used and presented in [41]. This microwave cavity is very similar to the microwave cavity used in our Rb atomic clock (see section 2.3.2). These investigations have been published in [103].

The cavities are often characterized by an electromagnetic field distribution at the center of the cavity where the vapor cell is usually placed. As mentioned previously (see section 2.3.2), our atomic clock used a cylindrical magnetron-type microwave cavity in a TE_{011}-like mode. Due to the spatial inhomogeneity of the microwave magnetic field inside the cavity and the vapor cell, different Rb atoms may experience various microwave pulse areas and not the exact $\pi/2$ microwave pulse. This effect results in a reduced clock signal contrast, consequently degrading the clock's short-term stability. We used Rabi oscillations to evaluate the microwave magnetic field uniformity inside the cavity. Here, we analyze Rabi oscillations in terms of change in optical absorption R induced by the microwave pulse area when the microwave frequency is set to the center of the clock transition. The normalized change in optical absorption is defined by:

$$R = 1 - \frac{I_t}{I_0}, \tag{3.2}$$

where I_t and I_0 are the transmitted light intensities for microwave pulse areas of θ and $\theta_0 = 0$, respectively. We simulated Ramsey signal numerically by considering $H_z(r, z)$, the z component of the microwave magnetic field inside the microwave cavity. $H_z(r, z)$ is parallel to the quantization axis in the physics package and is responsible for the π transition (including the clock transition). This simulation was conducted by on integrating the solution of the Ramsey fringes shape presented in [102] over the vapor cell. The calculation was adapted to our experimental conditions, such as the amplitudes of the optical and microwave pulses, population and coherence relaxation times and dimensions of the vapor cell. In our simulations, we considered two cases for the $H_z(r, z)$ field distributions. In the first case, we assumed that $H_z(r, z) = H_0$ is completely homogeneous and constant across the microwave cavity which is the ideal case; in the second case, we considered that $H_z(r, z)$ is distributed across the cavity based on a quasi TE_{011}-type field. The quasi TE_{011}-type field distribution in a cylindrical microwave cavity is expressed by [51]:

$$H_z(r,z) = H_0 J_0(3.832 \cdot \frac{r}{R_{cell}}) \sin\left(\frac{\pi z}{L_{cav}}\right), \qquad 0 \leqslant r \leqslant R_{cell}, \qquad 0 \leqslant z \leqslant L_{cav}, \tag{3.3}$$

where H_0 is the microwave magnetic field amplitude, R_{cell} is the vapor cell radius, L_{cav} is the length of the cavity and J_0 is the zero-order Bessel function.

Figure 3.13 shows the obtained experimental Ramsey pattern using the magnetron-type cavity and the two simulated Ramsey patterns for the ideal field and quasi TE_{011}-type field obtained from these simulations with black and blue solid lines, respectively. All three Ramsey signals were obtained when $T_R = 3$ ms and $\tau_m = 0.4$ ms, and the microwave pulse areas were $\pi/2$. Ramsey central fringes for the three case are shown in the inset of figure 3.13. For the ideal microwave field, the central Ramsey fringe contrast reached up to approximately 50%, while for the quasi TE_{011}-type microwave field, the contrast was approximately 35%, which was slightly lower than our measurements. The linewidths of the Ramsey central fringes in three cases were approximately 160±2 Hz.

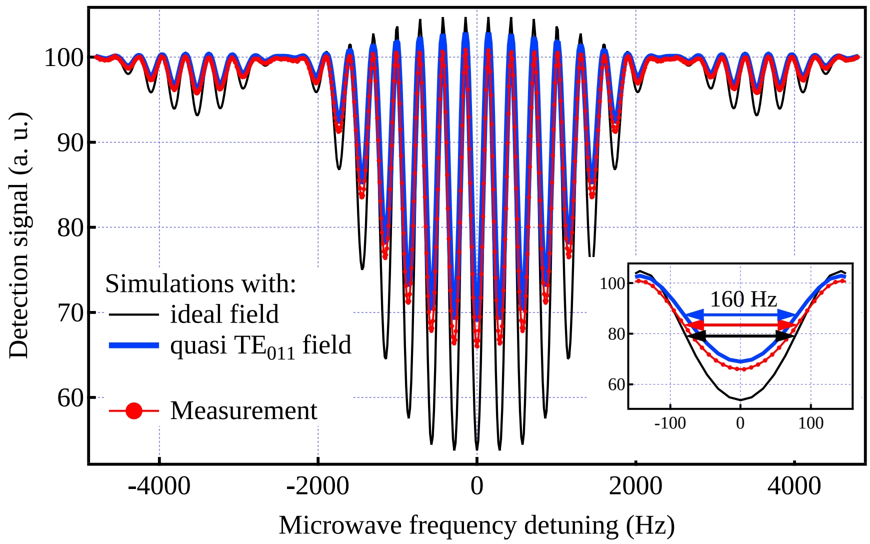

Figure 3.13: Simulation results for a hypothetical ideal (solid blue line) and TE_{011}-type (dash red line) microwave magnetic fields when, $T_R = 3$ ms and $\tau_m = 0.4$ ms and the microwave pulses are the $\pi/2$ pulses. Inset: Central Ramsey fringes. The figure is taken from [103].

For both field distributions, we simulated Rabi oscillations by varying the microwave field amplitude and maintaining a microwave pulse duration at $\tau_m = 0.4$ ms. Figure 3.14 shows the simulation results of Rabi oscillations for both microwave field distributions. In the case of the ideal field distribution, as expected, the Rabi simulation showed an undamped oscillations, and each extremum position occurred at $\theta = n \cdot \pi/2$ pulse area, where n is an integer number. In the case of quasi TE_{011}-type field distribution, the first maximum at $\theta = \pi/2$ had a smaller magnitude than that of the ideal field and this magnitude decayed in the next peaks. For the quasi TE_{011}-type Rabi oscillations, the extremum positions –from the second one– did not occur at $\theta = n \cdot \pi/2$. These effects likely occur due to residual $H_z(r,z)$ inhomogeneity, which causes various atoms in the cavity to experience a range of microwave-pulse areas. For a convenient comparison, the Rabi oscillations obtained from these experiments are shown in figure 3.14. The amplitudes of Rabi oscillations obtained experimentally in our magnetron-type cavity were not as high as those in the ideal field distributions but higher than those in the quasi TE_{011}-type field distribution. In addition, the damping rate as function of the microwave pulse area in the experimental Rabi oscillations was less than that in the quasi TE_{011}-type field. Therefore, based on the comparison of the simulations and experiments, we concluded that our magnetron-type cavity has a more uniform $H_z(r,z)$ distribution than that in a quasi TE_{011}-type field [103].

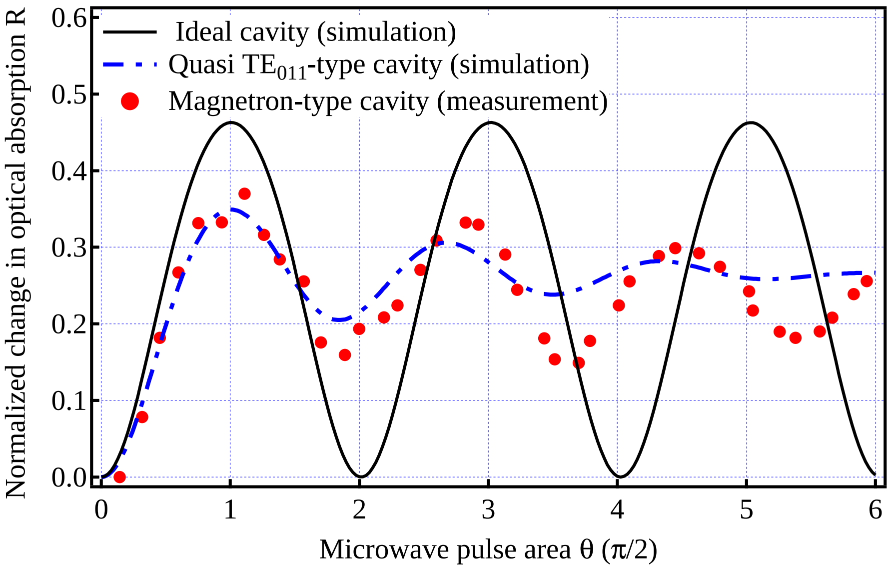

Figure 3.14: Rabi oscillations from: Simulated ideal (black solid line), quasi TE_{011}-type (blue dash line) microwave magnetic field distribution and measurements (red circle).

3.4 Vapor Cell and Stem Temperature Coefficients

We measured the temperature/pressure shift coefficients, β, δ and γ (see equation (1.43)), for the vapor cell used in our Rb clock. Figure 3.15 shows the clock's frequency shift –from the frequency of the clock transition of an unperturbed Rb atom– as a function of the cell temperature when stem temperature was fixed at $T_{stem} = 55\,°\mathrm{C}$. We obtained the inversion temperature of $T_{inv} = 63.22 \pm 0.05\,°\mathrm{C}$ with a quadratic fitting function like equation 1.43 applied to the data shown in figure 3.15 when T_0 =60°C. For a fixed stem temperature, the cell temperature coefficient of $TC_{cell} = 2.2(3) \times 10^{-12}/\mathrm{K}$ is determined from the local slope at the T_{inv}. Moreover, from the quadratic fit parameters, we obtained the β, δ and γ coefficients (equation (1.43)) for our vapor cell, where the Ar/N_2 buffer-gas mixture had a pressure ratio of $r = \frac{P_{Ar}}{P_{N_2}} = 1.6$ and a total pressure of 25 Torr. These measurement results are listed in table 3.2 together with the theoretically estimated values based on the theory and literature values from table 1.5. A good agreement exist between the estimated and the measured values of β and γ coefficients; however, this is not the case for the δ coefficient. This discrepancy is likely due to the estimation based on a standard vapor temperature of T_0 =60°C. From table 3.2, we calculated the clock frequency shift induced by the buffer gases using equation (1.43) at the level of approximately $\Delta\nu_{BG} \approx 4255\,\mathrm{Hz}$. In our Rb clock, the cell-TC was measured at the same level for the previous vapor cell design at the LTF presented by Bandi et al. in [35, 41]. The clock instabilities induced by the cell temperature fluctuations of about 3.5 mK [35], is at the level of approximately 7.7×10^{-15} up to $\tau = 10^4$ s.

It was mentioned in section 2.3.1 that for the vapor cell used in this work, a reduced ETS effect [94]

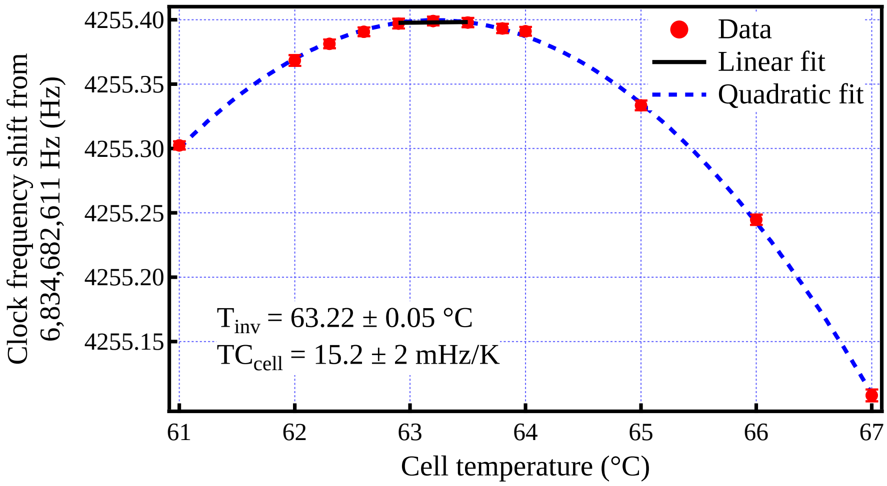

Figure 3.15: Clock frequency shift as a function of the vapor cell temperature when the stem temperature is fixed at $T_{stm} = 55\,°\mathrm{C}$. The inversion temperature $T_{inv} = 63.22 \pm 0.05\,°\mathrm{C}$ is obtained from equation (1.45) with a quadratic fit to the data points when T_0 =60°C.

Table 3.2: Measured (from figure 3.15) and estimated (from table 1.5) temperature/pressure coefficients for a mixture of Ar and N_2 with a pressure ratio of $r = P_{Ar}/P_{N_2} = 1.6$ with a total pressure of 25 Torr in our vapor cell and T_0 =60°C.

	β (Hz Torr^{-1})	δ (Hz Torr^{-1} K^{-1})	γ (Hz Torr^{-1} K^{-2})
Measurements	$170.2 \pm 9.3 \times 10^{-5}$	$5.1 \times 10^{-3} \pm 4 \times 10^{-5}$	$-0.8 \times 10^{-3} \pm 4.7 \times 10^{-6}$
Estimations (table 1.5)	173.6	1.46×10^{-2}	-0.8×10^{-3}

was achieved by strongly reducing the relative volume of the cell-stem and we estimated the relative stem-TC at the level of $TC_{stem} \approx 1 \times 10^{-12}$/K for our vapor cell. Here, we present the measurement of this quantity experimentally. Figure 3.16 shows the measured clock frequency shift as a function of the stem temperature when the cell temperature was fixed at $T_{cell} = 65\,°\mathrm{C}$. The stem-TC was measured at $1.07(8) \times 10^{-12}$/K from a linear fit to the measured data. This result is in agreement with our estimation. The obtained stem-TC for our vapor cell with a smaller stem volume was about one order of magnitude lower than $TC_{stem} = 1.2 \times 10^{-11}$/K for the previously developed vapor cell at the LTF with a larger stem volume presented in [41] and about two orders of magnitude lower than of the one used in Calosso et al. ($\approx 1.5 \times 10^{-10}$/K [94]). Therefore for our Ramsey-DR Rb clock, we estimate the induced clock instabilities by the stem temperature fluctuations at the level of approximately 5×10^{-15} up to $\tau = 10^4$ s for stem temperature variations of about 5 mK [35].

3.5 Light Shifts

Light Shifts (LS) or AC-Stark Shift is one of the main sources of instability in atomic frequency standards. As mentioned in section 1.5, in the Ramsey-DR scheme, the atoms are interrogated in absence of the light with a couple of resonant microwave pulses that are separated by a Ramsey time T_R. In principle, this separation results in a significant LS reduction using the Ramsey-DR scheme compared to the continuous-wave double-resonance (CW-DR) scheme.

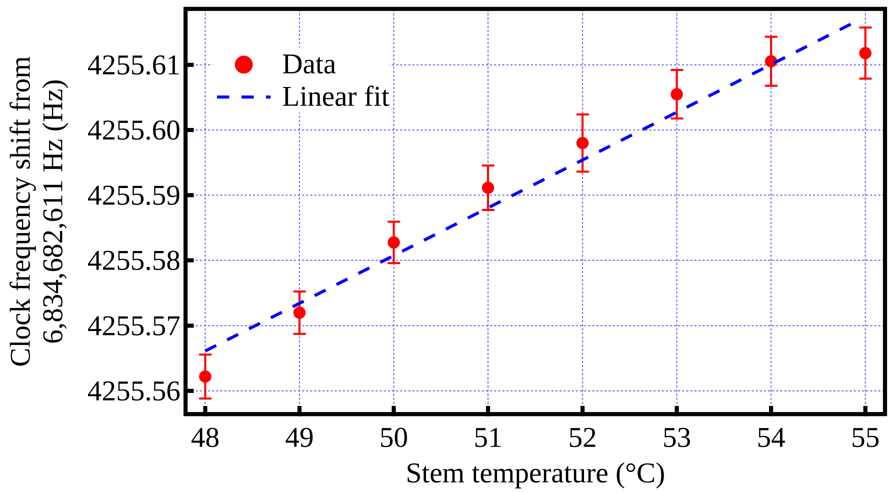

Figure 3.16: Clock frequency shift as a function of the stem temperature when the cell temperature is fixed at $T_{cell} = 65\,^{\circ}\mathrm{C}$.

In this section, first we measure the intensity and frequency LS coefficients α_{LS} and β_{LS} respectively, when the clock operates in the CW-DR scheme and in the Ramsey-DR scheme. Then, we present a model based on the LS measurements and the LS theory for the CW-DR scheme to estimate the various α_{LS} in the Ramsey-DR scheme when the laser frequency is stabilized to different sub-Doppler transition frequencies of D2 line of ^{87}Rb. Finally, we compare the results from the estimated α_{LS} and measured α_{LS} in the Ramsey-DR scheme.

The α_{LS} coefficient was calculated using equation (1.55), by measuring the clock frequency shift when the laser input power to the cavity was varied at a fixed laser frequency. For the measurements presented in this section, an optical polarizer was used in front of the entrance to the cavity to vary the laser input power to the cavity (see figure 3.17). Therefore, rotating the polarizer resulted in varying laser intensity during the entire sequences of the Ramsey-DR scheme. The polarizer did not change the ratio between laser input powers during optical pumping and optical detection pulses.

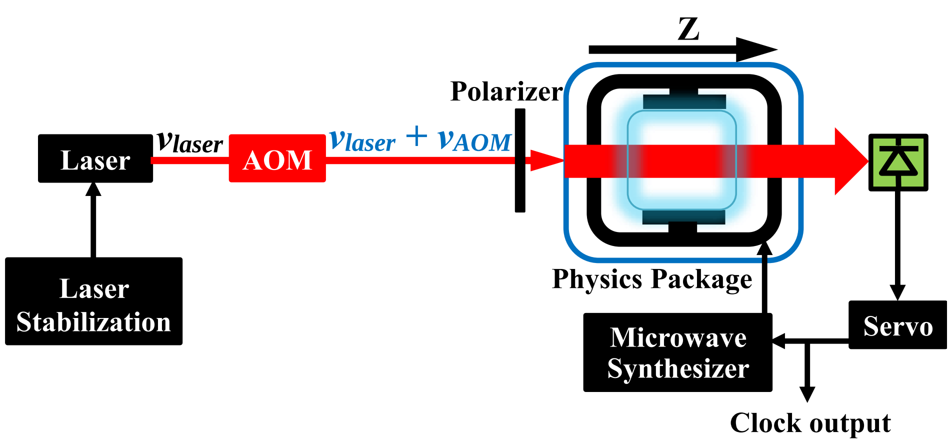

Figure 3.17: Simplified schematics of the clock setup. Laser has the frequency of ν_{laser} before the AOM. The light enters the cavity with frequency of $\nu_{laser} + \nu_{AOM}$ when the AOM is switched ON. When the AOM is switched OFF a residual light with a frequency of ν_{laser} enters the cavity.

3.5.1 α_{LS} and β_{LS} in Ramsey-DR Scheme vs CW-DR Scheme

Here, we measured and compared the LS coefficients α_{LS} and β_{LS} for our Rb atomic clock operating in Ramsey-DR and CW-DR schemes.

The clock frequency was recorded in our Rb atomic clock operating in the Ramsey-DR scheme when laser input power to the cavity during optical pumping and optical detection sequences were 12.3 mW and 110 μW, respectively. The laser frequency was stabilized to the sub-Doppler cross-over transition CO11-12 frequency (see figure 2.10) then shifted by -160 MHz using the AOM integrated in the LH (see section 2.3). The $\pi/2$ microwave pulses had a power of 5.9 μW and a duration of $\tau_m = 0.4$ ms, and the Ramsey time was set to $T_R = 3$ ms. This measurement was repeated for various laser input powers to the cavity. Figure 3.18 shows the clock frequency as a function of laser input power to the cavity during the optical pumping sequence (upper horizontal axis) in the Ramsey-DR scheme. The lower axis shows the normalized laser input power with respect to the nominal working point of optical pumping power (i.e., 12.3 mW). Using equation (1.55) and a linear fit to the data in figure 3.18, we calculated the intensity LS coefficient of $\alpha_{LS} = -6.6\,(5) \times 10^{-14}/\%$.

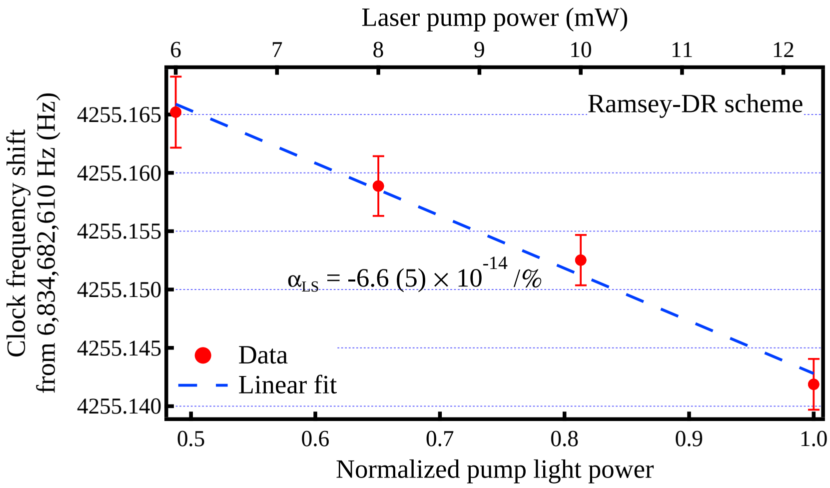

Figure 3.18: Clock frequency shift as a function of laser pump input power to the cavity in the case of Ramsey-DR scheme. The laser is stabilized to the sub-Doppler CO11-12 transition.

With the clock operating in the Ramsey-DR scheme, the frequency LS coefficient β_{LS} was measured with the laser input power to the cavity fixed at 12.3 mW and 110 μW for the optical pumping and detection, respectively, and the frequency of the laser detuned near the working point. This measurement was completed by varying the RF frequency feeding the AOM of the laser source. Figure 3.19 shows the clock frequency as a function of the laser frequency detuning. Using this measurement and equation (1.56), we deduced the frequency LS coefficient at $\beta_{LS} = -7.9\,(3) \times 10^{-14}/\mathrm{MHz}$.

In the same Rb atomic clock, α_{LS} and β_{LS} were also measured in the CW-DR scheme using the same procedure explained above. A detailed procedure for operating the Rb atomic clock in the CW-DR scheme was presented with optimized parameters in [41]. Briefly, for these measurements, we operated the clock in the CW-DR scheme when the laser was stabilized to the sub-Doppler cross-over transition CO11-12 (same as the LS measurements in the Ramsey-DR scheme) with an input power of 125 μW and an injected microwave power to the cavity of 0.45 μW. Figures 3.20 and 3.21 show the clock frequency as a function of the laser input power to the cavity and the laser frequency detuning, respectively. In the case of the CW-DR scheme, the LS coefficients of $\alpha_{LS} = +3.5\,(4) \times 10^{-13}/\%$

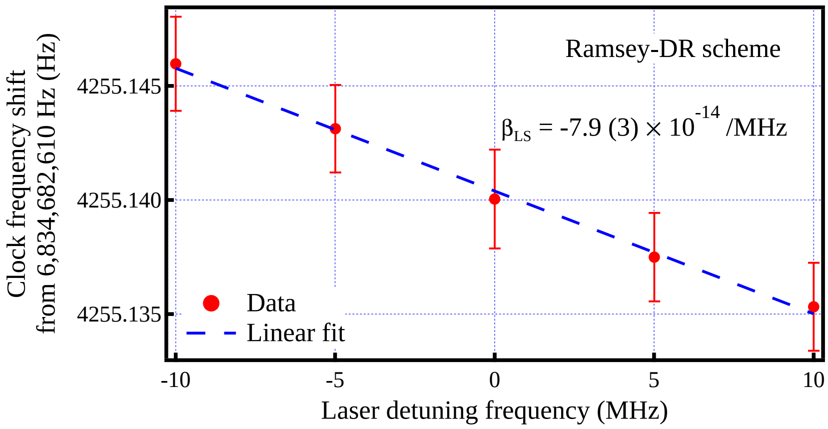

Figure 3.19: Clock frequency shift as a function of laser frequency detuning in the case of Ramsey-DR scheme. The laser is stabilized to the sub-Doppler CO11-12 transition.

and $\beta_{LS} = -1.0\,(1) \times 10^{-11}$/MHz were obtained. Bandi et al. reported $\alpha_{LS} \approx 8 \times 10^{-13}/\%$ and $\beta_{LS} \approx 1.0\,(1) \times 10^{-11}$/MHz for their Rb clock operating in the CW-DR scheme using a similar physics package and a different laser system with the AOM [35].

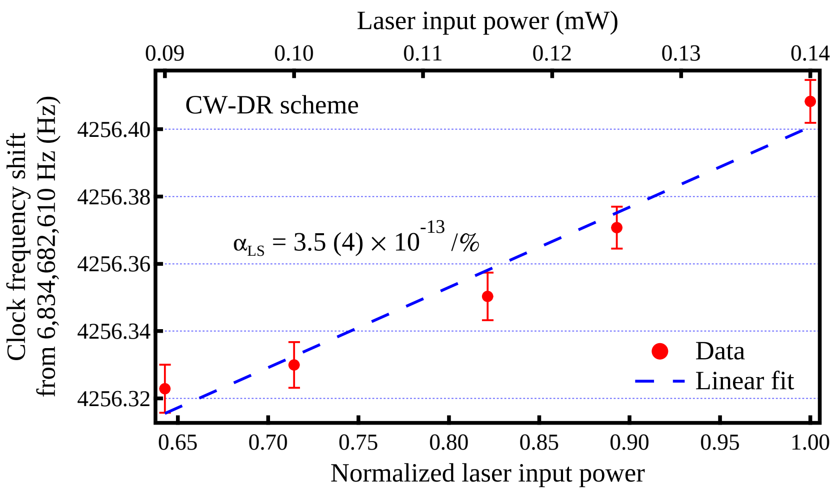

Figure 3.20: Clock frequency shift as a function of laser input power to the cavity in the case of CW-DR scheme. The laser is stabilized to the sub-Doppler CO11-12 transition.

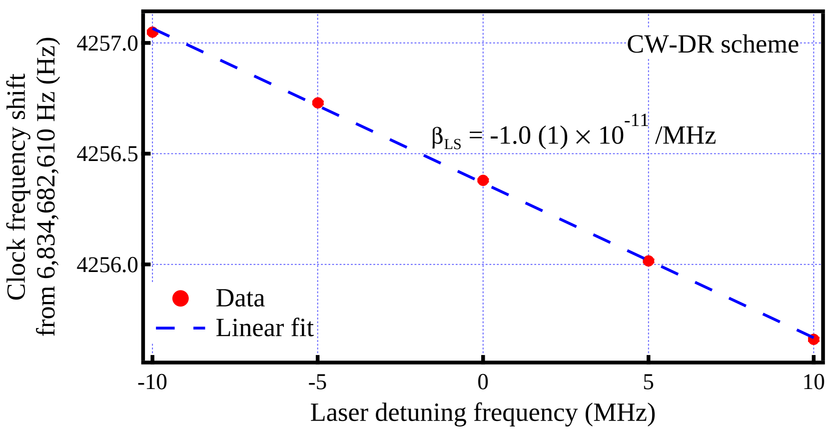

Figure 3.21: Clock frequency shift as a function of laser frequency detuning in the case of CW-DR scheme. The laser is stabilized to the sub-Doppler CO11-12 transition.

Table 3.3 lists the obtained LS coefficients for our Rb atomic clock operating in both Ramsey-DR and CW-DR schemes. The Ramsey-DR scheme resulted in a β_{LS} more than two orders of magnitudes lower than the CW-DR scheme. However, contrary to our expectations, α_{LS} in the Ramsey-DR scheme was not completely suppressed and only five times lower than that in the CW-DR scheme. In addition, notably, the measured α_{LS} for the two schemes had opposite signs. Both of these observations, the non-zero α_{LS} in the Ramsey-DR scheme and the opposite signs of α_{LS} in the Ramsey-DR and CW-DR schemes, suggest the presence of some residual light in the vapor cell when the AOM was off (i.e., during the microwave pulses and the Ramsey time T_R). In the next sections, we discuss and verify the possible sources of these observations.

Table 3.3: Measured light shift coefficients α_{LS} and β_{LS} for the Rb clock operating in Ramsey-DR and CW-DR schemes. The laser is stabilized to the sub-Doppler cross-over CO11-12 transition.

	Ramsey-DR	CW-DR	ratio: $\frac{\text{CW-DR}}{\text{Ramsey-DR}}$
α_{LS} (/%)	$-6.6\,(5)\times 10^{-14}$	$+3.5\,(4)\times 10^{-13}$	≈ -5
β_{LS} (/MHz)	$-7.9\,(3)\times 10^{-14}$	$-1.0\,(1)\times 10^{-11}$	≈ 125

3.5.2 α_{LS} and Gap Times Between Pulses in the Ramsey-DR Scheme

Here, we investigated the effect of the gap times between the pulses on the intensity LS coefficient α_{LS}. Figure 3.22 shows the Ramsey-DR scheme where, G_1 is the gap time between the optical pumping and the first microwave pulse, and G_2 is the gap time between the second microwave pulse and the optical detection pulse. Nominally in our measurements, G_1 and G_2 were set to 10 μs and 20 μs, respectively, which were longer than the AOM rise/fall time ($\approx$4.5 μs, see section 2.2.1).

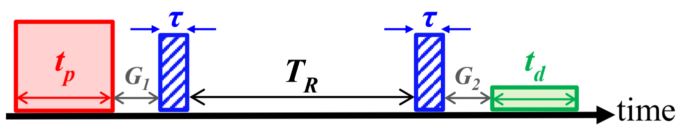

Figure 3.22: Timing sequence of the Ramsey-DR scheme including the gap times G_1 and G_2.

Figure 3.23 shows the obtained α_{LS} for four various G_1 and G_2 durations. In addition, it shows the obtained α_{LS} for the nominal working point, where G_1 and G_2 are 10 μs and 20 μs, respectively. The laser frequency is stabilized to the sub-Doppler cross-over transition CO10-12 and the direct transition 23 frequencies. From figure 3.23, we concluded that the gap times do not significantly influence the α_{LS}.

3.5.3 LS Model From CW-DR Scheme

In principle, an ideal AOM does not allow light to pass when it is switched off. However, in our laser system (see section 2.2), the optical switching by the AOM is not perfect. We measured a residual light with a power of 0.6 μW (comparing to the maximum 13 mW laser pump power) entering the physics package when the AOM was switched off. Due to the design of the LH, the frequency of this residual light was not shifted by the AOM and was equal to the frequency of the laser ν_{laser}. Therefore, when

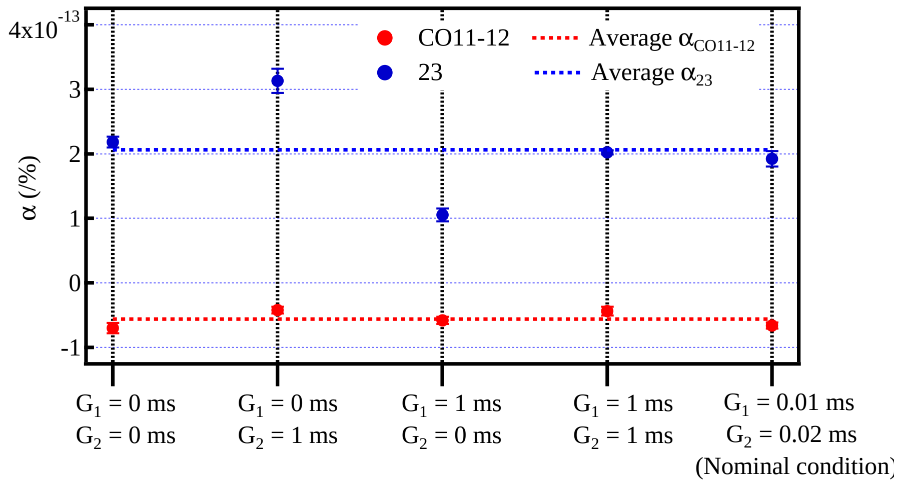

Figure 3.23: Measured α_{LS} in the Ramsey-DR scheme at various G_1 and G_2 gap times when the laser frequency is stabilized to the sub-Doppler cross-over transition CO10-12 (red solid circles) and the direct transition 23 (blue solid circles).

the clock operated in the Ramsey-DR scheme, this residual light with the frequency of ν_{laser} enters the vapor cell during Ramsey time T_R and microwave pulses and affects the LS results. We developed a preliminary model and investigated the impact of the residual light on α_{LS} in the Ramsey-DR scheme. We treated the LS induced by this residual light similar to the LS induced in the CW-DR scheme. However, for our measurements, the residual light in the Ramsey-DR scheme had the frequency of ν_{laser} (not shifted by the AOM) while in the CW-DR scheme the laser had a frequency of $\nu_{laser} + \nu_{AOM}$, where $\nu_{AOM} = -160\,\text{MHz}$ (see figure 3.17).

Previously, the intensity LS coefficient α_{LS} was measured for our Rb clock operating in the CW-DR scheme (see figure 3.20). Figure 3.24 shows the extrapolation of these measurements to zero laser input power. Hence, using the extrapolation, we can obtain the clock frequency shift at zero light of 4256.16 Hz, (primarily due to the presence of the buffer gases in the vapor cell, see section 1.7.3.2). The frequency difference between the clock frequency shift at the working point (i.e., when the laser input power is 125 μW) and the clock frequency shift at zero light was measured as: $\Delta\nu = 4256.37\,\text{Hz} - 4256.16\,\text{Hz} = 0.21$ Hz. Because in our calculations we used measurement results obtained from the CW-DR scheme, the frequency difference of 0.21 Hz is valid for a condition that the light frequency is $\nu_{laser} + \nu_{AOM}$.

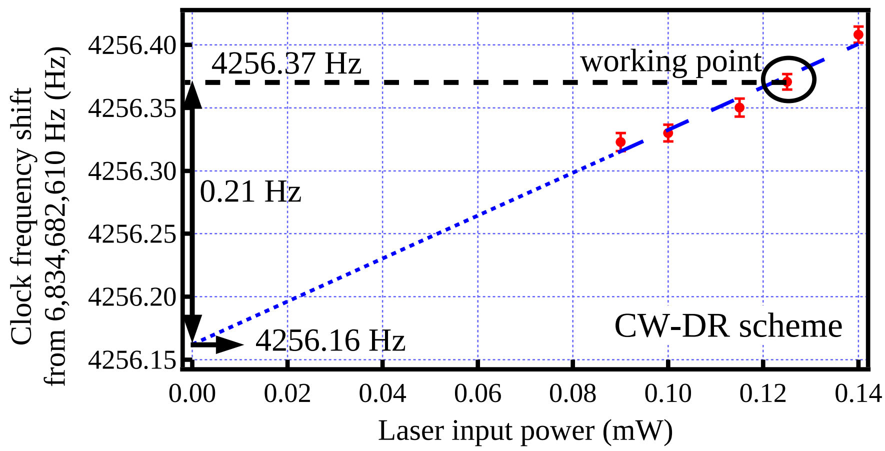

Figure 3.24: Extrapolation to zero laser input power to the cavity in the CW-DR scheme.

We used the measured frequency LS coefficient β_{LS} in the CW-DR scheme (i.e., figure 3.21) and developed our model to estimate the frequency difference when the laser frequency is not shifted by the AOM and is equal to the frequency of ν_{laser}. The model shown in figure 3.25 is based on the LS measurements in the CW-DR scheme. In figure 3.25, the y-axis is the clock frequency shift induced by the laser with the power of 125 μW and the x-axis is the frequency detuning of the laser from 384.228 115 THz (D2 line ^{87}Rb: $F_g = 2 \rightarrow F_e = 3$). Here, we assume that the zero intensity LS occurs at zero clock frequency shift (which corresponds to 4256.16 Hz in figure 3.24). The blue diamond represents the working point in the CW-DR scheme (same as in figure 3.24) where the light has the frequency of $\nu_{laser} + \nu_{AOM}$ and a power of 125 μW. For this point, the clock frequency difference from the zero LS was calculated as +0.21 Hz (figure 3.24). We used this frequency difference and the frequency LS coefficient $\beta_{LS} = -7.0 \times 10^{-8}$ Hz/Hz (figure 3.21) to calculate the frequency difference when the light is not shifted −160 MHz by the AOM (equivalent to the condition in the Ramsey-DR scheme induced by the residual light). This condition is denoted by a black circle on the graph in figure 3.25. By using the $\beta_{LS} = -7 \times 10^{-8}$ Hz/Hz coefficient and the AOM frequency $\nu_{AOM} = 160$ MHz, we estimated the frequency difference between the black circle point and the zero LS was equal to −11 Hz. This estimation was based on the condition of the laser power at 125 μW.

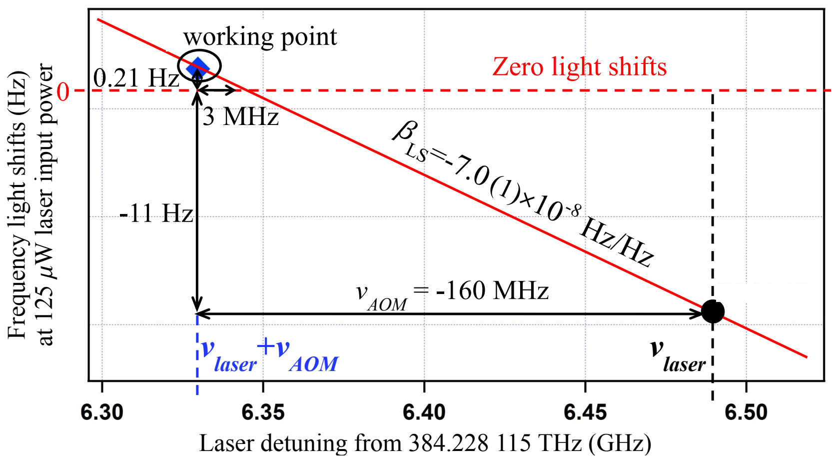

Figure 3.25: Preliminary LS model based on the measured α_{LS} and β_{LS} in the CW-DR scheme when the laser frequency was stabilized to the sub-Doppler CO11-12 transition frequency (figures 3.21 and 3.24) to estimate α_{LS} in the Ramsey-DR scheme for the same laser locking (CO11-12).

As mentioned previously, the residual light with a power of 0.6 μW passed through the vapor cell when the AOM was switched off (during T_R in the Ramsey-DR scheme). The power of this residual light is 210 times lower than the laser input power to the cavity in the LS measurements in CW-DR scheme (i.e., 125 μW). Therefore, by using our model presented in figure 3.25, we estimated the clock frequency shift induced by the residual light in the Ramsey-DR scheme to be $\frac{-11\,\text{Hz}}{210} = -0.052$ Hz, which corresponds to an intensity LS of $\alpha_{LS} \approx 7.7 \times 10^{-14}/\%$. This estimated α_{LS} from the LS model was in good agreement with the measured α_{LS} in the Ramsey-DR scheme shown in figure 3.18 and in table 3.3 (i.e., $-6.6(5) \times 10^{-14}/\%$). At zero light, the ratio of the frequency difference in the CW-DR scheme to frequency difference at in the Ramsey-DR scheme was calculated to be $\frac{0.21\,\text{Hz}}{-0.052\,\text{Hz}} \approx -4$. This ratio explains the difference in intensity LS coefficients in CW-DR and Ramsey-DR schemes presented in section 3.5.1 and table 3.3.

3.5.4 Generalizing the LS Model in the Ramsey-DR Scheme

In the previous section, we presented an LS model based on LS measurements in the CW-DR scheme and estimated the α_{LS} in the Ramsey-DR scheme for a particular condition when the laser frequency was stabilized to the sub-Doppler CO11-12 transition frequency. In this section we generalize our presented model to estimate the intensity LS coefficients α_{LS} in the Ramsey-DR scheme when the laser is stabilized to other sub Doppler transitions in the D2 line of ^{87}Rb. For this work, we used the LS theory and simulations presented in [87] for the CW-DR scheme. We adjusted the cell parameters in the model to those applying in the experimental clock realization and obtained the theoretical α_{LS} as a function of the laser frequency. Because the success of the CW-DR model for explaining the α_{LS} in section 3.5.3 motivated us to extend this model to the other optical frequencies. We note that, the frequency of this residual light during the Ramse time was not shifted by the AOM (due to the design of the LH).

The lower graph in figure 3.26 shows the theoretical α_{LS} curve (obtained from the simulations) as a function of the laser frequency detuning in the CW-DR scheme when the laser frequency is not shifted by AOM (i.e., light frequency is ν_{laser}) and the laser intensity is $1\,\mu\text{W/mm}^2$. Zero laser frequency detuning corresponded to the laser frequency of 384.228 115 GHz (D2 line ^{87}Rb: $F_g = 2 \rightarrow F_e = 3$). The upper graph in figure 3.26 shows the saturated absorption spectrum of the D2 line of ^{87}Rb where the peak from $F_g = 2 \rightarrow F_e = 3$ transition is fixed at zero laser frequency detuning. Using the saturated absorption and α_{LS} curves (figure 3.26), we obtained the theoretical α_{LS} for a Rb clock operating in the CW-DR scheme when the laser frequency was stabilized to various D2 line transitions of ^{87}Rb (ν_{laser}, without any frequency shift). The black circles on the α_{LS} curve denote this information (figure 3.26). In the case of CW-DR scheme without using AOM, the α_{LS} is positive if the laser frequency is stabilized to an $F_g = 2$ transition (and the α_{LS} is negative if the laser frequency is stabilized to an $F_g = 1$ transition). As previously mentioned, the condition of the CW-DR scheme without using AOM is similar to that of the Ramsey-DR scheme by residual light. Therefore in the case of the Ramsey-DR scheme, using this simulation, we predicted that the sign of α_{LS} is positive if the laser frequency is stabilized to an $F_g = 2$ transition (and is negative if the laser frequency is stabilized to an $F_g = 1$ transition). This prediction was confirmed by the measurements shown in figure 3.27 and table 3.4.

We estimated the α_{LS} in the Ramsey-DR scheme for various laser locking points from the presented LS model and the simulations, as presented in figures 3.25 and 3.26. For this work, we used the estimated clock frequency shift at zero light of $\Delta\nu_{LS}^{CO11-12} = 0.052\,\text{Hz}$ induced by the residual light in the Ramsey-DR scheme when the laser frequency was stabilized to the sub-Doppler transition CO11-12 (see section 3.5.3) and the LS simulations based on the CW-DR scheme. From the simulations, we calculated the $\alpha_{LS}^{CO11-12}$ for a laser input power of $0.6\,\mu$W. By knowing $\Delta\nu_{LS}^{CO11-12}$ and $\alpha_{LS}^{CO11-12}$, the laser intensity variation ΔI can be calculated from equation (1.55). We assumed ΔI was the same at the different laser locking points. Therefore, we estimated the clock frequency shift at zero light at different laser locking points from $\Delta\nu_{LS}^{n} = \alpha_{LS}^{n} \cdot \Delta I$, the α_{LS}^{n} is calculated from the simulations. The estimated α_{LS} in the Ramsey-DR scheme for various laser locking points are listed in table 3.4.

The blue diamond on the α_{LS} curve in figure 3.26 represents the intensity LS coefficient in the case of the CW-DR scheme when a laser frequency is stabilized to CO11-12 transition and is shifted by $-160\,$MHz. This α_{LS} (blue diamond) had a positive sign, which agrees with the measured α_{LS} in the CW-DR scheme (figure 3.20).

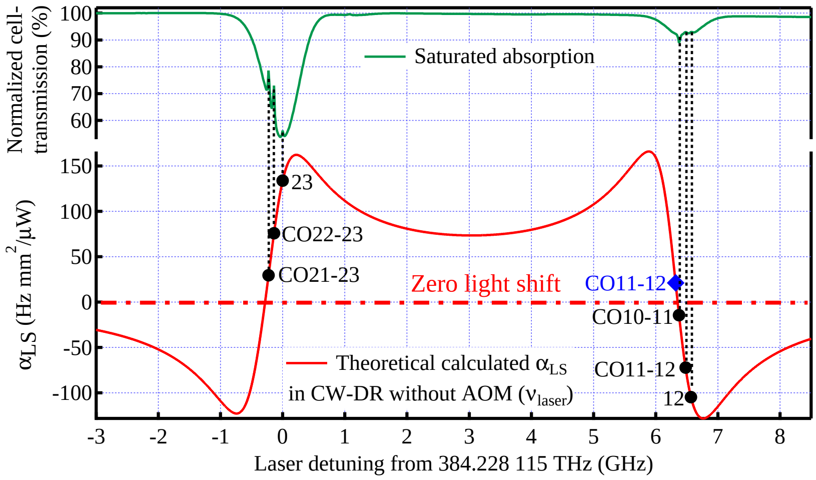

Figure 3.26: (Upper): Sub-Doppler absorption spectrum of the reference cell. (Lower): Theoretical frequency LS predictions in the D2 line of ^{87}Rb for a light intensity of 1 μW/mm^2 in the CW-DR scheme. Red solid line denotes the theoretical calculated intensity LS coefficient α_{LS} as a function of the laser frequency detuning in the CW-DR scheme based on simulations presented in [87]. The laser frequency was ν_{laser} and was not shifted by AOM. Black circles on the α_{LS} curve represent $\alpha_{LS}(\nu_{laser})$ for various laser locking points in the D2 line of ^{87}Rb. The blue diamond represents $\alpha_{LS}(\nu_{laser}^{CO11-12} + \nu_{AOM})$ for a laser whose frequency is stabilized to CO11-12 transition frequency, where $\nu_{AOM} = -160$ MHz.

3.5.5 α_{LS} Coefficients in the Ramsey-DR Scheme

In order to validate our preliminary model presented in section 3.5.4, we measured α_{LS} in our Rb clock operating in the Ramsey-DR scheme when the laser frequency was stabilized to different sub-Doppler transitions in the D2 line of ^{87}Rb. We operated our Rb clock in the Ramsey-DR scheme with the following conditions: $t_p = 0.4$ ms, $\tau_m = 0.4$ ms, $T_R = 3$ ms, $t_d = 0.7$ ms and the microwave pulse input power to the cavity of 5.9 μW. An optical polarizer was used in front of the physics package to vary the laser input power to the cavity (see figure 3.17). Therefore, rotating the optical polarizer results in varied light intensity in the whole sequences of the Ramsey-DR scheme. The laser input pumping power to the cavity varied from 6 mW to approximately 12-13 mW (depending on the laser locking point). Simultaneously, the optical detection power varied approximately from 50 μW to 120 μW. The clock frequency was measured when the laser frequency was stabilized to frequencies of six sub-Doppler transitions in the D2 line of ^{87}Rb, namely CO21-23, CO22-23, $F = 23$, CO10-11, CO11-12 and $F = 12$ (see figure 2.10) and shifted -160 MHz by the AOM integrated in the LH (see section 2.2). The result of these measurements are shown in figure 3.27.

Figure 3.27 shows the recorded clock frequencies as a function of laser input power to the cavity during the optical pumping pulse for various laser locking points. For each laser locking point, the α_{LS} was calculated from a linear fit to the data based on equation (1.55). Table 3.4 lists the α_{LS} obtained from the measurements shown in figure 3.27. Our expectation on the sign of estimated α_{LS} based on our model presented in section 3.5.4 fits very well with the measured α_{LS}. Moreover, the estimated absolute values for α_{LS} were in agreement with a factor of $0.4-2$ with the measured α_{LS} depending on the laser locking point.

Bandi et al. in [35] investigated the intensity LS in an Rb atomic clock operating in the CW-DR scheme using a similar physics package to ours but using a different laser system without any AOM

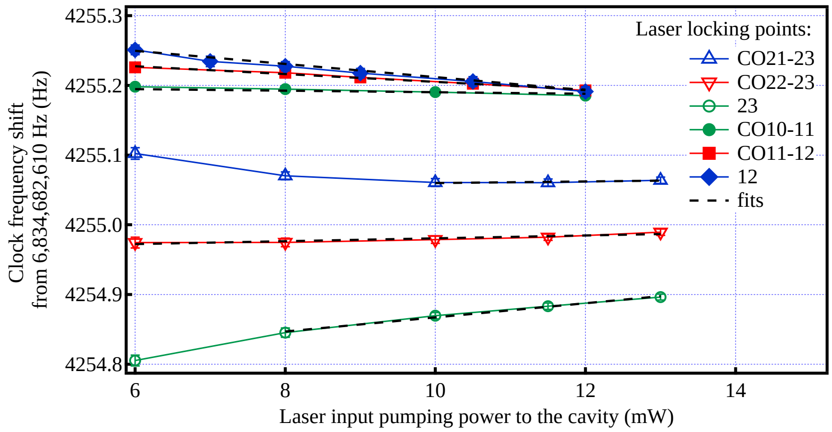

Figure 3.27: Clock frequency shift as a function of the laser input power to the cavity during the optical pumping pulse when the clock is operating in Ramsey-DR scheme. The frequency of the laser is stabilized to various ^{87}Rb sub-Doppler transition frequencies and shifted -160 MHz by the AOM. For each laser frequency the experimental α_{LS} is obtained by a linear fit to the data.

Table 3.4: Estimated and measured α_{LS} coefficient when the clock was operated in the Ramsey-DR scheme.

Laser locking point	Estimated $\alpha_{LS}\,(/\%)$	Measured $\alpha_{LS}\,(/\%)$
CO21-23	3.1×10^{-14}	$2.1\ (9)\times10^{-14}$
CO22-23	8.0×10^{-14}	$3.9\ (1)\times10^{-14}$
F=23	1.4×10^{-13}	$1.9\ (1)\times10^{-13}$
CO10-11	-1.5×10^{-14}	$-3.8\ (2)\times10^{-14}$
CO11-12	-7.7×10^{-14}	$-6.6\ (5)\times10^{-14}$
F=12	-1.1×10^{-13}	$-1.7\ (1)\times10^{-13}$

($\nu_{AOM} = 0$). This study is shown in figure 3.28 taken from [35]. It shows the relative clock frequency as a function of the laser intensity in their setup. We can see that the α_{LS} had a positive sign when the laser frequency was stabilized to an $F = 2$ transition and had a negative sign when laser frequency was stabilized to an $F = 1$ transition. This observation (the sign of α_{LS}) in the case of CW-DR scheme is in agreement with both our measured and estimated α_{LS} for the Ramsey-DR scheme (see table 3.4). Therefore, this agreement can validate our hypothesis that the sign of the α_{LS} in our Ramsay-DR clock is defined by the frequency of the residual light during the Ramsey time which is ν_{laser}.

In the same study [35], Bandi et al. reported an induced relative instability by the laser intensity fluctuations at the level of 9.9×10^{-15} for the medium- to long-term scale up to $\tau = 10^4$ s in their setup when the laser frequency ν_{Laser} was stabilized to CO10-11 transition and not shifted by any AOM ($\nu_{AOM} = 0$)[1]. For this estimation, they measured the relative laser intensity fluctuation at the level of 0.01% at $\tau = 10^4$ s [35]. In our Ramsey-DR Rb atomic clock using the integrated AOM laser system (see section 2.2), we estimated the induced instability from the laser intensity fluctuations approximately at the level of some 10^{-15} by knowing the measured α_{LS} from table 3.4 depending the laser locking

[1]Bandi et al. presented the lowest induced relative instability from the laser intensity fluctuations at the level of 6.9×10^{-16} for the medium- to long-term scale up to $\tau = 10^4$ s in their Rb atomic clock operating in the CW-DR scheme using an AOM-laser system [41].

point. In our estimation we used the relative laser intensity fluctuation at the level of 0.1% at $\tau = 10^4$ s (see figure 2.7).

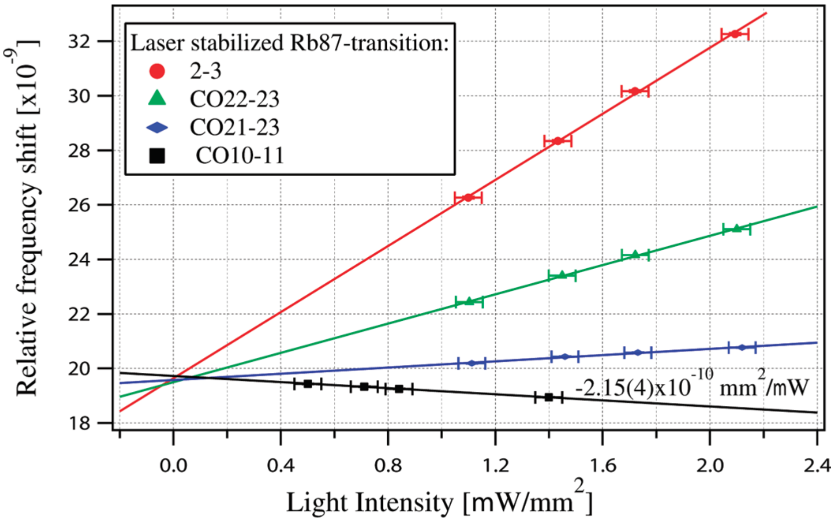

Figure 3.28: Intensity LS measurements by Bandi et al. when their Rb atomic clock was operated in the CW-DR scheme. In their study, they used a physics package similar to the one used in our work while a different laser system without any AOM was used. The figure is taken from [35].

Comparing the clock frequency sensitivity to the laser intensity between our Ramsey-DR and Bandi's CW-DR clocks, two different behaviors are visible (see figures 3.27 and 3.28). For the CW-DR Rb clock, extrapolating to zero light results in converging to zero LS, which it is not the case for the Ramsey-DR clock (non-converging behavior at zero light). The origin of this phenomena is still unknown and further analysis are required. A possible source for this phenomena can be the residual coherence effect due to the incomplete optical pumping in the case of the Ramsey-DR scheme [42]. As mentioned previously, we used a polarizer and varied the laser input power during the entire sequences of the Ramsey-DR scheme. Therefore, we cannot evaluate the dominant contribution of the LS in the Ramsey-DR sequences, even though the effect of the residual light in Ramsey time was evaluated. One direction for the further analysis is to investigate the LS in each sequence of the Ramsey-DR scheme independently.

3.5.6 β_{LS} coefficients in the Ramsey-DR Scheme

From data shown in figure 3.27, in addition to the intensity LS coefficient α_{LS}, we also measured the frequency LS β_{LS} globally for the conditions that the laser frequency was stabilized to $F = 1$ and $F = 2$ transitions. In the case of $F = 1$, the laser input power to the cavity was constant at 13 mW during the pumping and in the case of $F = 2$ the laser input power to the cavity was constant at 12 mW during the pumping. The measured β_{LS} coefficients are presented in table 3.5. We estimated a relative induced instability in the medium- to long-term scale up to $\tau = 10^4$ s approximately at the level of 10^{-16}. In our estimation we used the measured β_{LS} in table 3.5 and the laser frequency variations about 10 kHz at $\tau = 10^4$ (see figure 2.6).

Bandi et al. reported a frequency LS coefficient at the level of $\beta_{LS} \approx 1.2 \times 10^{-11}$/MHz and a relative instability induced by the laser frequency fluctuation at the level of about 3.7×10^{-14} in the medium- to long-term scale up to $\tau = 10^4$ s in their Rb clock operating in CW-DR scheme when the laser frequency was stabilized to CO10-11 transition and not shifted by any AOM [35].

Table 3.5: Measured frequency LS coefficient β_{LS} from figure 3.27 when the laser power was at its maximum and the clock was operated in the Ramsey-DR scheme.

Laser locking poit	β_{LS} (/MHz)
F=1	$0.47(34) \times 10^{-14}$
F=2	$-5.7(5) \times 10^{-14}$

3.6 Microwave Power Shift

The microwave power shift (PS) is an unavoidable phenomenon in our Rb clock operating in the Ramsey-DR scheme and as mentioned in section 1.7.3.5, it is most likely consequence of the microwave field inhomogeneity inside the vapor cell [80, 81, 82]. Due to this microwave field inhomogeneity inside the vapor cell because of the position-shift phenomenon, different Rb atoms may experience different microwave powers (or microwave pulse areas) during the Rabi pulses and consequently have different frequencies contribute to the resonance signal. Here, we present preliminary results on an experimental study of the microwave PS measurement in our Ramsey-DR Rb clock. For these measurements, we operated our Ramsey-DR Rb clock under the conditions presented in table 3.1. We recorded the clock frequency as a function of the input microwave power to the cavity, $P_{\mu w}$. This measurement was repeated when the frequency of the laser used during the optical pumping and optical detection was stabilized to frequencies of six sub-Doppler CO21-23, CO22-23, $F = 23$, CO10-11, CO11-12 and $F = 12$ transitions in the D2 line of ^{87}Rb (see figure 2.10). Figure 3.29 shows the results of this measurement. In this figure, the microwave power where the microwave pulse area is $\theta = \pi/2$ is indicated by a dash line.

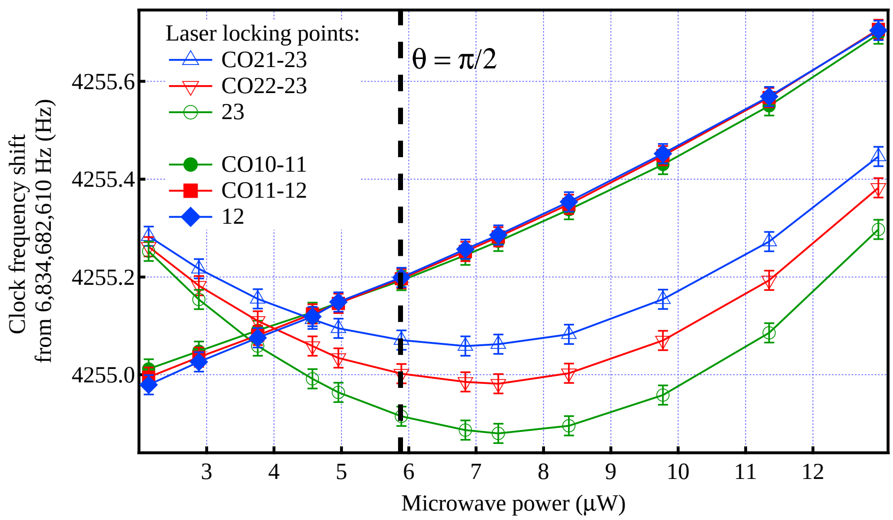

Figure 3.29: Clock frequency shift as a function of the microwave input power to the cavity when the clock is operating in the Ramsey-DR scheme. The dash line indicates the microwave power where the microwave pulse area is $\theta = \pi/2$.

From the measured data shown in figure 3.29, we measured the microwave PS coefficient $\frac{\partial \Delta\nu_{\mu w}}{\partial P_{\mu w}}$ by using linear fits near the operating point of the clock where the microwave power was 5.9 μW (i.e. microwave pulse area of $\theta = \pi/2$, see figures 3.3 and 3.3) for various laser locking points. These measured coefficients are presented in table 3.6. We can see that the microwave PS coefficient are negative (positive) when the laser frequency is stabilized to an $F = 1$ ($F = 2$) transition. The relative microwave power stability of the LO synthesizer was $\sigma_{P\mu w} \approx 10^{-3}$ at $\tau = 10^4$ s [41]. Hence, we can estimate the microwave power variation at the level of 6 nW at $\tau = 10^4$ s when the input microwave power was 5.9 μW. This induces a lock instability approximately at the level of $3(1) \times 10^{-14}$ up to $\tau = 10^4$ s from the LO synthesizer output power variations. This value is more than one order of magnitude higher than the one reported by Bandi et al. (9×10^{-16} up to $\tau = 10^4$ s) for their Rb clock operating in the CW-DR scheme with the note that their operating point was at 0.4 μW which was more than ten times lower than ours [35]. However, very recently Gozzelino et al. proposed a technique to stabilize the amplitude of the microwave field and reduce the microwave power variations in compact atomic clocks working in pulsed regime and exploits the atoms themselves as discriminators, without the need of any external reference [104].

Table 3.6: Measured microwave PS coefficients from data shown in figure 1.7.3.5 from linear fits near the operating point of the where the microwave power was 5.9 μW (microwave pulse area is $\theta = \pi/2$) and near the inversion points (microwave pulse area is $\theta \approx 1.1 \cdot \pi/2$) when the laser frequency was stabilized to an $F = 2$ transition.

Laser locking point	Microwave PS coefficient (/μW) @$\theta = \pi/2$	Microwave PS coefficient (/μW) @$\theta \approx 1.1 \cdot \pi/2$
CO21-23	$-2.8(6) \times 10^{-12}$	$\approx \pm 1.6 \times 10^{-13}$
CO22-23	$-3.8(7) \times 10^{-12}$	$\approx \pm 1.9 \times 10^{-13}$
F=23	$-6.0(9) \times 10^{-12}$	$\approx \pm 2.2 \times 10^{-13}$
CO10-11	$7.6(2) \times 10^{-12}$	—
CO11-12	$8.2(2) \times 10^{-12}$	—
F=12	$8.4(2) \times 10^{-12}$	—

In figure 3.29, we can see inversion points when the laser frequency was stabilized to an $F = 2$ transition (i.e., CO21-23, CO22-23, $F = 23$) and the input microwave power was about 6.5−7.5 μW where the microwave pulse area is approximately $\theta \approx 1.1 \cdot \pi/2$. For these inversion points the microwave PS coefficients $\frac{\partial \Delta \nu_{\mu w}}{\partial P_{\mu w}}$ reach their minimum. The origin of this observation is still unknown and it requires further investigations. Nevertheless, this observation allows us to reduce the induced microwave power instability in our Ramsey-DR Rb clock by varying the working point. We used the measurement data in figure 3.29 and estimated the first order coefficient by fitting to a parabolic function around the inversion points and knowing the output power uncertainty of about 1% from the LO synthesizer. These microwave PS coefficients are also listed in table 3.6. The microwave PS coefficients at the working point $\theta = \pi/2$ are approximately 20 times higher than at the inversion point $\theta \approx 1.1 \cdot \pi/2$. However, this change in the working condition results in: 1) slightly reducing the contrast of the Ramsey central fringe by $\approx 1\%$ (see figure 3.3) which is negligible, 2) increasing the cavity pulling effect approximately by 5% and reaching to $\approx 2 \times 10^{-15}$ (see equation (1.48)) and 3) increasing the β_{LS} approximately by 10% (estimated from figure 3.29) and reaching to $\approx 6 \times 10^{-16}/\mu$W.

From data shown in figure 3.29, in addition to the microwave PS coefficients, we also estimated the frequency LS coefficients β_{LS} at the working point ($\theta = \pi/2$). This estimation was done by taking a vertical cut in the graph shown figure 3.29 when $\theta = \pi/2$ to read the clock frequency, using the frequency separations for different laser frequencies and finally using equation (1.56). These measured

β_{LS} coefficients are presented in table 3.7. These results (as expected) were in good agreement with the ones presented in table 3.5.

Table 3.7: Measured frequency LS coefficient β_{LS} from figure 3.29 at the working point ($\theta = \pi/2$) in the Ramsey-DR scheme.

Laser locking poit	β_{LS} (/MHz)
F=1	$0.37(13)\times10^{-14}$
F=2	$-5.3(5)\times10^{-14}$

3.7 Optical Detection Duration and Short-Term Stability

In section 1.7.2.1, the analytical expression to predict the clock instability induced by the optical detection noise, $\sigma_y^{det}(\tau)$, was deduced and presented. We showed that the contribution of the optical detection noise can be estimated using equation (1.35). Here, we experimentally investigated the influence of the optical detection pulse duration t_d on the short-term frequency stability of our Rb atomic clock operating in the Ramsey-DR scheme. The investigations presented in this section have been published in [73].

To investigate the impact of the optical detection time t_d, we fixed the duration of the cycle time T_C so that the instability contribution from the Dick effect remains unchanged. The durations of the optical pumping pulse, Ramsey time and microwave pulses were set at $t_p = 0.4$ ms, $T_R = 3$ ms and $\tau_m = 0.4$ ms, respectively. We varied the optical detection duration t_d from 0.1 ms to 0.7 ms. For our measurements, the cycle time kept unchanged at $T_C = 4.94$ ms. For this estimate, we adjusted the duration of the gap time (pause time) after the optical detection pulse and the pumping pulse of the next cycle. In addition, laser input powers to the cavity during the optical pumping and optical detection sequences were fixed at 12 mW and 125 μW, respectively. We measured the central Ramsey fringe contrast at different optical detection duration t_d. Figure 3.30 shows the measured contrast of the Ramsey central fringe as a function of the optical detection duration. The contrast reduction with an increased detection time is due to the re-pumping effect during the detection phase, however, we still could obtain a contrast at approximately 35% when $t_d = 0.7$ ms.

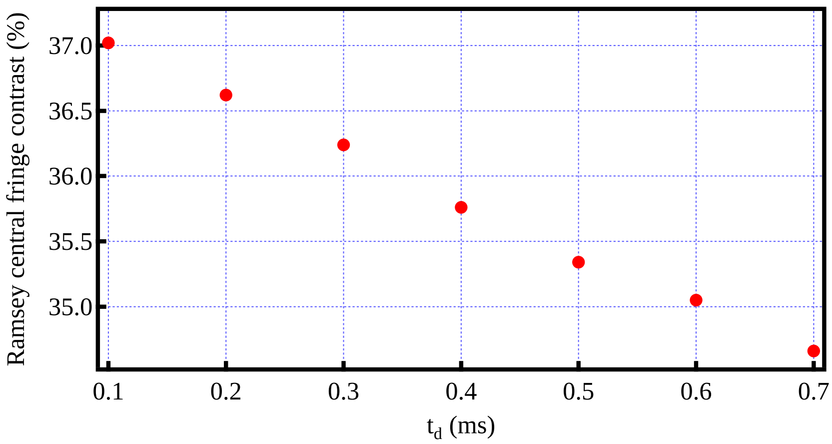

Figure 3.30: Measured Ramsey central fringe contrasts as a function of detection time t_d.

In addition, we measured the optical detection signal's RIN in DC mode when the laser power level was set to 125 μW, the same detection light level as during the optical detection phase. Figure 3.31 illustrates the typical RIN performance for the laser source.

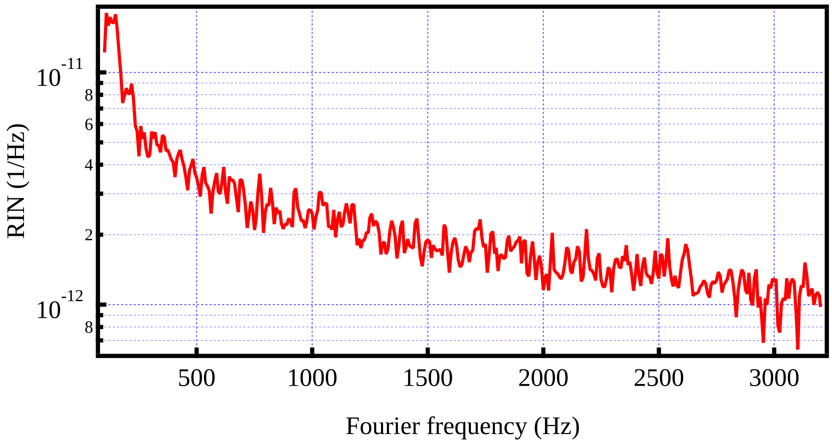

Figure 3.31: Typical RIN performance in DC mode of the laser source when the laser power level was set to 125 μW (equal to the one in stability measurements). The noise floor (detector in the dark) was approximately at the level of 9×10^{-15} (1/Hz).

For our Rb atomic clock, we calculated the clock instability induced by the optical detection noise $\sigma_y^{det}(\tau)$ from equation (1.35) as a function of optical detection time t_d when the averaging time τ is 1 s. In our calculations, Ramsey central fringe contrast and S_{RIN}^{det} were obtained from measured data shown in figures 3.30 and 3.31, respectively, the cycle frequency $f_C = T_C^{-1} \approx 200$ Hz and $Q_a \approx 4.2 \times 10^7$, with no other free parameters. This theoretical calculation is shown with a dash blue curve in figure 3.33. The theoretical curve includes a Dick-effect limit of $7.5 \times 10^{-14}\,\tau^{-1/2}$ (see section 1.7.2.2), which is independent of t_d. In addition to the theoretical calculations, we measured the short-term stability in our Rb clock operating in the Ramsey-DR scheme at various $t_d$under experimental conditions presented in table 3.1.

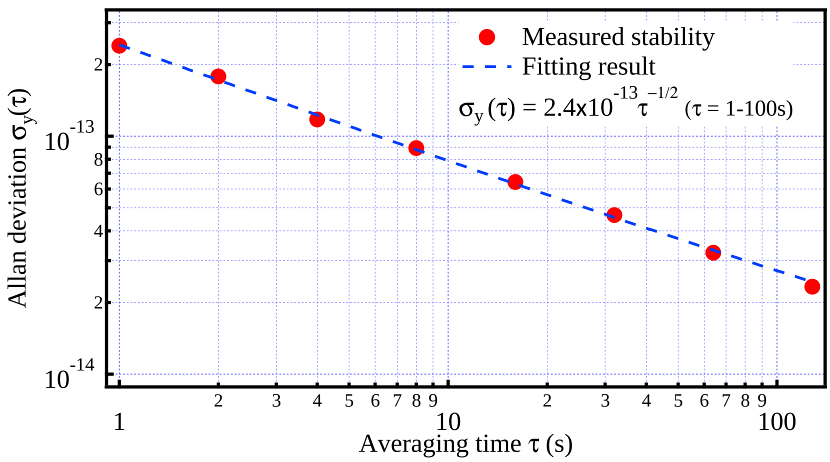

Figure 3.32: A measured short-term stability performance in our Rb clock operating in the Ramsey-DR scheme when $t_d = 0.7$ ms.

Figure 3.32 shows a typical measured short-term stability performance when optical detection duration was at $t_d = 0.7$ ms, where the short-term clock stability was obtained approximately at the level of $2.4 \times 10^{-13}\,\tau^{-1/2}$. The measured short-term stability at various optical detection times t_d are also shown in figure 3.33, in addition to the theoretical calculated one. The figure illustrates that the theoretical estimation based on equation (1.35) was consistent with the measurement results. Therefore, it can be concluded, up to a certain degree, that the effect of optical detection noise can be reduced by increasing the duration of optical detection phase in the Ramsey-DR scheme. This observation in the Ramsey-DR scheme provided us a degree of freedom to optimize the clock frequency stability by adjusting the duration of optical detection pulse in certain conditions.

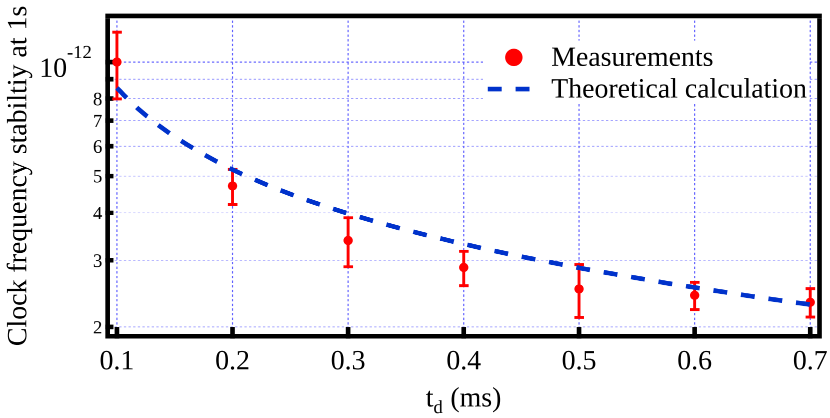

Figure 3.33: Theoretical (dash blue line) and measured (red solid circle) clock short-term stability at 1 s averaging time as a function of duration of optical detection sequence t_d.

3.8 Short-Term Clock Instability Budget

As mentioned in section 1.7, we consider 1 to 100 s averaging time range for short-term analysis. In this section, we present the short-term frequency stability performance of our Rb atomic clock operating in the Ramsey-DR scheme. We also compare this measurement result with the estimated contributions of the noise sources given in section 1.7.2.

We demonstrated a short-term stability at the level of $\sigma_y(\tau) = 2.4 \times 10^{-13}\,\tau^{-1/2}$ in our Ramsey-DR Rb clock which was shown in figure 3.32. Table 3.8 presents the estimated shot-noise-limit (from equation (1.29)) and the further noise contributions from the instability sources of the optical detection noise during the detection phase $\sigma_y^{det}(\tau)$ (equation (1.35)), the LO phase noise via Dick effect $\sigma_y^{LO}(\tau)$ (equation (1.36)) and the light shift $\sigma_y^{LS}(\tau)$ (equation (1.38)). It is seen that, in the short-term stability budget, the optical detection noise is dominant. This noise originated from the FM-to-AM noise conversion in the vapor cell [72] and the AM noise from the AOM [103]. The total estimated short-term stability of our Rb clock is calculated at the level of $2.2 \times 10^{-13}\,\tau^{-1/2}$ from equation (1.28) which is in good agreement with the measurement result. We note that, in our estimations we used a clock signal (Ramsey central fringe) obtained under experimental conditions presented in table 3.1 and the Ramsey time of $T_R = 3$ ms.

The measured short-term stability of $\sigma_y(\tau) = 2.4 \times 10^{-13}\tau^{-1/2}$ for our Ramsey-DR Rb clock is comparable to the state-of-the-art results previously demonstrated by Bandi et al. [35] and Micalizio et al. [34] also using Rb vapor cell atomic clocks. We note that our clock was operated in standard laboratory conditions (no vacuum enclosure or thermal chambers used). Bandi et al. used a similar physics package as ours but operating their clock in the CW-DR scheme in laboratory conditions and obtained a short-term stability at the level of $\sigma_y(\tau) = 1.4 \times 10^{-13}\tau^{-1/2}$, while Micalizio et al. operated

Table 3.8: Ramsey-DR Rb clock's short-term stability budget.

Shot-Noise-Limit	$\sigma_y^{SN}(\tau)$	$1.7 \times 10^{-14}\ \tau^{-1/2}$
Optical Detection	$\sigma_y^{det}(\tau)$	$2.1 \times 10^{-13}\ \tau^{-1/2}$
Dick Effect-LO	$\sigma_y^{LO}(\tau)$	$7.5 \times 10^{-14}\ \tau^{-1/2}$
Light Shift	$\sigma_y^{LS}(\tau)$	$\approx 1 \times 10^{-15}\ \tau^{-1/2}$
Total Estimated	$\sigma_y(\tau)$	$2.2 \times 10^{-13}\ \tau^{-1/2}$
Total Measured	$\sigma_y(\tau)$	$2.4 \times 10^{-13}\ \tau^{-1/2}$

their Rb clock under vacuum with a larger microwave cavity than ours and with a quality factor of approximately $Q_{cav} \approx 1000$ in the POP scheme and obtained a short-term stability at the level of $\sigma_y(\tau) = 1.7 \times 10^{-13}\tau^{-1/2}$. In both works (including ours, as mentioned above), the dominant instability source was the optical detection noise.

3.9 Long-Term Clock Instability Budget

In this chapter, we presented quantitative measurements of several sources of instabilities, their corresponding shift coefficients, and their direct consequences on the clock frequency stability, $\sigma_y(\tau)$ when it was operated in the Ramsey-DR scheme under experimental conditions presented in table 3.1. These coefficients and their respective estimated induced limits in medium- to long-term scale at $\tau = 10^4$ s are summarized in table 3.9. The coefficients and consequently the induced instabilities were obtained when the Rabi pulses in the Ramsey-DR scheme experienced exact $\pi/2$ microwave pulses (i.e. $\theta = \pi/2$). We note that this table is not a full metrological evaluation, but a first step towards it, based on the coefficients measured in this thesis and the parameters variations available from previous measurements presented in [41].

We can see from table 3.9 the medium- to long-term scales stability of our Ramsey-DR Rb clock was limited approximately at the level of $\sigma_y(\tau) \approx 2.7 \times 10^{-14}$ when the microwave pulse area of the Rabi pulses was $\theta = \pi/2$. This table also shows that this stability was mainly limited by the microwave PS effect that induced a contribution more than 2×10^{-14} to the clock performances. Our microwave PS measurements showed that (see section 3.6), this effect can be suppressed about 20 times by varying the operating point of the clock in which the microwave pulse area is approximately 10 % larger than $\pi/2$ ($\theta \approx 1.1 \cdot \pi/2$) and the laser frequency is stabilized to an $F = 2$ transition of the D2 line of ^{87}Rb. Therefore, in this optimized operating condition, we estimate a clock stability at the level of $\sigma_y(\tau) \approx 9.8 \times 10^{-15}$ in the medium- to long-term time scales.

Table 3.9: Summary of estimated instabilities in our Ramsey-DR atomic clock at $\tau = 10^4$ s. This table is not a full metrological evaluation, but a first step towards it, based on the coefficients we measured and the parameters variations available from previous measurements presented in [41].

Physical effect	Varying parameter	Coefficient abs.	Coefficient rel.	Variation at 10^4 s	Instability abs.	Instability rel.
Zeeman	C-field	$115\,\mathrm{Hz/G}$	$1.7 \times 10^{-8}/\mathrm{G}$	$0.1\,\mu\mathrm{G}$	$10\,\mu\mathrm{Hz}$	1.7×10^{-15}
Cell TC	T_{Cell}	$15.1\,\mathrm{mHz/K}$	$2.2 \times 10^{-12}/\mathrm{K}$	$3.5\,\mathrm{mK}$	$53\,\mu\mathrm{Hz}$	7.7×10^{-15}
Stem TC	T_{Stem}	$7.5\,\mathrm{mHz/K}$	$1.1 \times 10^{-12}/\mathrm{K}$	$4.6\,\mathrm{mK}$	$34.5\,\mu\mathrm{Hz}$	5.1×10^{-15}
Cavity pulling	T_{Cav}	$0.6\,\mu\mathrm{Hz/K}$	$8.8 \times 10^{-17}/\mathrm{K}$	$3.5\,\mathrm{mK}$	$2.1\,\mathrm{nHz}$	3.1×10^{-19}
Cavity pulling	μw pulse area	$0.3\,\mathrm{mHz}/\%$	$4.5 \times 10^{-14}/\%$	$0.034\,\%$	$10.2\,\mu\mathrm{Hz}$	1.5×10^{-15}
Intensity LS[1]	Laser intensity	$-0.26\,\mathrm{mHz}\ /\%$	$-3.8 \times 10^{-14}/\%$	0.1%	-26 μHz	3.8×10^{-15}
Intensity LS[2]	Laser intensity	$0.144\,\mathrm{mHz}\ /\%$	$2.1 \times 10^{-14}/\%$	0.1%	$14.4\,\mu\mathrm{Hz}$	2.1×10^{-15}
Frequency LS[3]	Laser frequency	$0.03\,\mathrm{mHz/MHz}$	$0.4 \times 10^{-14}/\mathrm{MHz}$	$10\,\mathrm{kHz}$	$0.3\,\mu\mathrm{Hz}$	0.4×10^{-16}
Frequency LS[4]	Laser frequency	$-0.38\,\mathrm{mHz/MHz}$	$-5.5 \times 10^{-14}/\mathrm{MHz}$	$10\,\mathrm{kHz}$	$3.8\,\mu\mathrm{Hz}$	5.5×10^{-16}
Microwave PS[3]	Microwave power	$0.05\,\mathrm{Hz}/\mu\mathrm{W}$	$8.0 \times 10^{-12}/\mu\mathrm{W}$	$6\,\mathrm{nW}$	$0.3\,\mathrm{mHz}$	4.8×10^{-14}
Microwave PS[4]	Microwave power	$-0.02\,\mathrm{Hz}/\mu\mathrm{W}$	$-4.4 \times 10^{-12}/\mu\mathrm{W}$	$6\,\mathrm{nW}$	$0.2\,\mathrm{mHz}$	2.4×10^{-14}

Total relative instability[1] 4.9×10^{-14}

Total relative instability[2] 2.7×10^{-14}

(1) The laser frequency is stabilized to the CO10-11 transition in the D2 line of ^{87}Rb.
(2) The laser frequency is stabilized to the CO21-23 transition in the D2 line of ^{87}Rb.
(3) The laser frequency is stabilized to an $F = 1$ transition in the D2 line of ^{87}Rb.
(4) The laser frequency is stabilized to an $F = 2$ transition in the D2 line of ^{87}Rb.

Predicted optimized total instability[5] $\approx 9.8 \times 10^{-15}$

(5) The laser frequency is stabilized to an $F = 2$ transition in the D2 line of ^{87}Rb and $\theta \approx 1.1 \cdot \pi/2$.

3.10 Conclusion

We demonstrated that our Rb atomic clock setup which contains a magnetron-type microwave cavity with a compact size ($45\,\mathrm{cm}^3$) and a low-quality factor (≈ 150) is able to operate in the Ramsey-DR scheme. We achieved a Ramsey clock signal with a contrast of 35% and a linewidth of 160 Hz by optimizing various parameters involved in the Ramsey-DR scheme, such as laser intensity, microwave amplitude and durations of the optical and microwave pulses. By using Rabi oscillations, we adjusted the duration and amplitude of the microwave pulses to achieve the microwave pulse area of $\theta = \pi/2$. The duration of the Ramsey time was optimized by measuring the short-term stability of our Rb clock. The uniformity of the microwave magnetic field in the cavity confirmed that our compact microwave cavity is a suitable candidate to be used in a Rb atomic clock operating in the Ramsey-DR scheme. The stem temperature coefficient of our vapor cell was measured approximately 1×10^{-12} /K which is one order of magnitude lower than that of the previous vapor cell design with a larger stem volume used in previous studies [41]. The perturbing effects of the LS and microwave PS were also studied. We measured and compared the intensity and frequency LS coefficients, α_{LS} and β_{LS}, in our Rb clock operating in both CW-DR and Ramsey-DR schemes. In the Ramsey-DR scheme, the intensity LS measurements were completed globally, which means that the laser intensity was varied in entire sequences simultaneously using an optical polarizer before the entrance of the physics package. We found that, when the clock operates in the Ramsey-DR scheme, a residual light with a power of 0.6μW due to non-perfect background light suppression passes through the vapor cell during the microwave pulses and the Ramsey time influences the intensity LS. We treated this residual light in the Ramsey-DR scheme equivalent to the applied light in the CW-DR scheme. In addition, we used the LS theory and simulations in the CW-DR scheme and presented a preliminary LS model and finally estimated intensity LS in our Ramsey-DR Rb clock. The estimated α_{LS} were in good agreement with the measured α_{LS} in our Rb clock. However, fully understanding the LS in the Ramsey-DR scheme requires more investigations and measurements. In addition to our LS study in the Ramsey-DR scheme globally, an alternative path to optimize the working parameters of the clock is to investigate the LS in each sequence of the scheme (i.e. optical pumping, optical detection and the Ramsey time) independently. We measured microwave PS coefficients and estimated an induced instability at the level of some 10^{-14} in the medium- to long-term scales near the operating point for our Ramsey-DR Rb clock. This estimation indicates that the microwave PS effect is the main limiting parameter in our Rb clock. In addition, based on these preliminary results, we found that the microwave PS effect can be suppressed if the clock is operated in the Ramsey-DR scheme when the Rabi pulses have microwave pulse area of $\theta \approx 1.1 \cdot \pi/2$ and the laser frequency is stabilized to an $F = 2$ transition in the D2 line of ^{87}Rb. We estimated that, this changing operating condition results in reducing the induced instability via the microwave PS effect by about 20 times and being not the main limiting parameter. We demonstrated the short-term stability at the level of $2.4 \times 10^{-13}\tau^{-1/2}$ for our Rb clock by considering the duration of the optical detection pulse. This measurement result was in good agreement with the estimated short-term stability obtained from our newly developed formula (equation 1.35) to estimate the instability induced by the optical detection noise. In addition, by using our formula, we re-evaluated the optimized T_R which was also obtained from short-term stability measurements. Finally, based on our quantitative measurements of several relevant sources of instabilities, we estimated a frequency stability of $\sigma_y(\tau) \approx 2.7 \times 10^{-14}$ in medium- to long-term scales for our Ramsey-DR clock operating with the nominal $\pi/2$ microwave pulses which was mainly limited by the microwave PS effect. However, we found that this stability can be improved up to $\sigma_y(\tau) \approx 9.8 \times 10^{-15}$ by varying the operating point to the microwave pulse area of $\theta \approx 1.1 \cdot \pi/2$ and stabilizing the laser frequency to an $F = 2$ transition in the D2 line of ^{87}Rb.

4 Measuring Relaxation Times in a Rubidium Vapor Cell

Vapor cell atomic frequency standards rely on long-lived ground-state spin-polarization of alkali vapor in the cell [105]. Generally, in a vapor cell atomic clock, the polarized alkali atoms may lose their polarization due to the relaxation processes that occur in the cell. These relaxation processes influence the contrast and/or linewidth of an atomic resonance line and consequently result in degradation of the clock stability. As previously mentioned (see section 1.6), in addition to the collisions of the polarized Rb atoms in the vapor cell, their interactions with electromagnetic fields are also among the relaxation sources. In our atomic clock, the electromagnetic fields (optical and microwave fields) are used to prepare/detect the resonance and, the C-field lifts the Zeeman degeneracy. The C-field may have some residual inhomogeneity in the vapor cell. In a microscopic view, Rb atoms experience various C-field amplitudes in the vapor cell due to the C-field inhomogeneity. This effect introduces additional dephasing [106], which results in a shorter coherence relaxation time. In this chapter we present methods to measure the relaxation times in the vapor cell of our Rb clock and discuss the measurement results.

We used three existing methods based on the Franzen scheme [37], continuous-wave double-resonance (CW-DR) scheme [35] and Ramsey-DR scheme [38] to measure the relaxation times in the same Rb vapor cell (see section 2.3.1). We demonstrated that the obtained coherence relaxation times from the CW-DR and Ramsey-DR methods are affected by C-field inhomogeneity across the vapor cell and is shorter than the "intrinsic" coherence relaxation time calculated previously (see section 1.6). To measure the intrinsic coherence relaxation time T_2, we presented our newly proposed Optically-Detected Spin-Echo (ODSE) method [107]. We demonstrated that the ODSE method suppresses the effect of C-field inhomogeneity across the vapor cell and enables the measurement of intrinsic T_2. The investigations presented in this chapter were done in collaboration with the Institute of Physics of Belgrade University [3] and published in [107].

4.1 Detection Methods

Franzen, Ramsey-DR and ODSE methods operate in pulse schemes. The timing sequence of these three methods starts with an optical pumping pulse and ends with an optical detection pulse using a laser with 780 nm wavelength. The details of the sequences for each method are presented in the following sections. The optical pumping pulse creates a population imbalance between the two ground states $F_g = 1$ and $F_g = 2$ of Rb atoms in the vapor cell (see figure 4.1). In the Ramsey-DR and ODSE methods, after an optical pumping pulse, series of $\pi/2$ and/or π microwave pulses that create/modify coherence between the ground states are applied. Finally, an optical detection pulse is used to measure the optical

[3] Within the project FNS (SCOPES): "Ramsey spectroscopy in Rb vapor cells and application to atomic clocks" no. 152511 (2014-2018).

density (OD) in the vapor cell using a photodetector. OD is a logarithmic measure of light attenuation in a medium, defined by:

$$OD = -\ln\left(\frac{I_t}{I_0}\right), \tag{4.1}$$

where I_0 and I_t are the incident and transmitted laser probe pulse intensities, respectively. The variation of the cell's OD as a function of time yields information about the population and/or coherence relaxation times of the Rb atoms in the vapor cell. For our measurements, we used a photodetector before and after the vapor cell to record I_0 and I_t, respectively, and obtained the cell's OD from equation (4.1).

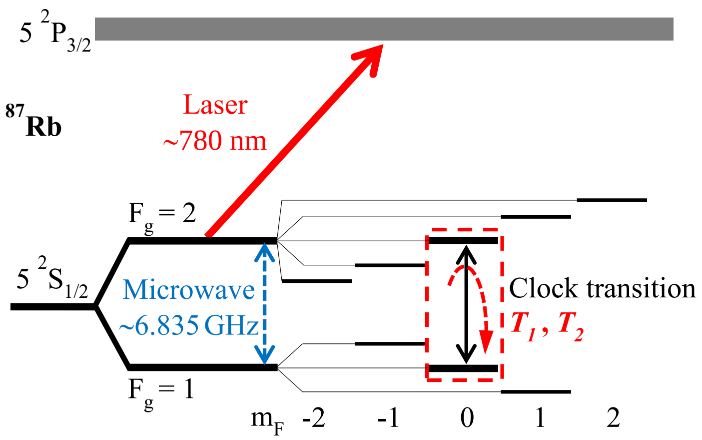

Figure 4.1: Atomic level scheme of ^{87}Rb. The optical pumping with the laser at 780 nm creates a population imbalance between two ground states $F_g = 1$ and $F_g = 2$ via excited state $5^2P_{3/2}$. Due to Doppler and collisional broadening, the hyperfine levels of the excited-state are not resolved by the laser light. The clock transition $|F_g = 1, m_F = 0\rangle \leftrightarrow |F_g = 2, m_F = 0\rangle$ is addressed by choosing appropriate microwave frequency. T_1 and T_2 are population and coherence relaxations times, respectively, particularly for the clock transition. Figure is taken from [107].

In pulsed schemes, the laser probe pulse during optical detection does not resolve the atomic excited state $5^2P_{3/2}$ because all optical transitions to this excited state are overlapped within the Doppler linewidth. Moreover, the clock transition cannot be addressed selectively by the laser alone, because both the intrinsic transition linewidth and the Doppler linewidth are much larger than the Zeeman splitting in the $5^2S_{1/2}$ ground states. Hence, for these pulsed schemes, we can only address the population relaxation time between *all* m_F Zeeman levels of the ground states $F_g = 1$ (or $F_g = 2$) *simultaneously* and we cannot measure the population relaxation time particularly for the clock transition.

4.1.1 Notation Summary

In this thesis, we used the notations T_1 and T_2 for the *intrinsic* population and coherence relaxation times, respectively, particularly for the clock transition. The same notation was used previously (see section 1.6) to present the calculated intrinsic relaxation times. As previously mentioned, in the pulsed methods (Franzen, Ramsey-DR and ODSE) because we used the laser for detection we could access the population relaxation time between *all* m_F Zeeman levels (and not the clock transition) of the ground states $F_g = 1$ or $F_g = 2$. To avoid confusions in the notations, we showed the population relaxation time applying collectively to *all* m_F sublevels of a given F state with T_1'. In the CW-DR, Ramsey-DR and ODSE methods, the microwave radiations are used to select the specific Zeeman sublevels of interest. Therefore, with these methods, we were able to access the coherence relaxation time particularly for the clock transition. However, in the cases of the CW-DR and Ramsey-DR methods, the effect of C-field inhomogeneity in the vapor cell was included in the measured coherence relaxation time. For these two methods, we showed the coherence relaxation time for the clock transition with T_2^*. The summary of the notations and their descriptions are also listed in table 4.1.

Table 4.1: Notations used for the relaxation times and their descriptions

	Description	Transition	Measurement method
T_1'	Population relaxation time	*all* m_F levels	Franzen, Ramsey-DR, ODSE
T_2^*	Coherence relaxation time with impact of C-field inhomogeneity	clock transition	CW-DR, Ramsey-DR
T_2	Intrinsic coherence relaxation time	clock transition	ODSE

4.2 Franzen Method

Franzen's method [37] is a well-known technique that is widely used to measure population relaxation time. This method is operated in a pulse scheme and is an all optical method without any microwave radiations. The Franzen method is also known as "relaxation in the dark" method. The timing sequence of the Franzen scheme is shown in the inset of figure 4.2. First, an optical pumping pulse with the laser creates a population imbalance between the ground states of ^{87}Rb atoms. After the optical pumping pulse, the laser beam is switched off with the AOM. Then during a dark time T_{Dark}, the hyperfine population imbalance relaxes toward the thermal equilibrium at a rate $1/T_1'$. Finally, an optical detection pulse with the laser probes the sample's OD. In our experiments, durations of the optical pumping and optical detection pulses were fixed at 1 ms and 0.1 ms. The frequency of the laser in optical pumping and optical detection pulses were identical but their input powers to the cavity remained constant at 12 mW and 110 μW, respectively. We varied the dark time T_{Dark} and measured OD using equation (4.1). Figure 4.2 shows the obtained cell's OD as a function of T_{Dark}. As dark time increased, the cell's OD also increased. This relationship is explained by the fact that, for longer T_{Dark}, more atoms decay from the $F_g = 1$ ground state to the $F_g = 2$ ground state. The error bars shown in figure 4.2 are dominated by technical noise and increase with increasing T_{Dark} due to decreasing transmitted intensity I_t. The measurement data were fitted with equation:

$$OD = A - B\exp(-T_{Dark}/T_1'^{Franzen}), \tag{4.2}$$

where A, B and $T_1'^{Franzen}$ were the fitting parameters. For the data shown in figure 4.2, the population relaxation time was determined as $T_1'^{Franzen} = 3.23 \pm 0.06$ ms from equation (4.2). Because the detection was conducted with the laser, the obtained population relaxation time is valid for all m_F levels together (see section 4.1). The population relaxation time $T_1'^{Franzen}$ was measured with the Franzen method when the laser input power during the optical detection pulse was 80 μW and 50 μW, and the other experimental conditions were remained constant. Table 4.2 lists the measured $T_1'^{Franzen}$ at different laser detection powers, showing that $T_1'^{Franzen}$ is independent of the laser detection power within the uncertainties. $T_1'^{Franzen}$ was also measured when the optical detection pulse duration varied by $\pm 50\%$ and the result did not change significantly (approximately 5%).

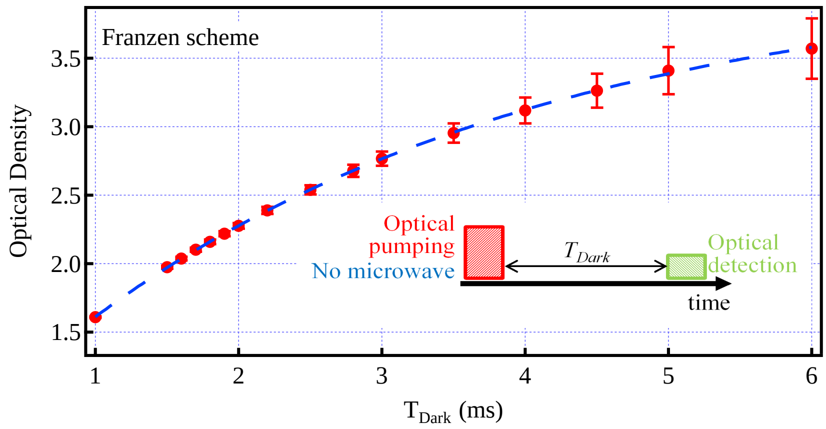

Figure 4.2: Vapor cell's OD as a function of T_{Dark} in the Franzen scheme when the durations of the optical pumping and optical detection pulses are 1 ms and 0.1 ms, respectively. The laser input powers in pumping and detection pulses are 12 mW and 110 μW, respectively. Solid red circles are the experimental data with corresponding error bars and blue dashed curve is a fit based on equation (4.2). Error bars are dominated by technical noise and increase with increasing T_{Dark} due to decreasing transmitted intensity, I_t. Inset: timing sequence of the Franzen scheme.

Table 4.2: Measured $T_1^{\prime Franzen}$ at various laser detection powers when the optical pumping and optical detection pulse durations were fixed at 1 ms and 0.1 ms, respectively and the laser pumping power was 12 mW. The statistical uncertainties for all the measured $T_1^{\prime Franzen}$ were about ± 0.1 ms.

Laser detection power (μW)	110	80	50
$T_1^{\prime Franzen}$ (ms)	3.23	3.25	3.30

4.3 Continuous-Wave-DR Method

The CW-DR method is also used to measure coherence relaxation time. The details of the CW-DR principle are presented in [9, 41]. In the CW-DR scheme, two resonant electromagnetic fields of light (laser) and microwave are required that are applied simultaneously. In this scheme, the laser optically pumps the Rb atoms, while simultaneously a near-resonant microwave field with the ^{87}Rb hyperfine clock transition is applied. The transmitted light signal as a function of microwave frequency is recorded by a photodetector after the vapor cell. It is a measure of the atomic ground state polarization known as DR signal that typically has a Lorentzian shape. The frequency of the microwave field selects a particular hyperfine transition, which enables measurements of coherence relaxation time only for the two involved m_F states.

Figure 4.3 shows a typical DR signal, which is obtained when the laser input power to the cell is 125 μW and the microwave frequency is scanned near the clock transition frequency with an injected microwave power to the cavity of 0.45 μW. The linewidth of the DR signal is a measure of the coherence relaxation rate of the clock transition [23]. However, this linewidth is additionally increased by optical and microwave power broadenings. Therefore, to extract the intrinsic DR signal linewidth $\Delta\nu_{1/2}$ the influence of the power broadenings must be removed from the linewidth of the obtained DR signal. To obtain the intrinsic $\Delta\nu_{1/2}$, first we recorded the DR signals at various laser and microwave powers and then extrapolated the DR signal linewidths to zero with respect to both optical and microwave powers.

The linewidth of the DR signals is extracted from each DR spectrum by using a Lorentzian fitting

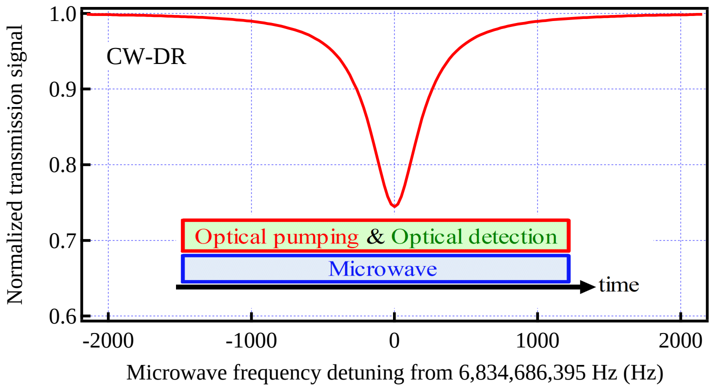

Figure 4.3: Typical DR signal in the CW-DR scheme when the microwave and laser input powers to the cavity are 0.45 μW and 125 μW, respectively. Inset: the CW-DR scheme.

function. Figure 4.4 shows the DR signal linewidth obtained from the fits as a function of the laser input power for different injected microwave powers. For each set of measured linewidth at a certain microwave power, we used a linear fit and extrapolated to zero laser power in order to subtract the optical power broadening from the linewidth. Figure 4.5 shows the DR signal linewidth extrapolated to zero light intensity (from the fits in figure 4.4) as a function of injected microwave power to the cavity. The uncertainties shown in figure 4.5 are statistical uncertainties from the fitting obtained from the graphs in figure 4.4. The second extrapolating to zero microwave power yielded the intrinsic $\Delta\nu_{1/2} = 147 \pm 22$ Hz. Finally, we estimated the coherence relaxation time $T_2^{*CW-DR} = 2.2 \pm 0.4$ ms for the clock transition using the formula [9]:

$$T_2^{*CW-DR} = \frac{1}{\pi}\frac{1}{\Delta\nu_{1/2}}. \tag{4.3}$$

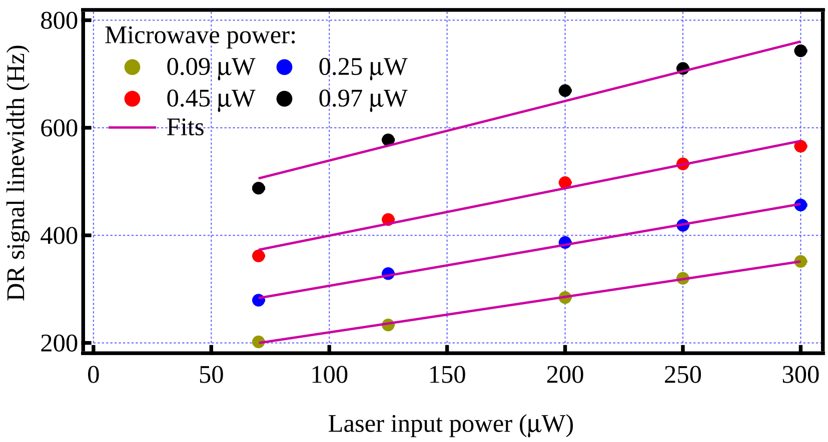

Figure 4.4: The obtained DR signal linewidth from the Lorentzian fit to the DR signals as a function of the laser input power for different injected microwave powers.

The uncertainty of 0.4 ms is statistical from the linear fit of the data presented in the graph of figure 4.5. However, the obtained coherence relaxation time from the CW-DR method is significantly smaller than the predicted intrinsic $T_2 = 4.5$ ms from table 1.3. This difference can be attributed to imperfect extrapolations to zero light and microwave powers. In addition, the presence of inhomogeneity of the static magnetic field in the vapor cell results in a shortening of the coherence relaxation time. Therefore, the coherence relaxation time obtained from the CW-DR method is shown by T_2^{*CW-DR}, with a superscript "*" (see section 4.1.1).

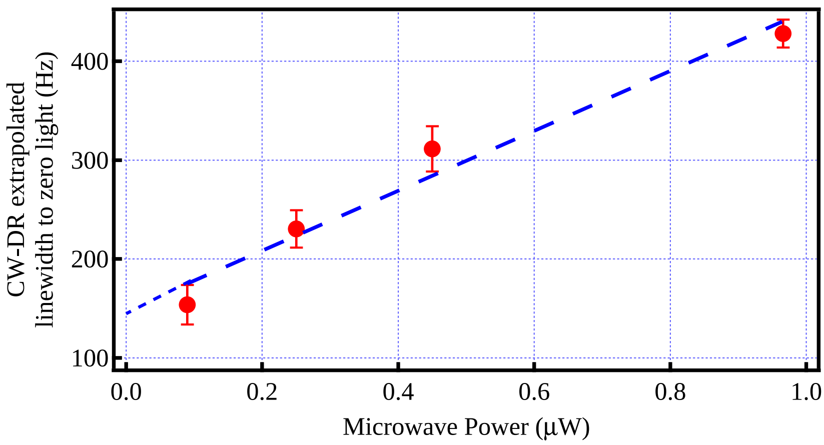

Figure 4.5: Extrapolation of the DR signal linewidth to zero microwave power. Solid red circles are the linewidths obtained by extrapolation to zero laser power and the blue dashed line is the linear fit of the data. The uncertainties are statistical from fitting obtained from figure 4.4. [107]

4.4 Ramsey-DR Method

The principle of the Ramsey-DR technique [83, 44] was presented in details in section 1.5). This method was presented in [38] to measure relaxation times in a Rb micro-cell. In this section, we used the Ramsey-DR method to measure the relaxation times in the Rb vapor cell. The timing sequence of the Ramsey-DR scheme is shown in figure 1.11. After the optical pumping pulse (which creates a population imbalance between ^{87}Rb ground-states), two coherent $\pi/2$ microwave pulses were applied and separated by the Ramsey time T_R. The frequency of the $\pi/2$ microwave pulses can select the specific transition between the Zeeman sublevels of interest (such as in the CW-DR scheme) and enables the measurement of the coherence relaxation time specific for that transition. Because we were interested in the clock transition, we applied the microwave pulses with a frequency close to the Rb clock transition frequency. In contrast to the Ramsey-DR method used to operate the clock, the microwave frequency was slightly detuned by δ from the Rb clock transition frequency. After the first $\pi/2$ microwave pulse, the atomic spins continue their free evolution during the Ramsey time. The detuning of the microwave frequency from the atomic resonance, δ, results in the atomic superposition accumulating a phase relative to the microwave. The second $\pi/2$ microwave pulse converts this phase into a population difference between the clock states. Using this method, the Ramsey oscillations were recorded in time by scanning T_R and the relaxation times were extracted from the decay of the Ramsey oscillation.

For the Ramsey-DR method, similar to the Franzen method, we recorded OD of the vapor cell by measuring I_0 and I_t from equation (4.1). Scanning the Ramsey time T_R resulted in oscillations of the atomic population and variation of the OD. The variation of OD as a function of T_R yields information about relaxation times of the Rb atoms in the vapor cell. Figure 4.6 shows the recorded OD as a function of Ramsey time T_R when a C-current of 1.6 mA is applied to the cavity and the microwave is detuned from the clock transition by $\delta = 3.8$ kHz. For this measurement, the experimental conditions in the Ramsey-DR scheme were as follows: optical pumping pulse, duration of 0.4 ms, laser input power of 14 mW; optical detection pulse, duration of 0.7 ms, laser input power of 125 μW; and both microwave pulses, duration of 0.4 ms, amplitude corresponding to a power of 15 μW injected into the cavity. The data shown in figure 4.6 was fitted with the function [38]:

$$OD = A - B\exp(-T_R/T_1^{\prime Ramsey}) + C\exp(-T_R/T_2^{*Ramsey})\sin(2\pi\delta T_R + \phi), \tag{4.4}$$

where A, B, C, $T_1^{\prime Ramsey}$, $T_2^{*Ramsey}$, δ and ϕ are the fitting parameters. This fit yielded the relaxation times of $T_1^{\prime Ramsey} = 3.20 \pm 0.01$ ms and $T_2^{*Ramsey} = 3.95 \pm 0.25$ ms. In addition, the fit delivered the microwave detuning from resonance of $\delta = 3.8 \pm 0.003$ kHz which was in excellent agreement with the measurement conditions. The uncertainties are statistical from the fit to single measurement data as shown in figure 4.6. In figure 4.6, two decay rates in OD are observed with increasing T_R: (1) a general exponential decay that corresponds to the population relaxation time $T_1^{\prime Ramsey}$, which is described by the second term of equation (4.4); (2) a damping of small Ramsey oscillations that corresponds to the coherence relaxation time $T_2^{*Ramsey}$, which is described by the third term of equation (4.4).

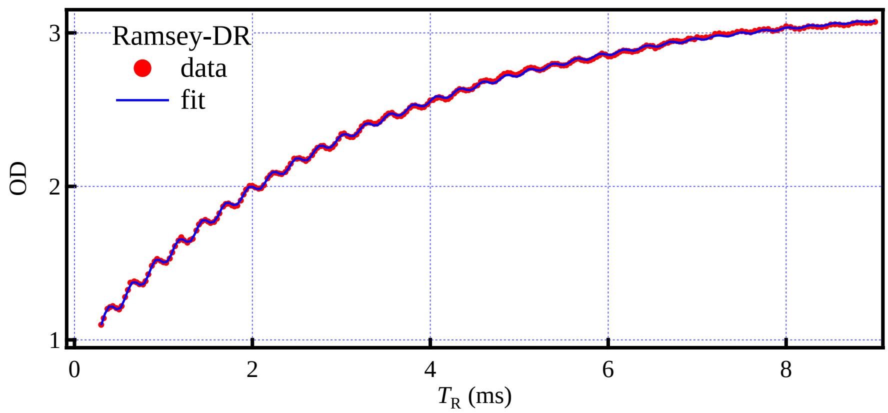

Figure 4.6: Optical density of the vapor cell in the Ramsey-DR scheme as a function of T_R. Solid red circles are the experimental data and blue dashed curve is a fit based on equation (4.4).

Figure 4.7 is the plot of ΔOD as a function of T_R which is the third term of equation (4.4), i.e.:

$$\Delta OD = C\exp(-T_R/T_2^{*Ramsey})\sin(2\pi\delta T_R + \phi). \tag{4.5}$$

Figure 4.7 shows the damping of the Ramsey oscillations very clearly. As mentioned previously, in the Ramsey-DR method, similar to the Franzen method, the detection is conducted using a laser. Therefore, we measured the population relaxation time for all m_F levels confounded, shown by $T_1^{\prime Ramsey}$. The measured population relaxation time obtained from the Ramsey-DR is consistent with the one obtained from Franzen method ($T_1^{\prime Ramsey} = T_1^{\prime Franzen} \approx 3.20$ ms). However, in contrast to $T_1^{\prime Ramsey}$ population relaxation time, $T_2^{*Ramsey}$ refers to the coherence relaxation time specific for the clock transition alone [38]. The measured coherence relaxation time obtained from the Ramsey-DR method was larger than the one obtained from the CW-DR method ($T_2^{*Ramsey} \approx 4$ ms vs $T_2^{*CW-DR} \approx 2.2$ ms) but shorter than the predicted intrinsic coherence relaxation time $T_2 = 4.5$ ms. Shorter $T_2^{*Ramsey}$ may be due to the presence of C-field inhomogeneity (in the $\vec{z}$ direction) across our vapor cell; however, the relative C-field inhomogeneity was only 2% (see figure 2.23).

To investigate the effect of C-field inhomogeneity across our vapor cell on the measured coherence relaxation time by using the Ramsey-DR scheme, we measured $T_2^{*Ramsey}$ when all the experiment parameters remained constant, except for the C-field in the cavity. For this new set of measurements, the C-current was set to 3.2 mA (two times higher than the previous measurements), which resulted in

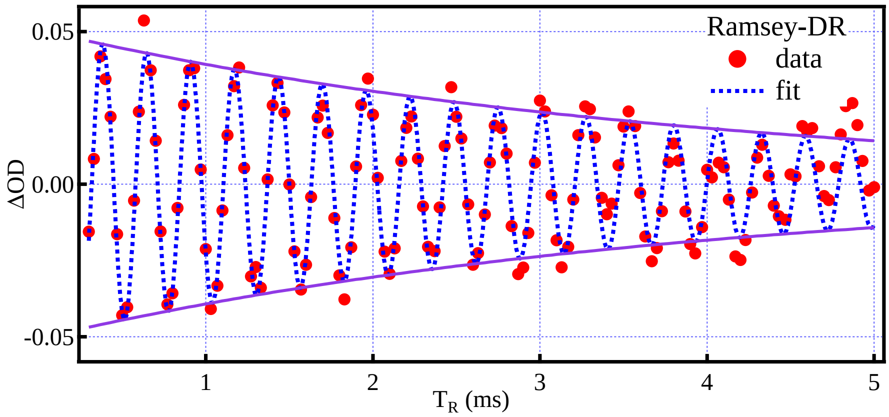

Figure 4.7: Plot of the ΔOD as a function of T_R in the Ramsey-DR scheme.

increased absolute C-field inhomogeneity in the vapor cell (see figure 2.23). At the higher C-field, the coherence relaxation time was found to be $T_2^{*Ramsey} = 3.80 \pm 0.25$ ms, which was approximately 4% shorter than $T_2^{*Ramsey} = 3.95 \pm 0.25$ ms obtained at the lower C-field. Although these obtained values for $T_2^{*Ramsey}$ cover each other with respect to their uncertainties, we observed a systematic reduction in $T_2^{*Ramsey}$ at the higher C-field. This observation motivated us to propose our ODSE method to suppress the effect of C-field inhomogeneity in the vapor cell and measure the intrinsic T_2 (see section 4.5).

4.5 Optically-Detected Spin-Echo (ODSE) Method

As previously mentioned (see section 1.6), the interaction of polarized Rb atoms in the vapor cell with the applied electromagnetic fields is interpreted as the source of relaxations. In our atomic clock, optical and microwave fields are used to prepare, drive and detect the resonance. In addition, the static magnetic field is applied to lift the Zeeman degeneracy and access the clock levels. In section 2.4, the relative C-field inhomogeneity in the $\vec{z}$ direction across our Rb vapor cell was measured at approximately 2%. Due to this C-field inhomogeneity, in a microscopic view, the Rb atoms may experience different C-fields in the vapor cell. This effect causes additional dephasing, which impacts the coherence between atomic states and decreases the coherence relaxation time [108].

In this section, we present our newly proposed Optically Detected Spin Echo (ODSE) method to measure the relaxation times, particularly the "intrinsic" coherence relaxation time T_2, in a Rb vapor cell with buffer gases. Our ODSE method is inspired by the classical NMR spin-echo method discovered by Hahn [39]. In classical NMR, Hahn's spin-echo method was used to narrow the resonance line broadening in inhomogeneous static magnetic fields. Hahn showed in his work that, after applying an initial $\pi/2$ pulse to an ensemble of spins in a liquid sample placed in a large static magnetic field, spins start to dephase at different precession rates. These different precession frequencies are caused by different phenomena, such as chemical shift effects, spin-spin coupling effects and presence of an inhomogeneous magnetic field [109]. Hahn applied an additional π RF pulse to refocus the spins. In the other words, the individual magnetic spin vectors regained phase coherence after the second RF pulse. Previous studies have also used the technique of applying multi-pulses with a $\pi/2$ pulse, followed by a single π pulse of the same phase. Although this $\pi/2-\pi$ echo sequence originated from Carr–Purcell (CP method) [106], it is named a Hahn-echo in the literature. The CP method was modified by Meiboom–Gill (called CPMG) [110] so that the initial $\pi/2$ preparation pulse is followed by a train of π pulses to measure coherence relaxation time in NMR systems. In solid-state systems, various modified NMR spin-echo techniques have been studied both theoretically and experimentally to extend the coherence time [111, 112]. Similar techniques such as the dynamical decoupling approach [113, 114] and gradient echo memory [115] applied in quantum memory [116] studies aim, for example, to minimize the detrimental effect of inhomogeneous broadening on the coherence storage time of the quantum bit (qubit) or to use the artificially created broadening for storage of broad-band optical pulses without deterioration of the storage time [117, 118]. In the classical NMR spin-echo, a pickup-coil is used to detect the magnetic moments' precession of the sample [106]. However, integrating a pickup in our atomic clock for the detection would be difficult. Moreover, it may produce additional noises by collecting the noise from the vapor cell and re-emitting the collected microwaves through the wires outside of the cell. Therefore, in our ODSE method, similar to Franzen and Ramsey-DR methods, we used a photodetector to measure *OD* in the vapor cell. The photodetector is much more robust, reliable than the pickup-coil and it does not feedback noises to the atoms.

Similar to classical NMR experiments, in the Ramsey-DR method after the first $\pi/2$ pulse, due to the presence of C-field inhomogeneity across the vapor cell, the atomic spins dephase at different rates. Then, their coherences start to decay and consequently cause a shorter coherence relaxation time than the intrinsic T_2. To suppress the effect of C-field inhomogeneity (in the $\vec{z}$ direction) and assess the intrinsic T_2, we modified the Ramsey-DR sequences by applying a π pulse between two $\pi/2$ pulses (similar to Hahn spin echo) and developed the ODSE method. The timing sequence of the ODSE method is shown in figure 4.8. For our measurements, the π pulse had the same frequency and amplitude as the $\pi/2$ pulses, but its duration was two times longer. The π pulse was separated from each of the two $\pi/2$ pulses by a dephasing/rephasing time T_{SE}. The π pulse flipped the direction of dephasing spins and reversed the spin phases. After some time equal to the dephasing time T_{SE}, the dephased states were rephased at the instant of the second $\pi/2$ microwave pulse. Finally, the detection by the second $\pi/2$ pulse and the laser pulse destroyed the atomic coherences that primarily reconverted to atomic population difference for the optical read-out.

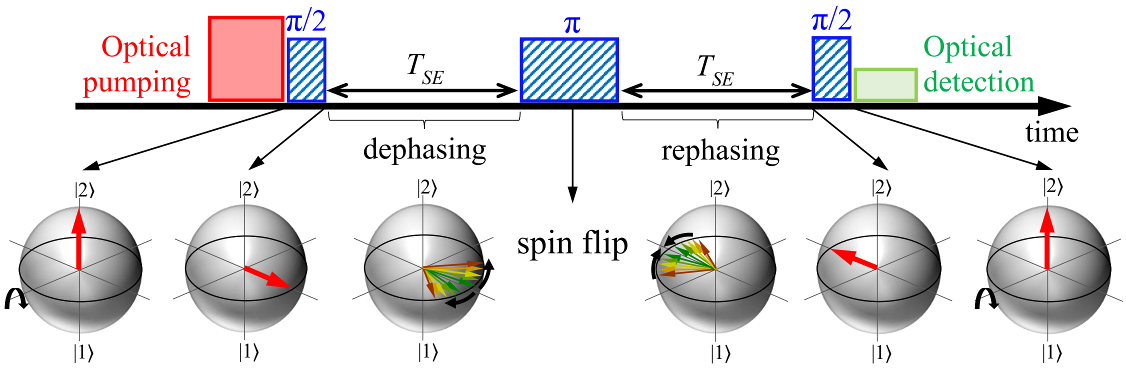

Figure 4.8: Timing sequence of the ODSE method.

To measure relaxation times in the vapor cell, we used the ODSE method and recorded *OD* of the vapor cell by measuring I_0 and I_t from equation (4.1) when the dephasing/rephasing time T_{SE} was varied. To compare the measured relaxation times obtained from the ODSE and Ramsey-DR methods, we kept all the experimental conditions of optical pumping, optical detection and $\pi/2$ microwave pulses identical to those used for the Ramsey-DR method measurements (see section 4.4). The applied C-current and the microwave frequency detuning from the clock transition δ were set to 1.6 mA and 3.8 kHz respectively (similar to the Ramsey-DR method). Figure 4.9 shows the measured *OD* as a function the dephasing/rephasing time T_{SE}. Furthermore, the experimental data shown in this figure was fitted to the function:

$$OD = A - B\exp(-T_{SE}/T_1'^{ODSE}) + C\exp(-T_{SE}/T_2^{ODSE})\sin(4\pi\delta T_{SE} + \phi), \tag{4.6}$$

where A, B, C, $T_1'^{ODSE}$, T_2^{ODSE}, δ and ϕ were the fitting parameters. The fit yielded relaxation times of $T_1'^{ODSE} = 3.21 \pm 0.05$ ms and $T_2^{ODSE} = 4.30 \pm 0.85$ ms with a detuning of $\delta = 3.8 \pm 0.005$ kHz. The uncertainties are statistical from the fit to single measurement data. In figure 4.9, when T_{SE} increases, we observed a general exponential decay of OD corresponding to the population relaxation time $T_1'^{ODSE}$, which is described by the second term of equation (4.6) and a decay of the small oscillations corresponding to coherence relaxation time T_2^{ODSE}, which is described by the third term of equation (4.6).

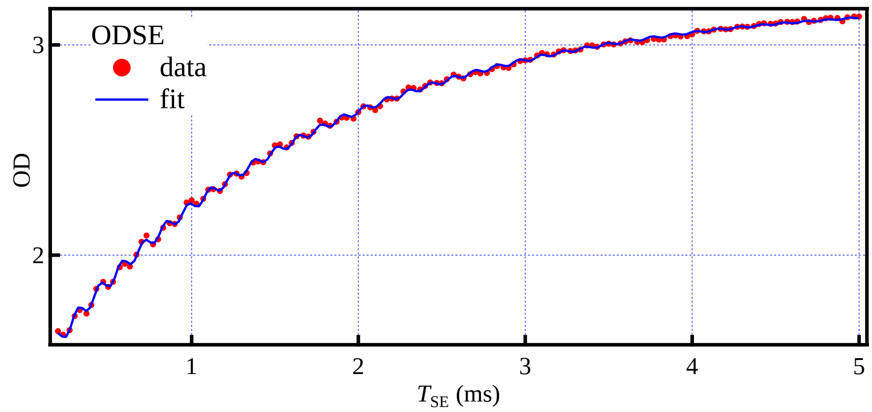

Figure 4.9: Optical density of the vapor cell in the ODSE scheme as a function of T_{SE}. Solid red circles are the experimental data and blue dashed curve is a fit based on equation (4.6).

In the ODSE method, similar to the Franzen and Ramsey-DR methods, $T_1'^{ODSE}$ corresponds to the population relaxation time for the transitions between all m_F levels (see section 4.1). For our measurements, there was a very good consistency with the obtained T_1' from the Franzen, Ramsey-DR and ODSE methods. Due to the suppression of C-field inhomogeneity in the $\vec{z}$ direction across the vapor cell, the obtained coherence relaxation time from the ODSE method T_2^{ODSE} was larger than that obtained from the Ramsey-DR method ($T_2^{ODSE} > T_2^{*Ramsey}$). T_2^{ODSE} and was in a good agreement with the predicted intrinsic coherence relaxation time $T_2 = 4.5$ ms. To prove the principle in the ODSE method, the measurement was repeated at a higher C-field inhomogeneity across the vapor cell by doubling the C-current to 3.2 mA. In this condition, the coherence relaxation time was measured at $T_2^{ODSE} = 4.26 \pm 0.80$ ms which is consistent with the measured coherence relaxation time when the C-current was 1.6 mA (variation, 1%). By contrast, in the case of the Ramsey-DR method, the variation of the measured coherence relaxation time in the lower and higher C-fields was approximately 4% (see section 4.4). Table 4.3 lists the measured coherence relaxation times using the Ramsey-DR and ODSE methods in two different C-fields. In the same C-fields, the obtained coherence relaxation time from the ODSE method was larger than that from Ramsey-DR method systematically.

In relaxation time measurements with both Ramsey-DR and ODSE methods, a trade-off exists when selecting the microwave detuning δ. For very small δ, large initial variations in I_t and consequently in OD can be observed, but only a few oscillations occur before they are damped away at approximately T_R or $T_{SE} \approx 2 \cdot T_2$. For very large δ, many oscillations can be observed over this timescale but the maximum variation of I_t is small, which reduces the signal-to-noise ratio of OD data.

Table 4.3: Measured coherence relaxation times with Ramsey-DR and ODSE methods in different C-fields.

C-current (mA)	$T_2^{*Ramsey}$ (ms)	T_2^{ODSE} (ms)
1.6	3.95 ± 0.25	4.30 ± 0.85
3.2	3.80 ± 0.25	4.26 ± 0.80

In our experiments, the measured relaxation times from the ODSE method had uncertainties 3–5 times larger than those from the Ramsey-DR method. This difference can be explained by two factors: (1) because the duration of one complete interrogation cycle from the ODSE method is approximately two times longer than that from Ramsey-DR method (2.7 ms$+2 \cdot T_{SE}$ versus 1.9 ms$+T_R$) and the exploited oscillation decays with a time constant T_2, the ODSE signal has also a lower amplitude than the Ramsey-DR signal; and (2) the residual instabilities of the microwave-synthesizer frequency over the entire measurement duration of approximately two hours may introduce additional noise to the signal (for the Ramsey-DR and ODSE methods approximately 250 (figure 4.6) and 150 (figure 4.9) data points are presented, respectively).

4.6 Summary of Measured Relaxation Times

Table 4.4 lists the measured relaxation times in the vapor cell of our Rb atomic clock using different methods presented in this chapter when the C-current was at 1.6 mA corresponding to the nominal working condition. In addition to the measurement results, the table contains the predicted intrinsic relaxation times calculated in section 1.6.

Table 4.4: Measured relaxation times in the vapor cell of our Rb atomic clock with Franzen, CW-DR, Ramsey-DR and ODSE methods when the C-current was at 1.6 mA. The intrinsic relaxation times was estimated in section 1.6.

	Clock transition			All m_F levels
Methods	T_1 (ms)	T_2 (ms)	T_2^* (ms)	T_1' (ms)
Franzen	—	—	—	3.23 ± 0.06
CW-DR	—	—	2.2 ± 0.4	—
Ramsey-DR	—	—	3.95 ± 0.25	3.20 ± 0.01
ODSE	—	4.3 ± 0.85	—	3.21 ± 0.05
Estimation	4.5	4.5	—	—

4.7 Conclusion

We developed the Optically-Detected Spin-Echo (ODSE) method to determine the population and coherence relaxation times in a thermal Rb vapor with buffer-gas in view of its application to atomic clocks. We demonstrated that the ODSE method delivers the population relaxation time for all m_F levels of ^{87}Rb ground states and the intrinsic coherence relaxation time specifically for the clock transition of the ^{87}Rb atoms. We confirmed that the ODSE method suppresses the coherence relaxation arising from C-field inhomogeneity (in the $\vec{z}$ direction) across the vapor cell and thus yields intrinsic coherence relaxation time closer to the theoretically predicted T_2. This method was compared to other well-established methods, including Franzen, CW-DR and Ramsey-DR using the same ^{87}Rb vapor cell. The population relaxation time measured with the ODSE method was very consistent with those with the Franzen and Ramsey-DR methods. By contrast, the measured coherence relaxation times with both CW-DR and Ramsey-DR methods were shorter than the predicted T_2 due to C-field inhomogeneity.

Our proof-of-principle demonstrations show that ODSE is a highly useful method for measuring intrinsic relaxation rates in atomic vapors, independently of present magnetic field gradients. Contrary to NMR spin-echo, the ODSE method does not require any pickup-coil but uses a photodetector to record the light absorbed in the vapor cell (optical density). This is more robust and less noisy (allows a better signal-to-noise-ratio) than detection in the radio-frequency or microwave regime. Moreover, the photodetector can be conveniently placed outside the atomic vapor system under study, indicating that the ODSE method is an ideal candidate for characterizing relaxation times in atomic clocks with a cavity. Similarly, the ODSE method is of high interest for characterizing relaxation rates in other quantum optics systems with optical readout, such as quantum information storage or processing, cold-atom experiments, and other applications of quantum systems that rely on long-live atomic coherences.

5 Summary, Conclusion & Next Steps

5.1 Summary

In this thesis, we developed a high-performance Rb vapor cell atomic clock operating in the Ramsey-DR scheme, using a highly compact magnetron-type microwave cavity in the context of future industrial applications in navigation systems and telecommunications. The magnetron-type microwave cavity in our Rb atomic clock setup has a volume of only 45 cm^3 with a relatively low quality factor ($\approx$ 150). This cavity was designed and developed at the LTF in collaboration with the LEMA-EPFL. We demonstrated a short-term stability of $2.4 \times 10^{-13}\tau^{-1/2}$ in our Rb atomic clock. In addition, we estimated the clock frequency stability of $\sigma_y(\tau) \approx 9.8 \times 10^{-15}$ in medium- to long-term scales for our Ramsey-DR Rb clock based on the quantitative measurements of relevant instability sources. In the following, we present the main achievements of this thesis.

5.1.1 Setup Design

The physics package of our Rb atomic clock with a total volume of 0.8 dm^3 contained a compact magnetron-type microwave cavity [36] of only 45 cm^3 external volume with a relatively low quality factor Q $\approx$ 150. A newly in-house-developed vapor cell was mounted in the microwave cavity confines ^{87}Rb atoms and two buffer gases of nitrogen and argon. The vapor cell had a stem, a reservoir for Rb atoms, with a volume of $\approx$5 mm^3, which was ten times smaller than the previous version [35]. We obtained a stem temperature coefficient of $TC_{stem} \approx 1 \times 10^{-12}$ for our vapor cell. This result is one order of magnitude lower than for th one used in Bandi et al. [35], which was a limiting instability factor in their work in medium- to long-term scales, and two orders of magnitude lower than for the one used in Calosso et al. [94].

5.1.2 Spectroscopy

A relative C-field inhomogeneity of approximately 2% was estimated in the vapor cell based on the broadening of the Zeeman lines with CW-DR measurements. For the magnetron-type microwave cavity, a field orientation factor was measured at approximately 92%, which describes a highly uniform microwave field distribution inside the cavity. In addition, the microwave field uniformity was re-evaluated based on Rabi oscillations. A decay of approximately 15% of the amplitude of Rabi oscillations (which is the contrast of Ramsey central fringe) over the microwave pulse area from $\theta = \pi/2$ to $\theta = 3\pi/2$ indicated a good microwave field uniformity across the vapor cell. Both of these results (from FOF and Rabi oscillations) proved that our magnetron-type microwave cavity was a suitable candidate to be used in an atomic clock operating in the Ramsey-DR scheme.

The Rb clock was operated in the Ramsey-DR scheme in a laboratory ambient environment. A high-contrast Ramsey pattern was obtained by optimizing various parameters such as durations and intensities of optical and microwave pulses. The Ramsey pattern with a central fringe contrast up to 35% and a linewidth of 160 Hz was achieved.

5.1.3 Clock Short-Term Stability

For our Rb clock, the shot-noise limit was estimated below $1.7 \times 10^{-14}\tau^{-1/2}$. We measured the short-term stability of approximately $2.4 \times 10^{-13}\tau^{-1/2}$, comparable with the state-of-the-art stability performances for POP scheme using a large microwave cavity with a high quality factor [34] and from the CW-DR scheme [35]. We developed a new analytical expression to estimate the short-term stability of the atomic clock operating in the Ramsey-DR scheme [73]. With this formula, we estimated the short-term stability at the level of approximately $2.2 \times 10^{-13}\tau^{-1/2}$ for our Rb clock, which is in good agreement with the experimental results. In addition, we used this formula to find the optimized Ramsey time $2 < T_R < 3$ ms for our Ramsey-DR Rb clock. In our formula, contrary to the existing expressions, the duration of the optical detection pulse was also considered. The stability performance in our Rb clock demonstrated that a vapor cell clock operating in the Ramsey-DR scheme does not necessarily require a microwave cavity with a high quality factor to achieve state-of-the-art stability performance. We showed that the optical detection noise during the detection phase of the Ramsey-DR scheme was the dominant source of the instability in the short-term scale. This noise originated from the FM-to-AM noise conversion in the vapor cell and the AM noise from the acousto-optic modulator (AOM).

5.1.4 Light Shift and Microwave Power Shift

The light shift effect was quantified in our Rb atomic clock. The intensity LS and frequency LS coefficients, α_{LS} and β_{LS}, respectively, were measured when the clock was operating in CW-DR and Ramsey-DR schemes. The β_{LS} obtained in the Ramsey-DR scheme was more than two orders of magnitude lower than the one in CW-DR scheme, while the α_{LS} was only reduced by five times in Ramsey-DR compared to the CW-DR scheme. Our investigations on the LS effects proved that the non-zero α_{LS} in the Ramsey-DR scheme originated from a residual light during the Ramsey time due to non-perfect light suppression. Finally, in our Ramsey-DR Rb atomic clock, we estimated relative induced instabilities approximately at the levels of 10^{-15} and 10^{-16} from the intensity LS and the frequency LS, respectively.

Our investigations on the induced instabilities in medium- to long-term scales proved that, the microwave power shift represented the highest contribution to the clock frequency stability comparing to the other shifts. It was estimated at the level of 10^{-14} at $\tau = 10^4$ s. However, we found that this instability can be suppressed notably (about one order of magnitude) by varying the operating conditions as follows: 1) stabilizing the laser frequency to an $F = 2$ transition of the D2 line of ^{87}Rb, 2) adjusting the microwave power to reach a microwave pulse area of $\theta \approx 1.1 \cdot \pi/2$.

5.1.5 Optically-Detected Spin-Echo Method and T_2

We developed the experimental method of Optically-Detected Spin-Echo (ODSE), inspired by classical nuclear magnetic resonance spin-echo, to determine both ground-state population and coherence relaxation times of ^{87}Rb atoms in a buffer gas vapor cell. This study was done at LTF in collaboration with the Physics Institute of Belgrade University. The ODSE method was shown to suppress the decoherence relaxation arising from C-field inhomogeneity across the vapor cell, thus enabling the assessment of the "intrinsic" coherence relaxation time T_2 specifically for the clock transition of ^{87}Rb atoms. In our vapor cell, the relative C-field inhomogeneity was measured at approximately 2%. Our proof-of-principle demonstrations confirmed that the T_2 obtained from the ODSE method is independent from the presence of the C-field gradients across the cell and was in good agreement with the predicted T_2 based on the theory presented in [9]. In our ODSE method, the optical detection was conducted by a photodetector that was placed outside the clock system under test. Therefore, this method is of high interest for characterizing T_2 in solid-state quantum optics systems with optical signal read-out, such as quantum memory [116] and nitrogen-vacancy center in diamond [114] for applications in quantum information, quantum sensing and quantum metrology [115, 117].

5.2 Future Work

5.2.1 New Setup Design

The LS measurements demonstrated that the intensity LS was not suppressed sufficiently in the Rb clock operating in the Ramsey-DR scheme due to the non-perfect background light suppression in the LH. Therefore, redesigning the laser head in view of reducing the residual light through the AOM could be helpful to reduce the LS effect and improve the clock stability. In view of practical applications, the additive-manufacturing of microwave cavities with complex geometries is less expensive, faster and simpler prototyping, than their conventional-manufacturing [119].

5.2.2 Light Shifts and Microwave Shift Analysis

Experimental and theoretical investigations on the LS and microwave shift are required to further improve the medium- to long-term stability of our Rb atomic. In this context, further optimizations of optical and microwave parameters, such as their intensities and durations, are necessary. In view of suppressing the LS effect, an alternative line for further optimizing the working parameters is to measure the LS in each of the three sequences of optical pumping, optical detection and microwave interrogation including the Ramsey time (i.e., the residual light) separately with respect to the various laser locking frequencies.

5.2.3 New Schemes

New possible lines of investigation to support the future of the Ramsey-DR Rb clock can be achieved by are modifying the Ramsey-DR scheme to suppress the induced shifts and improving the medium- to long-term stability of the clock. Recently, various modified Ramsey schemes such as "hyper-Ramsey" [120], "modified-hyper-Ramsey" [121] and "auto-balanced Ramsey spectroscopy" [122, 123] have shown positive signs in the field of optical clocks. However, [124] has shown that, despite the advantages of these hyper-Ramsey schemes, they are sensitive to decoherence relaxations. Therefore, it may be possible to apply these modified Ramsey schemes to the vapor cell Rb clock and combine them with the ODSE scheme to suppress at least part of this decoherence effect.

A CAD Designs of Physics Package and Magnetron-Type Microwave Cavity

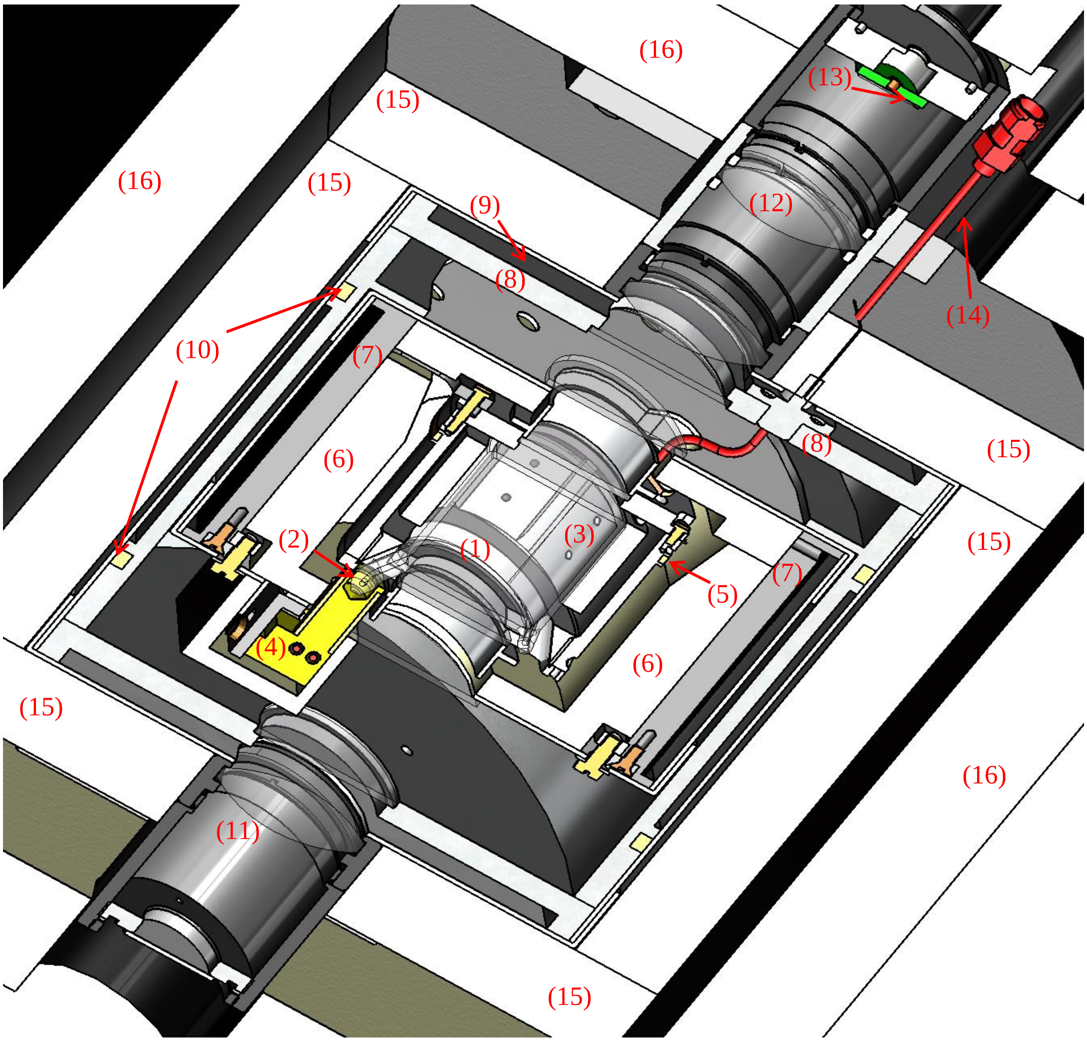

Figure A.1: CAD diagram of the completely assembled physics package, (1) cell-body with 25 mm diameter and 25 mm length; (2) cell-stem (reservoir) with 2.5 mm length; (3) magnetron-type microwave cavity with six electrodes; (4) heater and temperature control NTCs for the stem; (5) heater and temperature control NTCs for the cell body; (6) polyethylene foam; (7) C-field coils; (8) Aluminum holder for uniform thermal gradient; (9) μ-metal shields; (10) external control heaters; (11) telescope assembly; (12) focusing assembly; (13) photodetector; (14) co-axial cable; (15) polyethylene foam; and (16) polystyrene insulator.

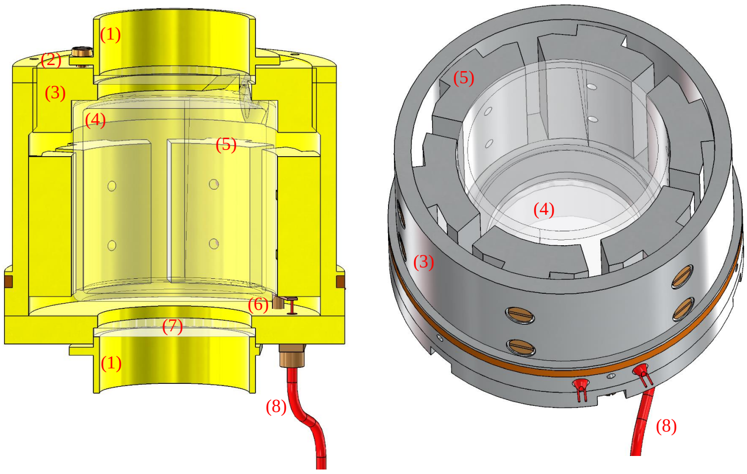

Figure A.2: CAD diagram of the magnetron-type microwave cavity with six electrodes, side view (right) and top view (left), (1) cut-offs; (2) cavity cap; (3) cavity body; (4) vapor cell; (5) electrode; (6) microwave cavity coupling loop; (7) focusing lens; (8) co-axial cable.

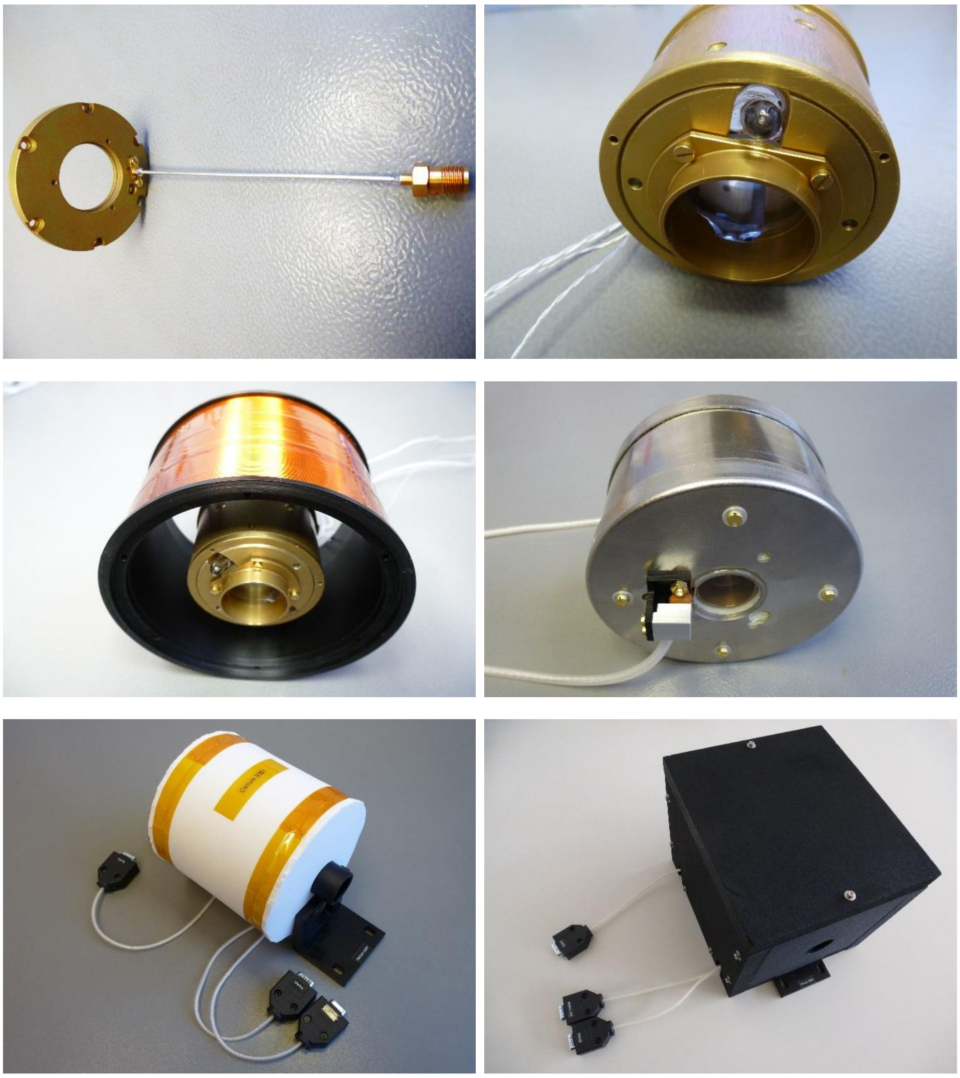

Figure A.3: Physics package assembly with the vapor cell, microwave cavity, C-field coils, μ-metal shields, polyethylene foam and polystyrene insulator.

B External Pressure Shift

At the time of writing this manuscript, a detailed study was being done by William Moreno from the LTF on the "Barometric effect in vapor cell atomic clocks" [125]. His achievements motivated us to measure this effect in our Rb clock as well. The atmospheric pressure variations deform the dimensions of the Rb vapor cell and change the density of the buffer gases [126, 127].

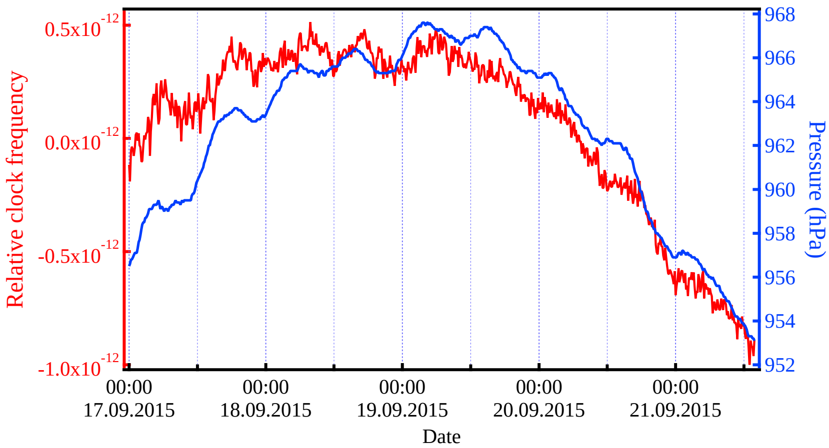

Figure B.1: The clock frequency and the atmospheric pressure over running the clock of $\approx$ 4.5 days.

In this section, we present our observation of the impact of the external atmospheric pressure on the clock frequency. We mentioned earlier that our Rb clock setup was placed in the ambient laboratory, therefore the natural daily atmospheric pressure fluctuations influence clock instability. We operated our Rb clock approximately for 4.5 days and recorded its frequency and the atmospheric pressure simultaneously. The atmospheric pressure was obtained from national Swiss weather station situated close to the laboratory (Longitudinal/Lateral E6°57′/N47°00′). Figure B.1 shows the clock frequency and the atmospheric pressure over a period of running the clock ($\approx$ 4.5 days). In this figure, a clear correlation between the atmospheric pressure and the clock frequency is visible. To estimate a pressure-shift coefficient in our measurement we plotted the clock frequency versus the atmospheric pressure in figure B.2. We estimated a pressure-shift coefficient at the level of $7.5(1) \times 10^{-14}$/hPa by averaging the coefficients measured from the two linear fits to the data shown in figure B.2. With these measurements, we estimated induced instabilities from the atmospheric pressure approximately at the level of 4×10^{-13} during our measurements considering the pressure variation of about 5 hPs. We have to take into account that the pressure variation can be increased up to some tens of hPs in various periods of the year.

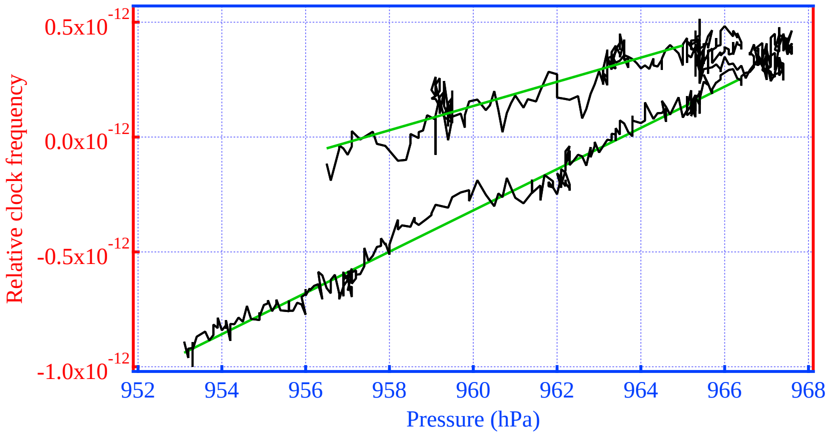

Figure B.2: The clock frequency versus the atmospheric pressure.

C POP Microwave Cavity

Following a first preliminary assembly of the cell-cavity system presented in section 2.3.2, we developed and built the final integration of the cavity with a vapor cell at the LTF. The tuning of the cavity's resonance frequency to the required ≈ 6.835 GHz atomic reference transition was performed while monitoring the resonance behavior (S11 parameter). The assembled and frequency-tuned cell-cavity system is shown in figure C.1.

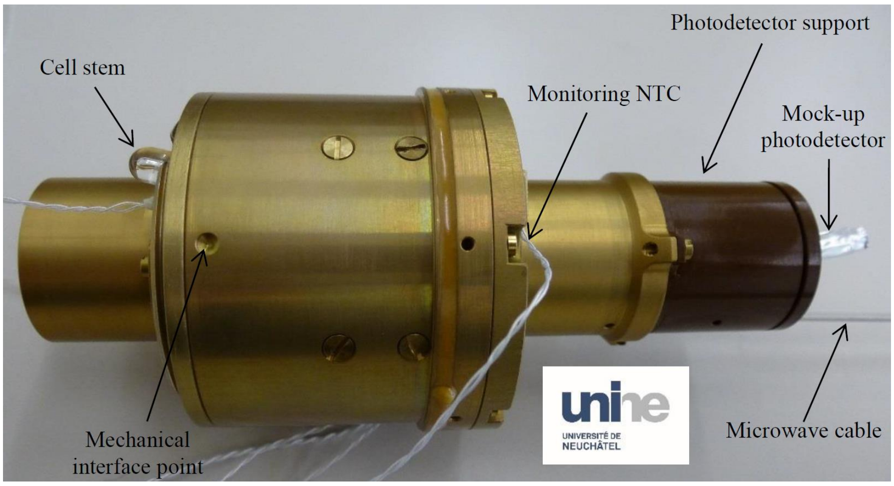

Figure C.1: Photograph of the integrated cell-cavity system.

The assembled cell-cavity system was submitted to testing of the microwave properties. These tests were performed over a range of few selected temperatures, including the 65°C expected operating temperature for the Ramsey-DR clock. For these tests, both a setup similar to the one shown in figure 2.14 as well as a Vector Network Analyser were used. The measured resonance spectrum is shown in figure C.2, for a cell and cavity temperature of 65°C. It clearly shows the required resonance at ≈ 6.834 GHz, with a resonance width on the order of about 90 MHz thus corresponding to a quality factor of

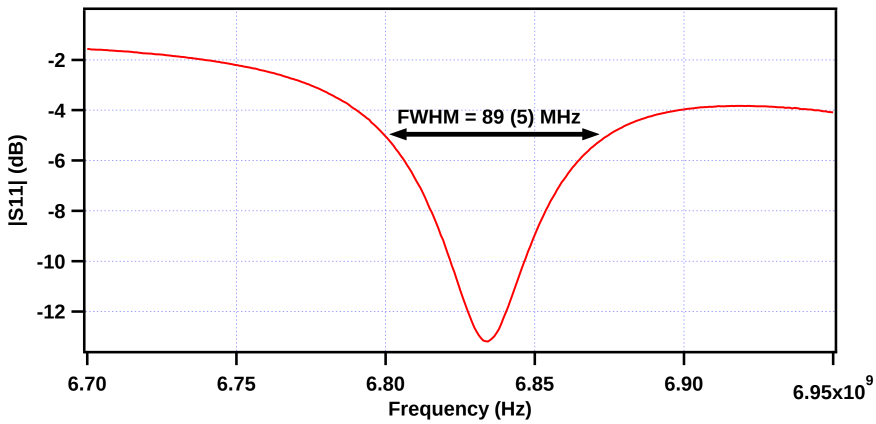

Figure C.2: Measured resonance spectrum for the cell-cavity system. Cavity temperature is 65°C.

$Q \approx 80$. At resonance, the coupling is measured to be $\mid S11 \mid \approx -12\,\text{dB}$, corresponding to an impedance of the cavity of about 53Ω.

By varying the temperature of the cell-cavity system and measuring precisely the center frequency of the cavity's resonance, we measured the temperature tuning coefficient for the cavity resonance. The result shown in Figure 4 shows a temperature coefficient of $\approx -33 \pm 2\,\text{kHz/°C}$. This small coefficient is advantageous for achieving small clock instability contributions from cavity pulling. We can estimate a temperature sensitivity of the clock frequency due to cavity pulling of about -5.7×10^{-14}/°C. The field orientation factor of this cavity was measured about 80% with the procedure explained in section 2.3.2.3 and equation (2.4).

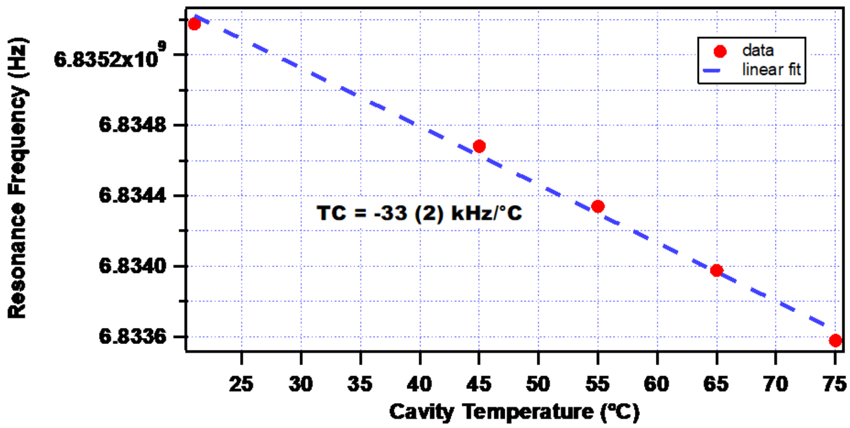

Figure C.3: Temperature tuning of the cavity resonance at 6.835 GHz. Error bars for the frequency data are on the level of 20 kHz, thus smaller than the data symbols here.

Bibliography

[1] E. Bava, M. Kühne and A.M. Rossi. *"Metrology and Physical Constants"*. IOS PRESS and SOCIETÀ ITALIANA DI FISICA, proceedings of the international school of physics "enrico fermi", 17-27 july 2012 edition, 2013.

[2] T. P. Heavner M. A. Lombardi and S. R. Jefferts. "nist primary frequency standards and the realization of the si second". *The Journal of Measurement Science*, 2(4), 2007.

[3] J. Curie and P. Curie. "Development, via compression, of electric polarization in hemihedral crystals with inclined faces". *Bulletin de la Société minéralogique de France*, 3(90-93).

[4] W. A. Marrison and J. W. Horton. "Precision determination of frequency". *I. R. E. Proc.*, 16(137-154), Feb. 1928.

[5] C. Cohen Tannoudji. "Quantum Mechanics". *Hermann and John Wiley and Sons. Inc.*, 1977.

[6] P. Kusch I. I. Rabi, S. Millman and J. R. Zacharias. "the molecular beam resonance method for measuring nuclear magnetic moments". *Phys. Rev.*, 55(526-535), 1939.

[7] I. I. Rabi. "Radiofrequency Spectroscopy". *In Richtmyer Memorial Lecture, delivered at Columbia University in New York, New York, volume 67 of Meeting at New York, January 19 and 20, 1945, Phys. Rev.*, (199-204), 1945.

[8] L. Essen and J. V. L. Parry. "an atomic standard of frequency and time interval". *Nature*, 176(280-286), 1955.

[9] J. Vanier and C. Audoin. *"The Quantum Physics of Atomic Frequency Standards"*. (Adam Hilger, 1989.

[10] R. Wynands and S. Weyers. "Atomic fountain clocks". *Physical Review*, 42(S64), 2005.

[11] P. Waller, S. Gonzalez, S. Binda, I. Sesia, I. Hidalgo, G. Tobias and P. Tavella. "The in-orbit performances of GIOVE clocks". *IEEE Trans. Ultrason. Ferroelctr. Freq. Control.*, 57(738), 2010.

[12] G. Busca, L.-G. Bernier and P. Rochat. "Active hydrogen maser frequency standard". *United States Patent*, 5(838), Nov. 1998.

[13] J. Camparo. "The rubidium atomic clock and basic research". *Physics Today*, 66(33), 2007.

[14] C. Affolderbach, F. Droz and G. Mileti. "Experimental demonstration of a compact and high-performance laser-pumped rubidium gas cell atomic frequency standard". *IEEE Trans. Instrum. Meas.*, 55(429), 2006.

[15] M. Takamoto, F-L Hong, R. Higashi and H. Katori. "An optical lattice clock". *Nature*, 435(321–324), 2005.

[16] S. A. Diddams, Th. Udem, J. C. Bergquist, E. A. Curtis, R. E. Drullinger, L. Hollberg, W. M. Itano, W. D. Lee, C. W. Oates, K. R. Vogel and D. J. Wineland. "An optical clock based on a single trapped 199Hg ion". *Science*, 293(5531)(825–828), 2001.

[17] Y.-Y. Jau, H. Partner, P. D. D. Schwindt, J. D. Prestage, J. Kellogg and N. Yu. "Low-power, miniature ^{171}Yb ion clock using an ultra-small vacuum package". *Appl. Phys. Lett.*, 101(253518), 2012.

[18] P. Rochat, F. Droz, P. Mosset, G. Barmaverain, Q. Wang, D. Boving, L. Mattioni, M. Belloni, M. Gioia, U. Schmidt, T. Pike and F. Emma. "The onboard Galileo rubidium and passive maser, status and performance". *Proc. of the 2005 IEEE Int. Freq. Cont. Symp. and Expos.*, (26–32), 2005.

[19] A. Kastler. "Applications of polarimetry to infra-red and micro-wave spectroscopy". *Nature*, 166(4211), 1950.

[20] C. E. Wieman and L. Hollberg. "Using diode lasers for atomic physics". *Review of Scientific Instruments*, 20 (1)(1-20), 1991.

[21] R. T. Dupuis, T. J. Lynch and J. R. Vaccaro. " Rubidium Frequency Standard for the GPS IIF program and modifications for the RAFSMOD Program ". *Proc. 2008 IEEE International Freq. Control. Symp. (IEEE Press, Piscataway, NJ, 2008*, (pp. 655-660), 2008.

[22] Q. Hao, W. Li, S. He, J. Lv, P. Wang and G. Mei. "A physics package for rubidium atomic frequency standard with a short-term stability of $2.4 \times 10^{-12}\,\tau^{-1/2}$". *Review of Scientific Instruments*, 87(123111), 2016.

[23] J. Vanier and C. Mandache. "The passive optically pumped Rb frequency standard: the laser approach". *Appl. Phys. B*, 87(565-593), 2007.

[24] G. Mileti. *"Etude du pompage optique par laser et par lampe spectrale dans les horloges á vapeur de rubidium".*

[25] IND55 Mclocks European Metrology Research Programme (EMRP). "http://www.inrim.it/Mclocks/".

[26] J. Vanier. "Atomic clocks based on coherent population trapping: a review". *J. Appl. Phys. B*, 81(421), 2005.

[27] P. Yun, J. M. Danet, D. Holleville, S. Micalizio, E. Clercq and S. Guérandel. "Constructive polarization modulation for coherent population trapping clock". *App. Phys. Lett.*, 105(231106), 2014.

[28] P. Yun, J. M. Danet, S. Guérandel and E. Clercq. "Coherent population trapping with polarization modulation". *Jour. Appl. Phys.*, 119(244502), 2016.

[29] P. Yun, F. Tricot, C. E. Calosso, S. Micalizio, B. François, R. Boudot, S. Guérandel and E. Clercq. "High-performance Coherent Population Trapping clock with polarization modulation". *Phys. Rev. Applied*, 7(014018), 2017.

[30] Y. Sortais, S. Bize, M. Abgrall, S. Zhang, C. Nicolas, C. Mandache, P. Lemonde, P. Laurent, G. Santarelli, N. Dimarcq, P. Petit, A. Clairon, A. Mann, A. Luiten, S. Chang and C. Salomon. "Cold Atom Clocks". *Phys. Scr.*, 2001(50), 2000.

[31] F. X. Esnault, D. Holleville, N. Rossetto, S. Guérandel and N. Dimarcq. "High-stability compact atomic clock based on isotropic laser cooling". *Phys. Rev. A*, 82(033436), 2010.

[32] F. X. Esnault, N. Rossetto, D. Holleville and N. Dimarcq. "HORACE: A compact cold atom clock for Galileo". *Advances in Space Research*, 47(5), 2011.

[33] J. F. Schaff, R. Szmuk, M. Langlois, L. de Sarlo, D. Holleville, N. Dimarcq and B. Desruelle. "MuClock a Commercial Cold Atom Clock for Ground Applications". *Proc. 5th int. Galileo Science Colloquium, Braunschweig, Germany*, 2015.

[34] S. Micalizio, C. E. Calosso, A. Godone and F Levi. "Metrological characterization of the pulsed Rb clock with optical detection". *Metrologia*, 49(425-436), 2012.

[35] T. Bandi, C. Affolderbach, C. Stefanucci, F. Merli, A. K. Skrivervik and G. Mileti. " Compact high-performance continuous-wave double-resonance rubidium standard with $1.4\times10^{-13}\tau^{-1/2}$ stability". *IEEE Transactions on Ultrasonics, Ferroelectrics and Frequency Control*, 61(1769-1778), 2014.

[36] C. Stefanucci, T. Bandi, F. Merli, M. Pellaton, C. Affolderbach, G. Mileti and A. K. Skrivervik. "Compact microwave cavity for high performance rubidium frequency standards". *Rev. Sci. Instrum.*, 83(104706), 2012.

[37] W. Franzen. "Spin Relaxation of Optically Aligned Rubidium Vapor". *Phys. Rev.*, 115(850), 1959.

[38] A. Horsley, G. X. Du, M. Pellaton, C. Affolderbach, G. Mileti and P. Treutlein. "Imaging of relaxation times and microwave field strength in a microfabricated vapor cell". *Phys. Rev. A*, 88(063407), 2013.

[39] E. L. Hahn. "Spin Echoes". *Phys. Rev.*, 80(580), 1950.

[40] M. Gharavipour, C. Affolderbach, S. Kang, and G. Mileti. "Double-resonance spectroscopy in Rubidium vapour-cells for high performance and miniature atomic clocks". *IOP Conf. Series: Jour. of Phys.*, 793(012007), 2017.

[41] T. N. Bandi. *"Double resonance studies on compact ,high- performance rubidium cell frequency standards"*. Université de Neuchâtel- Institut de Physique - Laboratoire Temps-Fréquence, PhD Thesis, 2013.

[42] A. Godone , S. Micalizio and F. Levi. "Pulsed Optically Pumped Frequency Standard". *Phys. Rev. A*, 70(023409), 2004.

[43] A. Godone , S. Micalizio , C. E. Calosso and F. Levi. "The Pulsed Rubidium Clock". *IEEE Transactions on ultrasonics, ferroelectrics, and frequency control*, 53(3), 2006.

[44] N. F. Ramsey. "Molecular Beams". *Clarendon Press, Oxford*, 1956.

[45] D. A. Steck. "Rubidium 87 D line data". *[Online], Available: http://steck.us/alkalidata.*, 2007.

[46] D. A. Steck. "Rubidium 85 D line data". *[Online], Available: http://steck.us/alkalidata.*, 2007.

[47] G. Breit and I. I. Rabi. "Measurement of Nuclear Spin". *Phys. Rev.*, 38(2082-2083), 1931.

[48] A. Clairon , S. Bize , Y. Sortais , M. S. Santos , C. Mandache and C. Salomon. "High accuracy measurement of the Rb 87 ground-state hyperfine splitting in an atomic fountain". *Europhysics Letters*, 45(5), 1999.

[49] U. Fano. "Description of States in Quantum Mechanics by Density Matrix and Operator Techniques". *Rev. Mod. Phys.*, 29(74–93), 1957.

[50] A. Godone, F. Levi, and S. Micalizio. "Coherent Population Trapping Maser". *(CLUT Editrice, Torino, Italy 2002).*

[51] F. Riehle. *"Frequency Standards Basics and Applications".* Wiley-VCH Verlag Gmb H Co.KGaA, Weinheim, 1989.

[52] A. Kastler. "Optical methods for studying Hertzian resonances". *Science*, 158(3798), 1967.

[53] N. F. Ramsey. "A Molecular Beam Resonance Method with Separated Oscillating Fields". *Phys. Rev.*, 78(695), 1950.

[54] N. F. Ramsey. "Molecular beam resonances in oscillatory fields of nonuniform amplitudes and phases". *Phys. Rev.*, 109(822-825), 1958.

[55] F. Bloch. "nuclear induction". *Phys. Rev.*, 70(460), 1946.

[56] M. Fox. *"Quantum Optics An Introduction".* Oxford University Press Inc., New York, 2006.

[57] R. Feynman, F. Vernon and R. Hellwarth. "Geometrical representation of the Schördinger equation for solving Maser problems". *J. App. Phys.*, 28(49), 1957.

[58] C. O. Alley. "Coherent pulse techniques in the optical detection of the 0-0 ground state hyperfine resonance in ^{87}Rb". *Quantum Electronics*, C. W. Townes, Ed. New York: Columbia Univ. Press(146–155), 1960.

[59] M. Arditi and T. R. Carver. "Atomic clock using microwave pulse coherent techniques". *IEEE Trans. Instrum. Meas.*, 13(146–152), 1964.

[60] T. C. English, E. Jechart and T. M. Kwon. "The rubidium atomic clock and basic research". *Proceedings 10th Precise Time and Time Interval Forum, Washington, 1978, edited by L. J. Rueger (NASA, Maryland, 1979)*, (pp. 147–165), 1978.

[61] F. Levi, C. Novero, A. Godone and G. Brida. "Study of light shift in rubidium frequency standard". *IEEE Transactions on Instumentation and Measurements*, 46(216), 1997.

[62] T. Scholtes, S. Woetzel, R. IJsselsteijn, V. Schultze and H. G. Meyer. "Intrinsic relaxation rates of polarized Cs vapor in miniaturized cells". *Appl. Phys. B*, 117(211), 2014.

[63] J. Vanier J, J. F. Simard and J. S. Boulanger. "Relaxation and frequency shifts in the ground state of ^{85}Rb". *Phys. Rev. A*, 9(1031), 1974.

[64] P. J. Oreto, Y.-Y. Jau, A. B. Post, N. N. Kuzma and W. Happer. "Buffer-gas-induced shift and broadening of hyperfine resonances in alkali-metal vapors". *Phys. Rev. A*, 69(042716), 2004.

[65] W. Happer. "Optical pumping". *Reviews of Modern Physics*, 44(2)(169-249), 1972.

[66] S. Micalizio, A. Godone, F. Levi and J. Vanier. "Spin-exchange frequency shift in alkali-metal-vapor cell frequency standards". *Phys. Rev. A*, 73(033414), 2006.

[67] F. A. Franz and E. Lüsher. "Spin Relaxation of Optically Pumped Cesium". *Phys. Rev.*, 135(A582), 1964.

[68] F. A. Franz. "Rubidium Spin Relaxation in the Rare Gases Under Ultraclean Conditions". *Phys. Rev.*, 115(A603), 1965.

[69] D. W. Allan. "Statistics of Atomic Frequency Standards". *In Proceedings of theIEEE*, 54(221–230), 1966.

[70] W. Riley and D. A. Howe. "Handbook of Frequency Stability Analysis". *NIST Spec. Pubs.*, Jul. 2008.

[71] G. Santarelli, C. Audoin, A. Makdissi, P. Laurent, G. J. Dick and A. Clairon. "Frequency stability degradation of an oscillator slaved to a periodically interrogated atomic resonator". *IEEE Trans. Ultrason. Ferroelectr. Freq. Control*, 45(no. 4 pp. 887-894), 1998.

[72] J. C. Camparo. "Conversion of laser phase noise to amplitude noise in an optically thick vapor". *Journal of the Optical Society of America B*, 15(1177), 1998.

[73] S. Kang, M. Gharavipour, C. Affolderbach and G. Mileti. "Stability limitations from optical detection in Ramsey-type vapour-cell atomic clocks". *Electronics Letters*, 51 (22)(1767-1769), 2015.

[74] G. J. Dick. "Local oscillator induced instabilities in trapped ion frequency standards". *Proc. 19th Precise Time and Time Interval Meeting, Redondo Beach, CA*, (pp.133-147), 1987.

[75] G. J. Dick, J. D. Prestage, C. A. Greenhall and L. Maleki. "Local oscillator induced degradation of medium-term stability in passive atomic frequency standards". *Proc. 22nd Precise Time and Time Interval Meeting, Vienna, Virginia*, (pp. 487-508), 1990.

[76] J. Vanier, R. Kunski, N. Cyr, J. Savard and M. Tetu. "On hyperfine frequency shifts caused by buffer gases: application to the optically pumped passive rubidium frequency standard". *J. Appl. Phys.*, 53(8), 1982.

[77] S. Micalizio, A. Godone, F. Levi and J. Vanier. "Erratum: Spin exchange frequency shift in alkali-metal-vapor cell frequency standards". *Phys. Rev. A*, 74(059905), 2006.

[78] S. Micalizio, A. Godone, F. Levi and C. Calosso. "Medium-Long Term Frequency Stability of Pulsed Vapor Cell Clocks". *IEEE Transactions on Ultrasonics IEEE Transactions on Ultrasonics, Ferroelectrics, and Frequency Control*, 57(7), 2010.

[79] J. Vanier, A. Godone and F. Levi. "Coherent population trapping in cesium: Dark lines and coherent microwave emission". *Phys. Rev. A*, 58(3), 1998.

[80] A. Risley, S. Jarvis and J. Vanier. "The Dependence of Frequency Upon Microwave Power of Wall-coated and Buffer-gas-filled Gas Cell ^{87}Rb Frequency Standards". *J. Appl. Phys.*, 51(9)(4571–4576), 1980.

[81] G. Mileti, I. Ruedi and H. Schweda. "Line inhomogeneity effects and power shift in miniaturized rubidium frequency standards". *In Proc. of 6th European Frequency and Time Forum*, page 515, 1992.

[82] J. C. Camparo, C. M. Klimcak and S. J. Herbulock. "Frequency equilibration in the vapor-cell atomic clock". *IEEE Transactions on Instrumentation and Measurement*, 54(1873–1880), 1992.

[83] S. Micalizio, A. Godone, F. Levi and C. E. Calosso. "Pulsed optically pumped ^{87}Rb vapor cell frequency standard: A multilevel approach". *Phys. Rev. A*, 79(013403), 2009.

[84] C. Affolderbach, C. Andreeva, S. Cartaleva, T. Karaulanov, G. Mileti and D. Slavov. "Light-shift suppression in laser optically pumped vapour-cell atomic frequency standards". *Appl. Phys. B*, 80(841-848), 2005.

[85] J. P. Barrat and C. Cohen-Tannoudji. "Study of optical pumping and the density matrix formalism". *(J. Phys. Radium)*, 22(329), 1961.

[86] B. S. Mathur, H. Tang and W. Happer. *"Light shifts in the alkali atoms".* Physical Review, 11-19, 171 edition, 1968.

[87] M. Pellaton. *"High-Resolution Spectroscopic Studies in Glass-Blown and Micro-Fabricated Cells for Miniature Rubidium Atomic Clocks".* Université de Neuchâtel- Institut de Physique - Laboratoire Temps-Fréquence, PhD Thesis, 2014.

[88] F. Levi, J. Camparo, B. Francois, C. E. Calosso, S. Micalizio and A. Godone. "Precision test of the ac Stark shift in a rubidium atomic vapor". *Phys. Rev. A*, 93(023433), 2016.

[89] F. Gruet, M. Pellaton, C. Affolderbach, T. Bandi, R. Matthey and G. Mileti. "Proc. of International conference on Space Optics (ICSO), 9-12th, October 2012". (no. 48), 2012.

[90] C. E. Calosso, S. Micalizio, A. Godone, E. K. Bertacco and F. Levi. "Electronics for the pulsed rubidium clock:design and characterization". *IEEE Trans. Instrum. Meas.*, 54(1731–1740), 2007.

[91] T. W. Hänsch, I. S. Shahin and A. L. Schawlow. "High-Resolution Saturation Spectroscopy of the Sodium D Lines with a Pulsed Tunable Dye Laser". *Phys. Rev. Lett.*, 27(707–710), 1971.

[92] A. L. Schawlow. "Spectroscopy in a new light". *Rev. Mod. Phys.*, 54(697-709), 1982.

[93] O. Schmidt, K.-M. Knaak, R. Wynands and D. Meschede. "Cesium saturation spectroscopy revisited: How to reverse peaks and observe narrow resonances". *Appl. Phys. B*, 59(167-178), 1994.

[94] C. E. Calosso, A. Godone, F. Levi and S. Micalizio. "Enhanced temperature sensitivity in vapor-cell frequency standards". *IEEE Trans. Ultrason. Ferroelctr. Freq. Control.*, 59(12), 2012.

[95] A. Godone, S. Micalizio, F. Levi and C. Calosso. "Microwave cavities for vapor cell frequency standards". *Rev. Sci. Instrum.*, 82(074703), 2011.

[96] W. Francisz and J. S. Hyde. "The loop-gap resonator: a new microwave lumped circuit ESR sample structure". *Journal of Magnetic Resonance*, 47(515-521), 1982.

[97] G. A. Rinard and G. R. Eaton. "Biomedical EPR - Part B: Methodology, Instrumentation and Dynamics". *Springer USA*, 24/B, 2005.

[98] W. N. Hardy and L. A. Whitehead. "Split-ring resonator for use in magnetic resonance from 200-2000 MHz". *Rev. Sci. Instrum.*, 52 (2)(213–216), 1981.

[99] S. An B. Xia, D. Zhong and G. Mei. "Characteristics of a novel kind of miniaturized cavity-cell assembly for rubidium frequency standards". *IEEE Trans. on Instrum. and Measurement*, 55(pp. 1000-1005), 2006.

[100] L. Guo-Bin, Z. Feng and G. Si-Hong. "Study of a low power dissipation, miniature laserpumped rubidium frequency standard". *Chinese Physics B*, 18 (9)(pp. 3839–3843), 2009.

[101] A. E. Ivanov. *"Study and Development of a Microwave Cavity for Atomic Clock Applications"*. Ecole Polytechnique Fédérale de Lausanne (EPFL)- Laboratory of Electromagnetics and Acoustics (LEMA), PhD Thesis, 2018.

[102] S. Micalizio, C. E. Calosso, F. Levi and A. Godone. "Ramsey-fringe shape in an alkali-metal vapor cell with buffer gas". *Phys. Rev. A*, 88(033401), 2013.

[103] S. Kang, M. Gharavipour, C. Affolderbach, F. Gruet and G. Mileti. "Demonstration of a high-performance pulsed optically pumped Rb clock based on a compact magnetron-type microwave cavity". *J. Appl. Phys*, 117(104510), 2015.

[104] M. Gozzelino, S. Micalizio, F. Levi, A. Godone and C. E. Calosso. "Reducing cavity-pulling shift in Ramsey-operated compact clocks". *Accepted for publication by IEEE UFFC*, 10.1109/TUFFC.2018.2828987, 2018.

[105] D. Budker, W. Gawlik, D. F. Kimball, S. M. Rochester, V. V. Yashchuk and A. Weis. "Resonant nonlinear magneto-optical effects in atoms". *Rev. Mod. Phys.*, 74(1153), 2002.

[106] H. Y. Carr and E. M. Purcell. "Effects of Diffusion on Free Precession in Nuclear Magnetic Resonance Experiments". *Phys. Rev.*, 94(no. 3, pp. 630), 1954.

[107] M. Gharavipour, C. Affolderbach, F. Gruet, I. S. Radojičić, A. J. Krmpot, B. M. Jelenković and G. Mileti. "Optically-detected spin-echo method for relaxation times measurements in a Rb atomic vapor". *New J. Phys.*, 19(063027), 2017.

[108] H. C. Torrey. "Bloch Equations with Diffusion Terms". *Phys. Rev.*, 104(no. 3 pp. 563–565), 1956.

[109] P. Stilbs. "Fourier Transform Pulsed-Gradient Spin-Echo Studies of Molecular Diffusion". *Progress in NMR Spectroscopy*, 19(1-45), 1987.

[110] S. Meiboom and D. Gill. "Modified Spin-Echo Method for Measuring Nuclear Relaxation Times". *Rev. Sci. Instrum.*, 29(688), 1958.

[111] N. Bar-Gill, L. M. Pham, A. Jarmola, D. Budker and R. L. Walsworth. "Solid-State Electronic Spin Coherence Time Approaching One Second". *Nat. Commun.*, 4(1743), 2013.

[112] J. S. Hodges, N. Y. Yao, D. Maclaurin, C. Rastogi, M. D. Lukin and D. Englund. "Timekeeping With Electron Spin States in Diamond". *Phys. Rev. A*, 87(032118), 2013.

[113] L. Viola and S. Lloyd. "Dynamical Suppression of Decoherence in Two-State Quantum Systems". *Phys. Rev. A*, 58(4), 1998.

[114] J. H. Shim, I. Niemeyer, J. Zhang and D. Suter. "Robust Dynamical Decoupling for Arbitrary Quantum States of a Single NV Center in Diamond". *Europhys. Lett.*, 99(4), 2012.

[115] M. Hosseini, B. M. Sparkes, G. Campbell, P. K. Lam and B. C. Buchler. "High Efficiency Coherent Optical Memory With Warm Rubidium Vapour". *Nat. Commun.*, 2(174), 2011.

[116] B. Julsgaard, A. Kozhekin and E. S. Polzik. "Experimental long-lived entanglement of two macroscopic objects". *Nature*, 413(400), 2001.

[117] S. Kröll, S. A. Moiseev W. Tittel, M. Afzelius, T. Chaneliére, R. L. Cone and M. Sellars. "Photon-Echo Quantum Memory in Solid State Systems". *Laser Photon. Rev.*, 4(244-67), 2010.

[118] C. Laplane, P. Jobez, J. Etesse, N. Timoney, N. Gisin and M. Afzelius. "Multiplexed on-Demand Storage of Polarization Qubits in a Crystal". *New J. Phys.*, 18(013006), 2016.

[119] C. Affolderbach, W. Moreno, A. E. Ivanov, T. Debogovic, M. Pellaton, A. K. Skrivervik, E. de Rijk, and G. Mileti. "Study of Additive Manufactured Microwave Cavities for Pulsed Optically Pumped Atomic Clock Applications". *Appl. Phys. Lett.*, 112(113502), 2018.

[120] Ch. Lisdat V. I. Yudin, A. V. Taichenachev, C. W. Oates, Z. W. Barber, N. D. Lemke, A. D. Ludlow, U. Sterr and F. Riehle. "Hyper-Ramsey spectroscopy of optical clock transitions". *Phys. Rev. A*, 82(011804), 2010.

[121] R. Hobson, W. Bowden, S. A. King, P. E. G. Baird, I. R. Hill and P. Gill. "Modified hyper-Ramsey methods for the elimination of probe shifts in optical clocks". *Phys. Rev. A*, 93(010501), 2016.

[122] C. Sanner, N. Huntemann, R. Lange, C. Tamm and E. Peik. "Auto-Balanced Ramsey Spectroscopy". *Phys. Rev. A*, arXiv:1707.02630 physics.atom-p], 2017.

[123] T. Zanon , R. Lefevre, A. V. Taichenachev and V. I. Yudin. "Universal interrogation protocol with zero probe-field-induced frequency shift for quantum clocks and high-accuracy spectroscopy". *Phys. Rev. A*, 96(023408), 2017.

[124] V. I. Yudin, A. V. Taichenachev, M. Yu. Basalaev and T. Zanon-Willette. "Synthetic frequency protocol for Ramsey spectroscopy of clock transitions". *Phys. Rev. A*, 94(052505), 2016.

[125] W. Moreno, C. Affolderbach, M. Pellaton and G. Mileti. "Barometric effect in vapor cell atomic clocks". *IEEE Trans. Ultrason., Ferroelectr., Freq. Control*, DOI: 10.1109/TUFFC.2018.2844020, 2018.

[126] W. J. Riley. "The Physics of the Environmental Sensitivity of Rubidium Gas Cell Atomic Frequency Standards". *IEEE Trans. Ultrason., Ferroelectr., Freq. Control*, 39 (2)(232-240), 1992.

[127] M. Huang, C. M. Klimcak and J. C. Camparo. "Vapor-cell clock frequency and environmental pressure: Resonance-cell volume changes". *IEEE IFCS, Newport Beach, CA, USA,*, (208-211), 2010.

Publications:

Peer-reviewed articles:

1. M. M. Ćurčić, T. Khalifa, B. Zlatković, I. S. Radojičić, A. J. Krmpot, D. Arsenović, B. M. Jelenković, and M. Gharavipour "Four-wave mixing in potassium vapor with an off-resonant double- Λ system" *Phys. Rev. A* 97 063851, 2018.

2. M. Gharavipour, C. Affolderbach, F. Gruet, I. S. Radojičić, A. J. Krmpot, B. M. Jelenković and G. Mileti "Optically-detected spin-echo method for relaxation times measurements in a Rb atomic vapor" *New Journal of Phys.* 19 063027, 2017.

3. M. Gharavipour, C. Affolderbach, S. Kang and G. Mileti "Double-resonance spectroscopy in Rubidium vapour-cells for high performance and miniature atomic clocks" *Journal of Physics: Conf. Series* 793 012007 2017.

4. M. Gharavipour, C. Affolderbach, S. Kang, T. Bandi, F. Gruet, M. Pellaton and G. Mileti "High performance vapour-cell frequency standards" *Journal of Physics: Conf. Series* 723 012006, 2016.

5. S. Micalizio, F. Levi, A. Godone, C. E. Calosso, B. François, R. Boudot, C. Affolderbach, S. Kang, M. Gharavipour, F. Gruet and G. Mileti "Pulsed Optically Pumped Rb clock" *Journal of Physics: Conf. Series* 723 012015, 2016.

6. S. Kang, M. Gharavipour, C. Affolderbach, G. Mileti. "Stability limitations from optical detection in Ramsey-type vapour-cell atomic clocks", *Electronics Letters* 51, issue 22, 1767 2015.

7. S. Kang, M. Gharavipour, C. Affolderbach, F. Gruet and G. Mileti. "Demonstration of a high-performance pulsed optically pumped Rb clock based on a compact magnetron-type microwave cavity", *Journal of Applied Physics* 117 104510, 2015.

8. K. Forghani, M. Gharavipour, M. Klein, F. Scholz, O. Klein, U. Kaiser, M. Feneberg, B. Neuschl and K. Thonke. "In-Situ deposited SiN_x nanomask for crystal quality improvement in AlGaN", *Physica Status Solidi C*, 8 2063 2011.

Conference proceedings:

1. M. Gharavipour, C. Affolderbach, F. Gruet, I. S. Radojičić, A. J. Krmpot, B. M. Jelenković and G. Mileti. "Impact of Static-Magnetic-Field-Gradients on Relaxation Times in a Rb Vapor Cell", Proceeding Paper European Frequency and Time Forum & International Frequency Control Symposium EFTF-IFCS, 2017, Besançon, France.

2. S. Kang, M. Gharavipour, F. Gruet, C. Affolderbach, G. Mileti. "Compact and high-performance Rb clock based on pulsed optical pumping for industrial application", Proceeding Joint Conference of the IEEE International Frequency Control Symposium & European Frequency and Time Forum (EFTF), 2015, Denver, Colorado, USA.

3. S. Kang, C. Affolderbach, F. Gruet, M. Gharavipour, C. E. Calosso, G. Mileti. "Pulsed optical pumping in a Rb vapor cell using a compact magnetron-type microwave cavity", Proceeding Paper European Frequency and Time Forum (EFTF), 2014, Neuchâtel, Switzerland.

4. K. Forghani, M. Gharavipour, F. Scholz, K. Thonke. "Investigations on Si-doped AlGaN: Below and above the Mott density", Physica Status Solidi C, DOI: 10.1002/pssc.201100481 (ICNS proceeding) 2011.

Conference contribution:

1. M. Gharavipour, I. S. Radojičić, F. Gruet, C. Affolderbach, A. J. Krmpot, B. M. Jelenković and G. Mileti "Impact of Static-Magnetic-Field-Gradients on Relaxation Times in a Rb Vapor Cell" European Frequency and Time Forum & International Frequency Control Symposium EFTF-IFCS July 2017, Besançon, France (Talk & Poster, *Student poster finalist*).

2. M. Gharavipour, I. S. Radojičić, F. Gruet, C. Affolderbach, A. J. Krmpot, B. M. Jelenković and G. Mileti "Comparison of the measured relaxation times with different methods in an Rb vapor-cell" Swiss Physical Society SPS Annual Meeting 23rd – 25th August 2016, Lugano, Switzerland (Talk).

3. M. Gharavipour, I. S. Radojičić, F. Gruet, C. Affolderbach, A. J. Krmpot, B. M. Jelenković and G. Mileti "Relaxation time measurements in a Rb vapour cell" European Frequency and Time Forum (EFTF), April 2016, York, United Kingdom (Talk).

4. M. Gharavipour, I. S. Radojičić, F. Gruet, C. Affolderbach, A. J. Krmpot, B. M. Jelenković and G. Mileti "Light Shifts Studies in CW and Ramsey Double Resonance Vapor Cell Frequency Standards", European Frequency and Time Forum (EFTF), April 2016, York, United Kingdom (Poster, *Student poster finalist*).

5. M. Gharavipour, A. E. Ivanov, C. Affolderbach, A. Skrivervik and G. Mileti "Microwave Cavity Characterization for Rubidium Frequency Standards", European Frequency and Time Forum (EFTF), April 2016, York, United Kingdom (Poster).

6. K. Forghani, M. Gharavipour, F. Scholz, K. Thonke, O. Klein and U. Kaiser. "Detailed Studies of Si-doped AlGaN Films Grown by MOVPE", International Conference on Nitride Semiconductors (ICNS), July 2011, Glasgow, Scotland. (Poster)

7. K. Forghani, M. Gharavipour, M. Klein, F. Scholz, O. Klein, U. Kaiser, M. Feneberg, B. Neuschl, K. Thonke. "In-Situ deposited SiN_x nanomask for crystal quality improvement in AlGaN", International Workshop on Nitride Semiconductors (IWN), September 2010, Tampa, Florida, USA. (Talk)

Mohammadreza Gharavipour

Rue des parcs 47
CH-2000 Neuchâtel
Switzerland

+41 79 3251555
mohammadreza.gharavipour@unine.ch

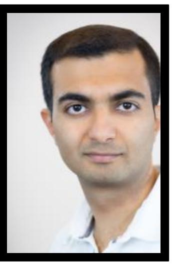

Personal

Date of Birth	12 August 1983
Nationality	Iranian
Family Status	Married, One child
Languages	English, Deutsch (B1) and Persian (native)

Education

2014 – 2018 **Ph.D. in Physics**
Physics Department, University of Neuchâtel, Switzerland

2008 – 2011 **M. Sc. in Advanced Materials (Nano-technology)**
University of Ulm, Germany

2001 – 2006 **B. Sc. in Physics (Atomic-Molecular)**
Iran University of Science and Technology (IUST), Tehran, Iran

Work Experience

2011 – 2013 **Process Engineer**
OptoGaN GmbH, Landshut, Germany

2011 – 2011: **Research assistant**
Institute of Optoelectronics, University of Ulm, Germany